Doctoral theses at NTNU, 2021:243

Torbjørn Andersen Ve

Effect of Absorbed Water and Temperature on Charge Transport and Accumulation in XLPE Cable Insulation

Doctoral thesis

NTNU
Norwegian University of Science and Technology
Thesis for the Degree of Philosophiae Doctor
Faculty of Information Technology and Electrical Engineering
Department of Electric Power Engineering

NTNU
Norwegian University of Science and Technology

Torbjørn Andersen Ve

Effect of Absorbed Water and Temperature on Charge Transport and Accumulation in XLPE Cable Insulation

Thesis for the Degree of Philosophiae Doctor

Trondheim, June 2021

Norwegian University of Science and Technology
Faculty of Information Technology and Electrical Engineering
Department of Electric Power Engineering

NTNU

Norwegian University of
Science and Technology

NTNU
Norwegian University of Science and Technology

Thesis for the Degree of Philosophiae Doctor

Faculty of Information Technology and Electrical Engineering
Department of Electric Power Engineering

ISBN 978-82-326-5278-5 (printed ver.)
ISBN 978-82-326-6995-0 (electronic ver.)
ISSN 1503-8181 (printed ver.)
ISSN 2703-8084 (online ver.)

Doctoral theses at NTNU, 2021:243

Printed by NTNU Grafisk senter

Preface

This thesis is submitted in partial fulfilment of the requirements for the degree of Philosophiae Doctor (PhD) at the Norwegian University of Science and Technology (NTNU) in Trondheim, Norway. The PhD work has been carried out at the Department of Electric Power Engineering, between October 2010 and March 2021. Associate Professor Frank Mauseth has been the main supervisor for this work, with Dr. Øystein Hestad and Professor Erling Ildstad as co-supervisors.

The PhD work was part of the Norwegian Renergi R&D project "High Voltage AC and DC Subsea Cables for Offshore Wind Farms and Transmission Grids", funded by the Research Council of Norway and the industrial partners Nexans Norway AS, EDF R&D (France), Equinor ASA, Statnett SF, Statkraft SF, and Borealis.

Abstract

As the use of HVDC subsea power cables increases, studying DC phenomena in wet conditions becomes increasingly important. Space charge accumulation and transport in the insulation is relevant for ageing and the ability to resist failure due to voltage transients.

This thesis investigates the effect of absorbed water on conducted current and space charge accumulation in cross-linked polyethylene (XLPE) insulation with semiconducting polymer electrodes. Two different measurement techniques were utilised: polarisation-depolarisation current measurement and the pulsed electroacoustic space charge measurement technique. Temperatures between 20–80 °C, which are within the temperature range found in a cable in service, were chosen. Measurements were conducted on samples with water contents of between 4 and 90% saturation levels.

Measurements of conducted current showed that the presence of absorbed water increases the apparent electrical conductivity in XLPE up to 3.5 times the dry-state conductivity, with an exponential temperature and electrical field dependency that does not significantly change from dry to wet insulation. Several commonly used conduction mechanisms were found to be able to describe the current in samples with the same water content, but no single conduction mechanism could predict the changes in conductivity with water content. A dual-mechanism model was tested and found to describe the changes in conductivity across all measured levels of applied electric, temperature and water content, albeit with parameters outside what is possible for the base physical mechanisms.

Measurements of space charge accumulation showed that injected charge was likely dominant in both dry and wet samples, with absorbed water increasing charge mobility at temperatures up to 60 °C. The increase in mobility was supported by measurements of time-dependent current. At temperatures above 20 °C, positive charge was the main contributor to space charge, both for wet and dry samples. At 80 °C, absorbed water seemed to differ in effect compared to the lower temperatures, leading to increased amounts of accumulated charge that did not stabilise within the measurement period.

In summary, the effect of absorbed water on conducted current and accumulated space charge does not appear to be critical for XLPE insulation systems at temperatures of 20–60 °C. At higher temperatures, further investigation is warranted, given the apparent detrimental change in mechanism for accumulated charge in wet conditions at 80 °C.

Acknowledgements

Thanks to all the people who have contributed with help in the lab or discussions around this rather dry subject. I would like to thank my main supervisor, Frank Mauseth, for guidance through this lengthy process. It's taken some time, but you've dragged me through it. I would also like to thank my co-supervisor, Øystein Hestad at SINTEF, for good discussions on the minutia of charge transport, and much help with getting a less coherent piece of work to a finished document in the final phase. Thanks to my co-supervisor, Erling Ildstad, for discussions in the early part of the work.

At SINTEF, several people have contributed. Thanks to Sverre Hvidsten for fruitful discussions and also access to his secret stores of equipment that was implemented in some of the experimental setups. Thanks to Hallvard Faremo, the project manager for the Offshore Wind Farm Cables SINTEF project, for support and for getting me my very own climate chamber (though I seem to have occupied two of them, and I don't think I ever asked for permission…). Also, my other colleagues at SINTEF, and former colleagues at NTNU, have helped a lot with the work. Thanks for lending your more-or-less willing ears when I was enthusiastically talking about how water diffusion or charge transport works, or complaining about some equipment that seemed to break all of the time. A lot of you have become friends, and some I've even managed to trick into going running or skiing or hiking or climbing with me – I appreciate the trips and am grateful you found time for them.

Emiliya, you have only been part of my life for a short time, but you are an inspiration to me. Everything seems a little easier to manage with you around. Thank you for being your wonderful self.

Finally, I would like to thank my family and friends, especially my parents and my sisters. While continuous questions of "how is the PhD work progressing?" was at times annoying, I know that they came from a good place and I am very grateful for you asking them. Now I can finally answer "It's going great! I'm done!"

Contents

1 Introduction

High-voltage direct current (HVDC) subsea links have been in use for almost 70 years, with the first cable, connecting the Swedish island of Gotland, going into service in 1954. Recent years have seen an increased interest in use of HVDC links due to the increasing need for long-distance power transfer. In applications that involve high power loads, such as connecting islands to a mainland grid, like the Gotland link, or subsea interconnections between countries, use of large HVDC cables is advantageous.

The viability of choosing HVDC power transfer over the more established high-voltage alternating current (HVAC) system depends on transfer distance. While the converter stations needed in an HVDC link makes the distance-independent investment more expensive than HVAC, costs for HVAC go up faster with increasing distance than HVDC, due to higher line costs and reactive losses that increase with cable length. The breakeven distance, i.e. when HVDC starts getting more economical than HVAC, will be dependent on the specific project, but for lengths greater than 50–100 km HVDC often starts becoming a viable option [1,2]. Connecting to offshore installations, such as oil rigs or offshore renewable power production, with HVDC requires a higher initial investment cost, as converter stations located on platforms or on the seabed are more expensive than land-based stations, and can therefore move the breakeven distance even further. However, the recent increased interest in offshore wind farms likely means that the demand for HVDC power links will increase, due to the long transfer distances required to connect to the remote locations of these farms, and also that investment costs will decrease as the technology of platform and seabed converter stations matures.

HVDC cable insulation has traditionally been lapped insulation, typically consisting of layered paper or plastic laminates impregnated with insulating oil. The use of HVDC extruded polymer-insulated cables have increased in recent years [2]. Extruded insulation exposed to HVDC loads have historically had issues with failures during polarity reversals, which has been related to the accumulation of space charge [1,3]. Technological development, especially the introduction of voltage source converters (VSC) which have eliminated the need for polarity reversals to reverse power flow, have made extruded HVDC cables feasible to use. Using extruded insulation has advantages, as it can withstand higher conductor temperatures than mass impregnated cables, is more mechanically robust, has a lower weight per meter cable and cable joints that are simpler to construct [2,4]. However, even though VSC technology has eliminated the main source of detrimental effects from space charge, it is still important to know how space charge accumulates in the insulation system, as it will have an effect on ageing [5,6] and the capacity to withstand failure during rapid grounding or when exposed to transients. In addition, new dynamic load patterns due to, e.g. use of cables in wind farms, means that changes in space charge accumulation and conducted currents due to changes in

temperatures are also important parameters to consider when using extruded insulation systems.

Subsea high-voltage (HV) cables have traditionally included a water blocking sheath. For dry-design cables the barrier is metallic (extruded lead, welded copper or aluminium), while wet-design cables can have completely polymeric barriers or hybrid barriers consisting of an overlapping non-welded metal barrier in combination with polymer materials. Lead sheathing has been the most commonly used water barrier. However, cost concerns and the need for dynamic cables in moving installations such as floating windmills or other offshore platforms have shifted the market more towards wet designs. Even for purely static cables such as subsea transmission cables, the lighter and cheaper wet designs will be relevant to save costs. Finally, the European Chemicals Agency is expected to include lead in the REACH authorisation list, banning lead from being used to manufacture, repair or maintain cables, possibly as early as 2025 [7].

Polymeric water barriers, which are lighter, cheaper and easier to manufacture, and also have better resistance to dynamic mechanical stress, are being introduced as alternatives to metal barriers. The challenge of using polymeric water barriers is that polymers are never completely watertight. Long-chained polymer molecules will have gaps between the molecular chains through which small molecules can pass. Water will therefore diffuse into the insulation system over time. For alternating current (AC) cables, the presence of water in the insulation must be minimised, as water trees will be created at relative humidities above 70% [8]. In HVDC cables, however, the effect of water is less known. The aforementioned space charge accumulation and conducted current is suspected to be affected by absorbed water, although only a few systematic studies have thus far been conducted [9-13].

Purpose of work

The knowledge of the effect of absorbed water on the electrical properties of HVDC cable insulation is limited. The purpose of this work is therefore to study the changes in space charge accumulation and conductivity of a commercially available XLPE insulation system with varying amounts of absorbed water present. Several items of interest present themselves:

- What is the origin of accumulated charge in XLPE?
- What is the effect of increased temperature on charge accumulation and transport in XLPE?
- Can charge transport in XLPE with absorbed water be satisfactorily described by existing conduction mechanisms?
- How does absorbed water alter the accumulation of space charge in XLPE?
- Does the effect of water change with temperature?

Measurements of conducted current and space charge accumulation were performed to address these questions. As temperature alters both the electrical properties and the rate and amount of water absorption, measurements at three different temperatures were done. As insulation temperature can be as high as 90 °C, the temperatures 40, 60 and 80 °C were chosen. In addition, some measurements were also performed at room temperature. All electrical tests were done on samples with semiconducting polymer electrodes, as this is what is present in an extruded cable. To control the water content in the samples, water absorption and permeation measurements were also performed.

2 Theory

2.1 Introduction to charge transport in polymers

Although a perfect insulation material does not conduct electricity, real materials are far from this ideal and charged particles will move through them when under a potential gradient. These mobile charged particles are referred to as charge carriers. For insulating polymers, the movement of charge is affected by a variety of factors, such as the composition of the polymer chain itself, degree of crystallinity, whether the polymer is cross-linked and the presence of additives and impurities. The type of charge carriers present in the polymer will also impact the movement, as for instance the physical size of carrier or polarity and charge number will have an effect. The origin of the carriers can be from bulk generation, for example ionisation of impurities, or injection from the electrodes.

In general, charge carriers are separated into two main categories: electronic carriers and ionic carriers. Electronic carriers consist of negatively charged electrons and positively charged virtual particles called holes, which are created by the absence of an electron. Charge carriers injected from the electrodes generally refer to electronic carriers, i.e. electrons and holes [14]. The rate and type of injection is very dependent upon the electrode-dielectric interface; for instance, metallic electrodes have been found to provide different injection conditions than semiconducting polymer electrodes [14]. Different types of electrodes may also affect extraction of charge carriers. Ionic carriers are positive and negatively charged ions which originate from, for instance, ionisation of impurities in the bulk. In certain circumstances, such as sharp defects at the electrodes, field strengths could be high enough to cause ionisation, leading to positive ions generated at the electrodes, although this requires higher electric field strengths and is often more connected to pre-breakdown phenomena than sustained charge generation [15]. Mechanisms that result in bulk-generated electronic charge carriers also exist. In Section 2.2, several mechanisms relevant to the transport of charge in XLPE are presented. In addition, measurement principles used to determine which of these mechanisms controls the flow of current are introduced. Section 2.3 concerns the theory around the build-up of charge inside the insulation material, and also presents some methods for evaluating the behaviour of the stored charge.

2.2 Conductivity and conduction mechanisms

2.2.1 Introduction

Dielectric materials have a very low intrinsic conductivity. Real dielectrics, however, contain defects, in the form of voids of various sizes, and impurities, such as cross-linking by-products and additives, which explains why the measurable conductivity is significantly higher than the intrinsic [16].

Conductivity in a material can be expressed as

$$\sigma = \sum_{\text{All } i} n_i q_i \mu_i \tag{2.1}$$

in which n is the concentration, q the charge and μ the mobility of the charge carriers. The total conductivity will be the sum of the contributions from each different charge carrier species, denoted by i. Defects and impurities will affect the conductivity either as carrier sources, by increasing n, or facilitating the movement of charge carriers through the polymer matrix, increasing μ. In polymers, charge carriers can be electrons, holes and various kinds of ions. The movement of electronic charge carriers is described by quantum mechanics, often using the movement of electrons in crystals as a starting point [16]. The movement of ions is governed by the principles of mass transport [17,18].

At low applied electric fields, the conductivity will be constant, and Ohm's law will be valid. This is therefore called Ohmic conduction. At higher electric fields, the field dependence of the conductivity means that more complex models must be used. Section 2.2.2 summarises the principles for the movement of electrons in an electric field in polymers and presents several conduction mechanisms that attempt to explain the observed non-linear behaviour of conductivity at high fields. In Section 2.2.3, the movement of ions and ionic conduction mechanisms are discussed.

2.2.2 Electronic conduction and band structure

This section will go through the basic principles of electron and hole conduction band structure (for more information see e.g. [16,19-21]).

By applying quantum mechanics, electrons in insulating solids are found to be limited to only certain energy levels, separated by forbidden gaps [16,22]. In a periodic potential lattice, the energy levels group together to form ordered energy bands, which may be occupied by electrons. Transport of electrons can only occur in bands which are not completely occupied. The highest completely occupied energy band is called the valence band, while the empty band immediately above is referred to as the conduction band. The

forbidden gap between the valence and conduction bands determines the intrinsic conductive properties of the material. The width of the band gap for some insulating polymers can be very large, for example for polyethylene at about 8.8 eV [23], which means that almost no electrons will be found in the conduction band. This would in principle make the material an almost perfect insulator. However, the structural imperfections and presence of impurities in real polymers introduce states within the forbidden gap which electrons can occupy [24,25]. The extent of these states is limited in space to around the impurity or imperfection, which means that they exist as discrete localisation points within the polymer structure. Impurity states just below the conduction band can act as electron donors, enabling mobile electrons in the conduction band at a lower energy than would be required for a valence band electron. At the other end of the band gap, impurity states just above the valence band can act as electron acceptors, increasing the creation of positive 'holes' in the valence band, which can act as virtual charge carriers. The effect of an impurity state on the transport of charge depends both on the energy level and the nature of the impurity state. While an electron acceptor state close to the valence band aids the generation of holes, an acceptor state close to the conduction band may slow the transport of electrons due to increasing the residence time of electrons at the impurity. The term describing states that localise charge at particular sites is charge traps. The trap depth describes the energy level compared to the conduction band for electrons and the valence band for holes.

The concept of the conduction band will be valid as long as the lattice stays periodic with a certain degree of order. A one-dimensional regular lattice will be valid along a polymer chain, while crystalline groups in polymers form relatively regular inter-chain lattices. Crystalline groups are limited in size, however, as irregular folding of chains and chain entanglement leads to formation of amorphous zones. These zones can affect the transport of electronic charge carriers due to, for instance, the interfacial regions between crystalline and amorphous zones behaving as trap states [26]. In addition, different morphological groups may be preferential to electron or hole transport. As holes are vacancies in the valence band, they are limited in location to the polymer chains, and are most easily transported where the chains are more dense, i.e. crystalline zones. On the other hand, calculations of electron conduction states in polyethylene have found that they are mainly interchain [27], which indicates that electrons contributing to conduction will likely prefer to move in lower-density, amorphous regions. This hypothesis is supported by the observation that polyethylene has a negative electron affinity.

Contact between the polymer and other materials may lead to injection of charge carriers into the polymer. This occurs either due to an externally applied electric field or due to a difference in Fermi levels between the polymer and the electrode. In the first case, the injection will continue until the external electric field is removed. In addition, space charge may form to counter the effect of the field. In the last case, charge will form until the difference in Fermi levels is equalised.

The conduction mechanisms governing the generation and transport of charge carriers will depend on the applied electric field, temperature and electrode effects, in addition to being dependent on the presence of trap states from, for instance, imperfections in the polymer structure, impurities or morphology. Below, the principles of four possible conduction mechanisms for electronic charge carriers in XLPE are summarised, and their dependencies on electric field and temperature presented.

2.2.2.1 **Hopping conduction**

Hopping conduction supposes that the mobility of charge carriers is limited by localisation at trap sites. Originally developed for conduction in ionic crystals [28], it has also been shown to be applicable for electronic charge carriers [29]. The amount of time an electronic charge carrier will spend in a trap depends on the depth of the trap, the temperature and the electric field acting on the carrier. The movement of carriers from trap site to trap site is a thermally activated process, enhanced by the electric field. Given a high enough density of traps, with an average distance a between trap sites, this will be a series of potential wells, separated by barriers with a barrier height Φ corresponding to the trap depth. An applied electric field will lower the energy required to surmount the potential barrier, increasing the net jump frequency. The conductivity can be expressed as [28,29]

$$\sigma = ne\frac{2a\nu}{E}\exp\left(-\frac{\Phi}{kT}\right)\sinh\left(\frac{aeE}{2kT}\right) \tag{2.2}$$

in which e is the elementary charge, ν the frequency of attempts to escape the trap and k the Boltzmann constant. The same formalism can also be reached for ionic carriers, as will be shown in Section 2.2.3.1. Hopping conduction has previously been used to describe current flow in XLPE insulated cables in [30], although the nature of the carriers was not focused on in that work.

2.2.2.2 **Schottky injection**

Schottky injection is regularly included as the high-field injection mechanism when modelling charge transport [31-33] and has also been found to be a probable conduction mechanism for XLPE in some cases [34,35]. It assumes that the current is limited by field-assisted injection of electrons or holes from the electrodes. At the electrode-dielectric interface, electrons will experience a barrier due to the electrostatic attraction between the electrode and an electron. This can be illustrated by a “mirror image charge” of equal and opposite charge to the electron, placed equidistant to the neutral plane at the interface. An applied field would then reduce the effective barrier height at the interface. Using Coulomb’s law and Fermi-Dirac statistics, this yields [16]

$$J = \frac{4\pi e m k_B^{\,2} (1-R) T^2}{h^3} \exp\left(-\frac{\Phi}{kT}\right) \exp\left(\frac{e}{2k_B T}\sqrt{\frac{eE}{\pi\varepsilon}}\right) \tag{2.3}$$

in which m is the electron mass, $R \leq 1$ the proportion of electrons that are reflected at the interface, T the temperature, h the Planck constant and Φ the barrier height.

In [35,36], a modification of the Schottky mechanism was used to include the field distortion effect of space charge near the electrodes. This replaced the geometric electric field E with the local electric field at the cathode E_C, using $E_c = \gamma E$. For $\gamma > 1$, the local electric field controlling injection is higher than the geometric field. Enhanced local electric field means that the space charge near the injecting electrode is heterocharge. For $\gamma < 1$, the local electric field is lower than the geometric field and the change is caused by homocharge [35,36].

2.2.2.3 **Poole-Frenkel conduction**

A bulk-limited conduction mechanism, Poole-Frenkel involves the thermionic emission of electronic carriers. In order for Poole-Frenkel conduction to occur, the band structure of a material must have a wide band gap with donor states some kT below the conduction band or acceptor states some kT above the valence band, so that no free carriers are generated at room temperature. An electron in a donor state will experience barriers limiting movement. As with Schottky injection, the applied electric field lowers the barriers in the field direction and increases the barrier in the direction opposite to the field. The conductivity using the Poole-Frenkel model can be expressed as [16]

$$\sigma = \left(N_{\text{eff}} N_{\text{D}}\right)^{0.5} e\mu \exp\left(-\frac{\Phi}{2kT}\right) \exp\left(\frac{\beta}{T}\sqrt{E}\right) \tag{2.4}$$

in which N_{eff} is the effective density of states in the conduction band, N_{D} is the density of donors, Φ the barrier height and β a constant connected to presence of trap states in the material. If there are no traps, $\beta = \frac{e}{2k}\sqrt{\frac{e}{\pi\varepsilon}}$. If there is a single trap level, $\beta = \frac{e}{k}\sqrt{\frac{e}{\pi\varepsilon}}$ [37]. Poole-Frenkel conduction has been suggested as a conduction mechanism for XLPE in a number of publications [34,38,39].

2.2.2.4 **Space-charge limited current**

At low charge mobility, injected carriers may accumulate in the bulk as space charge. The electric field from this accumulated charge will affect the conducted current. In some cases, space-charge limited current has been found as the dominant conduction

mechanism in XLPE [40,41]. In the case of only electrons as charge carriers, a perfect contact injecting electrode and uniformly distributed space charge, the space-charge limited current density is given by [16]

$$J = \theta \frac{9\varepsilon\mu V^2}{8d^3} \tag{2.5}$$

in which θ is the ratio between the number of electrons in the conduction band and in traps, V is the applied voltage and d the sample thickness. For a dielectric without traps, $\theta = 1$. For a dielectric with traps, the value of θ is voltage-dependent. At low voltage above the Ohmic region, most electrons are trapped and θ is very small. As the voltage rises, traps become filled, and θ increases towards unity. This results in the current density increasing more rapidly than with V^2. When all traps are filled, the current density once again increases with the square of the voltage. For a single trap level, the current density will increase as $J \propto V^{\infty}$, at a given voltage level (the trap-filling limit). However, in real dielectrics the trap levels are usually distributed, which leads to the current density increase having a dependency between V^2 and V^{∞}.

2.2.3 Ionic conduction

While electronic charge carriers involve electrons moving along molecular chains or between localised traps, ionic carriers are governed by the principles of mass transport. This means that they will move between polymer chains, similar to the diffusion process governing the movement of neutral particles. Areas in the polymer structure with lower density will be preferred, and transport will take place mainly in the amorphous zones, while crystalline zones will be more or less impermeable.

Mobile ionic species in insulating polymers are usually assumed to have their origin in impurities or additives. These can be consciously introduced as, for example, anti-oxidants [42]. Other sources can be by-products from cross-linking processes [43-45], gases or vapours absorbed from the atmosphere, oxidation residue or migration of species from materials in contact with the insulation, such as semiconducting electrodes [42,46]. Lastly, absorbed water vapour may lead to ionic dissociation [13,47].

2.2.3.1 Hopping conduction

As described for electronic charge carriers in Section 2.2.2.1, the hopping conduction mechanism describes conduction due to localised carriers moving in a lattice of occupation sites. Due to thermal excitation, the ion will attempt to jump over the barrier to the next site with a given frequency. Assuming an isotropic material, the probability of a jump will be equal for all directions in the absence of an electric field. When a field is applied, the barrier in the field direction will be reduced and the barrier in the opposite

direction increased. This gives a net flow of carriers in the field direction, similar to Equation (2.2) [16]:

$$J = 2qnav\exp\left(-\frac{E_A}{kT}\right)\sinh\left(\frac{qaE}{2kT}\right) \tag{2.6}$$

in which E_A is the energy required to jump over the barrier and q is the charge of the ion. The hopping mechanism was originally derived for conduction in ionic crystal structures, but has been extended to apply to ionic conduction in polymers.

2.2.3.2 Ionic dissociation

Most polymers will contain additives, by-products of manufacturing or other impurities. Of these, some are dissociable, meaning that a portion of the compound will dissociate into its associated ions. Assuming a single dissociable compound contributing to the current, and that there is equilibrium between the original molecules and product ions, the conductivity from ionic dissociation can be expressed as [48]

$$\sigma = \sqrt{K_0 n_0}\, e\left(\mu_+ + \mu_-\right)\exp\left(-\frac{\Delta W}{2\varepsilon kT}\right) \tag{2.7}$$

in which K_0 is the equilibrium constant for the dissociation reaction, n_0 is the concentration of ionisable compound, μ_+ and μ_- are the positive and negative ion mobilities, respectively, and ΔW is the activation energy required for the separation of the product ions.

2.2.3.3 Ionic dissociation in an electric field

When an electric field is applied, ions of opposite charge will experience forces in opposite directions. This leads to the equilibrium between molecules and ions shifting, increasing the number of dissociated ions. The effect of this equilibrium shift on the dissociation constants can be calculated [49,50], giving

$$k_D = k_{D_0}\mathrm{J}_1\left(-\frac{1}{kT}\sqrt{\frac{8Ee^3}{\pi\varepsilon}}\right)\Big/\left(-\frac{1}{kT}\sqrt{\frac{Ee^3}{2\pi\varepsilon}}\right) \tag{2.8}$$

Where k_{D_0} is the dissociation coefficient of ion pairs to free ions and J_1 is the Bessel function of the first kind and order one. By assuming a high enough electric field, this can be approximated to yield the field-dependent conductivity as [49,50]

$$\sigma = \left(\mu_+ + \mu_-\right) e \left(\frac{\nu_0}{k_\mathrm{R}}\right)^{0.5} {k_{\mathrm{D}_0}}^{0.5} \exp\left(-\frac{\Delta W}{2kT}\right) \left(\sqrt{\frac{2}{\pi}} \left(\frac{e^3 E}{\pi \varepsilon k^2 T^2}\right)^{-0.75} \exp\left(\sqrt{\frac{e^3 E}{\pi \varepsilon k^2 T^2}}\right)\right)^{0.5} \quad (2.9)$$

in which ν_0 is the concentration of ion pairs, and k_R is the recombination constant of free ions to ion pairs. The concentration of ion pairs is usually proportional to the concentration of dissociable ions, which means that the conductivity given by Equation (2.9) will yield a similar square root dependency on the concentration of ionisable compound as in Equation (2.7). Assuming that dissociation in a dielectric liquid is a valid approach for XLPE, the approximation leading to Equation (2.9) is valid for electric fields of higher than 7–9 kV mm^{-1}, depending on temperature, meaning that some error will be expected for low applied electric fields.

2.2.4 Measurement principles

2.2.4.1 Steady-state current

In most of the equations used to describe the conduction mechanisms in Section 2.2.2 and 2.2.3, either the conductivity or the current density is expressed as a time-independent function of electric field and temperature. Measuring the steady-state current density at different combinations of applied electric field and temperatures may therefore yield insight into the underlying conduction mechanism. When water is absorbed, the changes, if any, to the current would provide information on what the nature of the effects are. A limitation of this method is that, as can also be seen in the previous sections, most of the expressions for the current density and conductivity are exponentially dependent on the applied electric field and temperature. Distinguishing the different mechanisms from each other may therefore be challenging.

2.2.4.2 Transient current

Investigating the time dependence of the charging and discharging currents can give insight into the mechanisms beyond what can be found from steady-state currents. For a solid dielectric, the charging current density can be expressed as

$$J_{\mathrm{C}}(t) = \varepsilon_0 E\left(\delta(t) + f(t)\right) + \sigma E \tag{2.10}$$

where $\delta(t)$ factor is a delta function describing the instantaneous polarisation response of the system, meaning the response of unoccupied space in any free volume and voids in the dielectric. $f(t)$ is the combined response of the material components constituting the dielectric, which is the sum of their polarisation currents. σE is the contribution of the conduction current. The discharging current in an ideal dielectric will be similar, minus the conduction current contribution. The most generic polarisation current response is described by the Curie-von Schweidler model [51], which gives the current as a power law response with exponent m

$$f(t) \propto t^{-m} \tag{2.11}$$

which will yield a straight line on log-log plots. A generic transient charging current response will therefore be the sum of a power law relation and a constant conduction current. Deviations from this are possible, however, given that charging currents not conforming to Equation (2.10) have previously been observed for polyethylene, for example in [52] and [53]. There are various models that explain deviations from the transient charging current response based on space charge effects [54,55] and hopping mechanisms [52,56]. Charge transport models that take several interacting mechanisms into account have also been developed [53,57,58]. Common to all these models is that

they predict a peak in the transient charging current, which can be used to estimate the mobility of the charge carriers [54].

Comparing short-time charging and discharging currents, and also comparing discharging currents between measurement series, would also provide insight as to the dominant mechanism. Dissimilar charging and discharging currents would be an indication of space charge phenomena, while hopping processes would yield symmetrical currents with opposite signs [59].

2.3 Space charge in polymers

2.3.1 Introduction and definitions

Space charge in a dielectric occurs when there is an imbalance between the charge entering and exiting a volume. This can occur near the electrodes, for instance if there is a surplus of injected charge or a limitation on charge extraction. Charge can also accumulate in the bulk, as for example when dissociation of impurities creates low mobility ions or when trap sites in the bulk prevent the motion of charge carriers.

Through Maxwell's equations, it is seen that space charge is closely connected to the conductivity and permittivity of a dielectric. Combining Gauss's law

$$\nabla \cdot \vec{E} = \frac{\rho}{\varepsilon} \tag{2.12}$$

with Ohm's law

$$\vec{J} = \sigma \vec{E} \tag{2.13}$$

and considering charge a conserved quantity yields [60]

$$\rho + \frac{\varepsilon}{\sigma}\frac{\partial \rho}{\partial t} = \vec{J}\nabla\frac{\varepsilon}{\sigma} \tag{2.14}$$

In the equations above, $\vec{E}$ is the electric field, ρ is space charge density, ε the permittivity, $\vec{J}$ the current density, σ the conductivity and t time. From Equation (2.14), it is seen that a non-constant ratio between permittivity and conductivity in a volume through which a current is flowing will result in charge accumulation. An example of this is a temperature gradient over the insulation in a cable, as while the permittivity in many polymer insulation materials remains almost constant as temperature changes, the conductivity is typically highly temperature-dependent [61]. This means that the conductivity will change along the temperature gradient, while the permittivity will not, thus the ratio changes and leads to build-up of space charge. Other examples of non-constant ratios between conductivity and permittivity are interfaces between different dielectrics, between impurities and the dielectric and between crystalline and amorphous zones in semi-crystalline polymers [62].

One way in which this can occur in a cable system is when the conductivity increases in proximity of the semiconductors while the permittivity remains constant. The higher conductivity originates in impurities from semiconductor electrodes, such as carbonyl

groups, diffusing into the insulation during production, as shown in [63]. The highest concentration of diffused impurity traps would likely be found closest to the electrodes, with the concentration decreasing towards the bulk.

In [64], this was implemented on an XLPE insulation system with semiconductor electrodes, using an exponential conductivity enhancement corresponding to an impurity concentration gradient resulting from diffusion, yielding

$$\sigma(x)=\sigma(E,T)\left(1+(m_\sigma-1)\left(\exp\left(-\frac{x}{x_\sigma}\right)+\exp\left(-\frac{L-x}{x_\sigma}\right)\right)\right) \tag{2.15}$$

in which m_σ is the conductivity enhancement factor at the interface and x_σ is a distance factor, changing how far into the bulk the conductivity enhancement occurs. L is the sample thickness, and $\sigma(E,T)$ is the bulk conductivity.

2.3.2 **Apparent mobility**

The apparent mobility of charge from space charge profiles during discharge can be calculated by using the mean of the absolute value of charge [65,66]. The sample is assumed to be a parallel plane electrode system, yielding

$$J(t)=J_C(t)+\varepsilon\frac{\partial E(x,t)}{\partial t}=\rho_{\mathrm{f}}(x,t)\mu(t)E(x,t)+\varepsilon\frac{\partial E(x,t)}{\partial t} \tag{2.16}$$

Here, J is the total discharge current density, J_C is the conduction contribution, E the electric field, ε the permittivity, ρ_f the free charge carrier density and μ the mobility. Using the Poisson equation for a parallel plane electrode system, i.e. $\varepsilon\frac{\partial E(x,t)}{\partial x}=\rho_{\mathrm{f}}(x,t)+\rho(x,t)$, and integrating along the sample thickness, l, results in

$$\mu(t)=\frac{J(t)l-\varepsilon\frac{\partial}{\partial t}\int_0^l E(x,t)\,\mathrm{d}x}{\varepsilon\frac{\left[E(l,t)\right]^2-\left[E(0,t)\right]^2}{2}-\int_0^l\rho(x,t)E(x,t)\,\mathrm{d}x} \tag{2.17}$$

To calculate the apparent mobility, Equation (2.17) is simplified through several assumptions [65]. First, the free conducted charge is assumed to be very small ($\rho_f \ll \rho$). Second, recombination and simultaneous occupation of space by charge with opposite polarities can be neglected ($J(t)=L\,\mathrm{d}\overline{\rho}/\mathrm{d}t$; $\overline{\rho}$ is the mean density of total charge,

assuming charge uniformly distributed in the insulation). Third, the electric field is assumed to be uniform ($E(x,t) = \bar{\rho}L/2\varepsilon$, $\partial E/\partial x = 0$, meaning the electric field is mostly due to charge at the electrodes). This leads to the apparent mobility being expressed as

$$\mu(t) = -\frac{2\varepsilon}{\bar{\rho}(t)^2}\frac{\mathrm{d}\bar{\rho}(t)}{\mathrm{d}t} \tag{2.18}$$

The change in mobility over time during discharge is attributed to the trap distribution of the material [65].

There is no analytical expression for the time dependence of the net total charge in a sample, and as such, the derivative of the mean charge density does not have an analytical expression. In the mobility estimations, the discrete difference is therefore used as an approximation of the derivative: $\frac{\partial\bar{\rho}(t=n)}{\partial t} \approx \frac{\bar{\rho}(n+1)-\bar{\rho}(n)}{t(n+1)-t(n)}$.

2.3.3 Charge traps and electrode effects

On the microscopic level, the presence of charge traps will lead to a localisation of charge. However, the effect on space charge accumulation will vary, depending on the trap depth and distribution. For shallow traps, residence times will be low, and the traps may even assist the transport of charge, as described in Section 2.2.2. The increased local charge mobility this will produce is one possible microscopic origin of the conductivity increase described in Section 2.3.1 and [64].

In the case of deeper traps, residence times will be higher, leading to a localisation of charge and reduction in charge mobility. The distribution of traps will be important for the effect on the accumulation of space charge, but even a uniform trap distribution can lead to a build-up of local concentrations of charge. If, for instance, there is charge injection, the deep traps close to the injecting electrode will be filled first, leading to homocharge build-up. In the same manner, if the deep traps are located close to the extracting electrode, injected charge from the opposite electrode, having crossed the sample, will start filling traps further away from the extracting electrode first, resulting in heterocharge build-up.

Carbonyl groups, a common impurity in XLPE, are deep traps for electrons and shallow traps for holes, as shown by density functional theory calculations in [67]. The effect of carbonyl on space charge has been found to be dependent on concentration: low concentrations were found to increase accumulation, while high concentrations lowered

space charge accumulation, possibly related to providing hopping sites for hole conduction, leading to increased carrier mobility [68].

2.4 Effect of absorbed water in XLPE insulation on charge transport and accumulation

2.4.1 Existing hypotheses

In the literature, there are several hypotheses on how water can affect the conduction and accumulation of charge in an insulating polymer material. This section summarises some of these hypotheses: water directly affecting the trap distribution is discussed in Section 2.4.1.1; water solvation and migration of semiconductor impurities in Section 2.4.1.2; water assisted ionic dissociation of embedded impurities in Section 2.4.1.3; and ionic dissociation of water molecules in Section 2.4.1.4.

2.4.1.1 Water molecules increasing shallow-trap density

Absorbed water in a non-polar polymeric insulating material will be located in the free volume between molecular chains in the amorphous regions. The water molecules can there act as trapping sites for charge carriers, either forming space charge if the traps are deep or increasing charge mobility if the traps are sufficiently shallow. Calculations on water molecule trap depth for electronic charge carriers have shown that water molecules are shallow electron traps [67,69], which might lead to increased electron mobility with increased water content. Indications that water affects trap levels and charge mobility has also been found in [10,11].

2.4.1.2 Solvation-assisted migration of impurities from semiconductors

As mentioned in Section 2.3.1, diffusion of impurities from the semiconductor into the insulation has been found to occur [42,63,70,71]. For water soluble impurities, such as carbonyl and ionic groups, higher water content would be expected to increase diffusion, as shown for several different water-soluble impurities in [70,72]. The type and concentration of impurities would determine the effect on charge accumulation and transport.

Non-ionic impurities would act as charge traps of different depths, while ionic dissociable impurities transported into the insulation would be sources of ions. For both types, the amount and location of either traps or charge sources would be dependent on the rate of diffusion. In general, higher temperatures and higher water content would be expected to increase both the amount migrated and the depth of penetration of the impurities. The impact would be expected to be higher near the electrodes, with the impurity concentration in the insulation increasing close to the electrode interface.

As diffusion is a thermodynamic process, the temperature and access to water (which will be higher at higher temperatures and relative humidities) will affect the extent of

diffusion. The time required for an impurity to migrate in significant quantities would be dependent on the type of impurity and its interaction with the polymer matrix. For short tests, in the range of minutes to an hour, very little change in impurity concentration would be expected. For longer tests lasting several days, some diffusion could be expected to take place.

While in the literature cited above it appears that the effect of impurity migration from the semiconductor into the insulation could be significant, it is likely that less impurities are present in the semiconductor polymers used in the present work. Compared to the semiconductor grades used in [42,63,70,71], the impurity content in semiconductors has in general been reduced significantly compared to when those studies were conducted [73]. In addition, there are studies in the literature that contradict the notion that water enhances the migration of impurities, finding that most of the impurities found near the semiconductor electrodes are remnants from production [74]. In that case, no difference between samples with and without absorbed water would be expected for this mechanism.

2.4.1.3 **Water-enhanced dissociation of embedded impurities**

The presence of dissociable impurities in XLPE is a possible source of charge carriers. Water molecules in proximity to these impurities may enhance the dissociation into ions due to its high dielectric constant [9,47]. This requires a sufficiently high concentration of water so that the local electrical environment around the impurities is affected. This might occur if water clusters around impurities without solvation; the polar water molecules being drawn towards the high local electric field interface regions between impurities and the polymer matrix. Another possibility is that water soluble impurities might be partially dissolved by water, enhancing the dissociation rate [75-77]. In general, the increase in ionic dissociation would be expected to lead to an increase in heterocharge and conducted current.

Potential sources of ions in the samples are in principle any ionisable species present in sufficient quantity. The most abundant species are of course the molecular chains themselves, but as polyethylene molecules are not easily ionisable, these can be excluded. Other species are cross-linking by-products, the most common of which are acetophenone, methyl alcohol and α-methylstyrene, as well as additives such as antioxidants.

Starting with the cross-linking by-products, methyl alcohol and α-methylstyrene have been found to mainly assist in trapping of other charge carriers [44]. While acetophenone alone has been found to not affect space charge [46], it has been found to contribute to heterocharge generation when in the presence of antioxidants [46,77] or water [44,77]. It seems unlikely that this originates from the ionisation of acetophenone molecules themselves, as the energy of acetophenone ionisation is one to two orders of magnitude

higher than kT, even at 80 °C. As for acetophenone ionisation when solvated, this is also unlikely to affect the current much, as the acid dissociation constant is very high [78]. As such, the contribution of acetophenone to charge generation is likely only due to increasing the rate of dissociation of other species, such as antioxidants or water, as a result of the high polarity of the acetophenone molecule. Degassing has been found to remove most of the cross-linking by-products [44,46,77,79], however, limiting the impact on charge accumulation.

Antioxidants and antioxidant decomposition products are other candidates for ionisable species. The presence of some types of antioxidants in combination with acetophenone has been shown to lead to negative heterocharge in XLPE [46,80]. Degassing in a ventilated oven removed the heterocharges, leading to space charge profiles similar to degassed samples without antioxidants [80], implying that most of the impact can be removed by an appropriate degassing procedure.

2.4.1.4 **Ionic dissociation of water molecules**

Given that even pure water contains a small amount of ionic derivates through self-dissociation, a higher conductivity due to absorbed water can be connected to ionic dissociation of water itself, as in [13]. It has been suggested that this is the most important effect of water on conductivity at low concentrations [81]. As shown in Section 2.2.3.3, an applied electric field will alter the dissociation equilibrium, resulting in an increased number of ions being generated. While the small size of water ions means they can likely move easily through the polymer, mainly contributing to increased conductivity, in [12] accumulation of space charge was suspected to be due to water ions interacting with either impurities or local clusters of water, leading to the ions being trapped. The effect of water dissociation on charge accumulation and transport will therefore likely be dependent on the amount of water absorbed in the polymer, which means that measured results of conducted current and accumulated charge could be cross-checked against measurements of water absorption.

3 Measurement techniques and procedures

3.1 **Materials**

The materials used in the experiments was a commercial cable-grade peroxide-cured XLPE and a commercial cable-grade polyethylene-polyacrylate copolymer semiconductor. Material parameters used in data analysis and for calculations of preconditioning time are listed in Table 1.

Table 1: Material parameters used in data analysis

Material	**Parameters**					
	ε_r	**d**	D_0	E_D	S_0	E_S
	[-]	**[kg m^{-3}]**	**[m^2 s^{-1}]**	**[J mol^{-1}]**	**[kg m^{-3} Pa^{-1}]**	**[J mol^{-1}]**
XLPE	2.3 [a]	922 [a]	$3.11 \cdot 10^{-4}$ [c]	36793 [c]	$1.84 \cdot 10^{-7}$ [d]	-9239 [d]
SC PE-PA	N/A	1135 [b]	$2.02 \cdot 10^{-6}$ [e]	35968 [e]	$3.46 \cdot 10^{-9}$ [e]	-33224 [e]

[a] From XLPE TDS, included in Appendix A

[b] From SC PE-PA TDS, included in Appendix A.

[c] Calculated from measurements of permeability and solubility, described in Appendix B.

[d] Measured as described in Appendix B.

[e] Calculated from water absorption measurements, as described in Appendix B.

3.2 Current measurements and conductivity calculation

3.2.1 Measurement principle

As described in Section 2.2.4.1, measuring the steady-state current is in principle an easy way to obtain the temperature and field dependence of the conductivity, which will provide information on the underlying conduction mechanism. Reaching a steady current in highly insulating materials is not necessarily straightforward, however, as the polarisation time constant can be quite large (e.g. $\tau = \varepsilon/\sigma \approx 230$ days for polyethylene at 20 °C [82]). Long-term exposure to strong electric fields and high temperatures may cause changes in the material, such as morphological changes or oxidation. These changes, as well as space charge accumulation, may affect the conducted current [39], leading to a test object that changes over time. This limits the usefulness of measurements over very long durations for determining the baseline conductivity.

A charging-discharging current measurement utilises the symmetry of polarisation and depolarisation processes, as illustrated in Figure 1. As described in Section 2.2.4.2, the charging current density is given by [51]

$$J_{\mathrm{C}}(t) = \varepsilon_0 E\left(\delta(t) + f(t)\right) + \sigma E \tag{3.1}$$

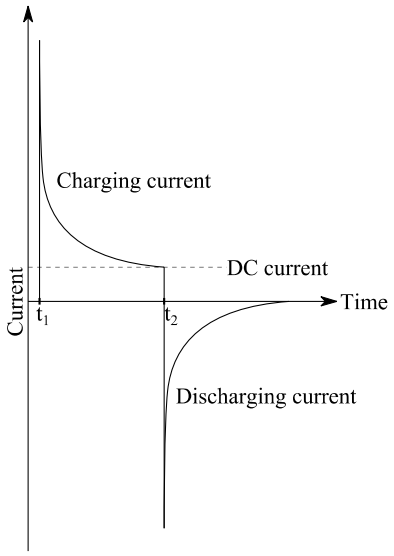

Figure 1. Principle of charging-discharging current measurements. Voltage is applied at t_1. The initial current spike is followed by the decaying polarisation current of the dielectric, which falls towards the steady DC current. At t_2, the voltage is removed, and a discharging current flows.

When the voltage is removed, the discharging current density will be given by [51]

$$J_{\mathrm{D}}(t) = -\varepsilon_0 E\left(\delta(t) + f(t)\right) \tag{3.2}$$

The conductivity can then be calculated from the sum of the charging and discharging currents

$$J_{\mathrm{Tot}} = J_{\mathrm{C}} + J_{\mathrm{D}} = \sigma E \tag{3.3}$$

Replacing the current density with the measured current I, yields

$$\frac{I_{\mathrm{C}} + I_{\mathrm{D}}}{A} = \sigma E = \sigma \frac{U}{d} \tag{3.4}$$

where A is the cross-sectional surface area, U the applied voltage and d the thickness of the dielectric. By considering the test object as a parallel plate capacitor, the capacitance can be written as $C = \varepsilon \frac{A}{d}$, which, combined with (3.4) yields the conductivity as

$$\sigma = \frac{\varepsilon}{UC}\left(I_C + I_D\right) \tag{3.5}$$

From (3.5), it is apparent that that the sum of polarisation and depolarisation currents is in principle independent of time. This means that high amounts of random noise can be compensated for, as it is possible to use the mean of the summed currents over time. A limitation of this method is that several different conductivity mechanisms all have similar electric field and temperature dependence, as shown in Section 2.2, and distinguishing the different mechanisms can be challenging when only measuring steady-state current. Transient current measurements, which also include the time-dependent elements of Equations (3.1) and (3.2), enables more information to be obtained, such as calculating of charge mobility from peaks in the charging current or analysing the discharge current to see if main carrier type changes with temperature or water absorption.

3.2.2 Current measurement setup

The current measurement setup is shown in Figure 2. A high stability FUG HCN 140-35000 HVDC source was connected to a high voltage relay through a resistor. At charging current measurement start, the relay switched to connect the HVDC source to the high voltage electrode, applying the voltage to the test object. For discharging measurements, the high voltage relay switched from the HVDC source to short circuit the test object to ground through a second resistor. A third resistor was placed between the test object and the high voltage relay. A Keithley 6485 picoammeter was used to measure the currents. A second relay was used to ground the picoammeter input connector, protecting the picoammeter from potentially damaging transient currents when switching the high voltage relay. To minimise electrical noise, the relays and resistors, as well as unshielded connecting cables, were placed in a grounded metal box. The test object and electrodes were placed in a perforated grounded metal box in a climate chamber. The cables used to connect the measurement electrode to the switch box, and the switch box to the picoammeter, were low-noise coaxial cables.

As the climate chamber used a compressor and a fan to regulate temperature and humidity, the test objects and connecting electrodes were subjected to significant mechanical vibrations, affecting the measured current. To minimise vibrational noise, the perforated metal box was placed on a vibration dampening mat on a metal plate. The metal plate rested on brass cones with rubber washers. A second vibration dampening mat was placed below the cones. However, even with the vibration dampening in place, the noise levels with the climate chamber switched on were still higher by a factor of 10, varying around $\pm$ 1–5·10^{-12} A, compared to $\pm$ 1–2·10^{-13} A with the climate chamber switched off.

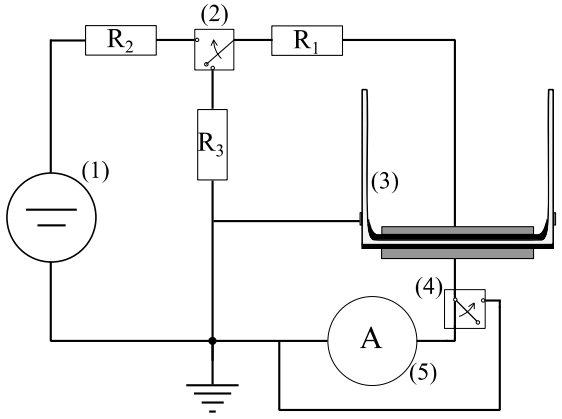

Figure 2. Current measurement setup. (1) HVDC source; (2) High voltage relay; (3) Test object; (4) Low voltage relay; (5) Picoammeter.

3.2.3 **Test objects**

The test objects consisted of XLPE insulation with semiconducting polymer electrodes, shown schematically in Figure 3. These cylindrical test objects have an outer diameter of 50 mm and a height of 40 mm. The bottom of the cylinder contains the insulation system to be tested, as shown in Figure 3. The upper part of the insulation and the upper semiconductor (connected to the high voltage electrode) are Rogowski-profiled, making the electric field between the electrodes relatively homogeneous. The objects were press-cast from extruded XLPE tape and roll-milled semiconducting film at 120 °C, and cross-linked at 170 °C. After casting, the objects were annealed at 130 °C for 15 minutes and degassed at 90 °C for 3 days in a ventilated oven. Capacitances and thicknesses of the Rogowski test objects used in the current measurements are shown in Table 2.

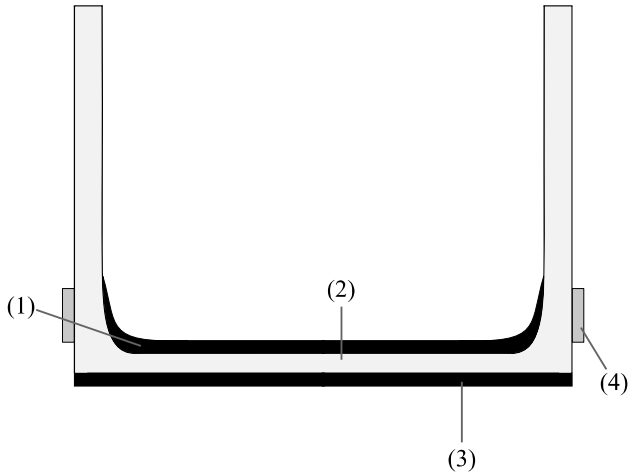

Figure 3. Cross section of Rogowski-profiled current measurement test objects. (1) High voltage semiconducting electrode; (2) XLPE insulation; (3) Measurement electrode; (4) Guard electrode.

Table 2: Rogowski test objects used in current measurements

Test object	Test	Capacitance [pF]	Thickness [mm]
1	Steady state	49	0.78
2	Transient current	117	0.33
3a	Long term current – dry	79	0.48
3b	Long term current – wet	82	0.46

3.2.4 **Preconditioning and measurement procedure**

The water content in the test objects was varied by controlling the temperature and humidity in the climate chamber. The samples were preconditioned at measurement temperature and relative humidity for between 6 and 48 hours, depending on temperature, in order to ensure that the water content in the samples was at equilibrium with the surroundings. The measurements were performed in the same climate chamber used for preconditioning, without removing the test objects before measurement. The measurements were performed at 40, 60 and 80 °C, with preconditioning times as listed in Table 3.

The voltage source was switched on for one hour prior to the measurements to ensure that the source had warmed up, in order to minimise noise and offset. In addition, the voltage level was set 15 minutes prior to charging measurement start, in order to stabilise the voltage output. Before starting the charging measurements, offset and noise levels were determined by measuring the current in the sample for 15 minutes with the high voltage electrode switched to ground. Samples were kept grounded for a period of at least twenty

times longer than the charging time before starting the next measurement, in order to minimise the effect of previous measurements on subsequent measurements.

Three different sets of current measurements were performed. The first set measured the averaged charging and discharging currents, to obtain the temperature and electric field dependence, and was performed at all three temperatures and with 10, 30, 60 and 90% relative humidity (RH). The use of time-averaged currents meant that these measurements could be performed with the climate chamber on throughout the measurement.

The second set of measurements was performed to investigate short-time transient currents. To minimise noise, the climate chamber was switched off approximately 15 seconds before the start of the charging current measurements and kept off for 50 seconds of charging and 50 seconds of discharging measurements. The short duration meant that the temperature drop was minimal, measured to be around 1 °C in the climate chamber at 80 °C. The temperature in the test object was likely much less, given that it was located between the solid brass high voltage and ground electrodes.

The third set of tests measured the charging and discharging currents over 14 days, for comparison with the space charge measurements. These measurements were only performed at 40 °C, in dry conditions and at 85% RH. Similar to measurement set 2, the climate chamber was switched off for 15 seconds prior to and 50 seconds after switching to charging and discharging measurements.

Table 3: Preconditioning and measurement conditions for current measurement samples

Temperature [°C]	Relative humidity [%]	Water content [kg m^{-3}]	Preconditioning time [h]
40	10	0.005	48
	30	0.014	
	60	0.028	
	90	0.042	
60	10	0.010	24
	30	0.031	
	60	0.062	
	90	0.093	
80	10	0.020	6
	30	0.061	
	60	0.122	
	90	0.183	

3.3 Detection of space charge and the pulsed electroacoustic method

3.3.1 Introduction

The pulsed electroacoustic (PEA) test method is a non-destructive measurement technique used to detect the placement, polarity and magnitude of charge concentrations within an insulation material sample. It is one of several methods that use the agitation of charges in a sample to generate detectable signals. The methods differ in both agitation and detection methods, and can be divided into three main categories: the first uses pressure waves to agitate charges [83-85], the second uses the propagation of heat to agitate charges [86-88] and the third category, which PEA is a part of, agitates the charges by applying voltage pulses [89]. A summary of these, in addition to several other non-destructive and destructive methods, can be found in [90]. For details on the pressure wave methods, see [83-85,91,92], and for the thermal methods, see [86-88,93].

The PEA method is the most well-established test method in the third category. Here, charges in the sample are perturbed by voltage pulses, creating acoustic waves that are measured by a piezoelectric sensor. Originally published as a method for measuring electric fields at an electrode-dielectric interface [89], it was further developed to also measure charge distribution in the bulk [94,95]. Improvements and modifications of the test method include cable geometry measurements [96,97], the possibility of measuring 3D charge distributions [98] and measurement setups that can withstand harsh environments [99,100]. Techniques to improve the resolution of space charge measurements to a sub-nanometre scale by using femtosecond laser pulses for signal generation has also been proposed [101].

3.3.2 Measurement principle

The sample is placed between two electrodes, as depicted in Figure 4a, and a voltage pulse is applied to one of the electrodes. The change in electric field induces a force on the charges in the sample, which causes them to slightly shift position, as shown in Figure 4b. In turn, the movement of the charges cause neighbouring particles to shift, creating a pressure wave which travels through the sample. A piezoelectric sensor placed behind the ground electrode is used to detect the pressure wave, as shown in Figure 4c. Positive and negative charges will move in opposite directions when affected by the electric pulse, resulting in signals with opposite signs. If charges with opposite polarities occupy an area less than the spatial resolution of the equipment, the PEA method will detect the net charge in the area.

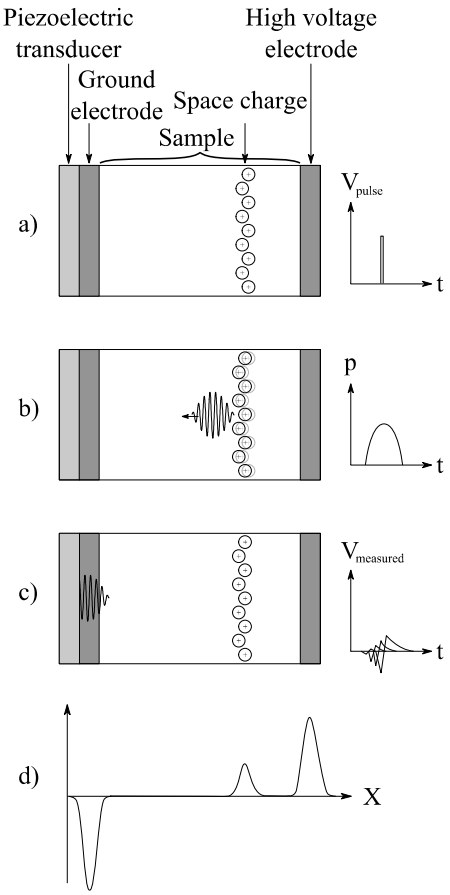

Figure 4. Principle of the PEA method with DC voltage applied. a) A voltage pulse is applied to the high voltage electrode. b) The voltage pulse causes charge present in the sample to shift position, generating a pressure wave. c) The pressure wave travels through the sample and the ground electrode and is detected by a piezoelectric sensor. d) Deconvoluted space charge signal.

3.3.3 **Pulsed electro-acoustic measurement setup**

The PEA setup used, schematically shown in Figure 5, is the commercial Pulsed ElectroAcoustic Non-destrUctive Test Setup (PEANUTS). It consists of an HVDC source, a pulse generator, the measurement and amplifier modules and a digital oscilloscope with a PC link. The HVDC source, a Matsusada HEOPS-10B2 ±10 kV, is coupled to the high voltage electrode of the sample through a 20 MΩ resistor. To enable simultaneous application of pulse and DC voltage, the pulse generator is connected to the high voltage electrode through a capacitor. The electric pulses have an amplitude of 600 V with a 5 ns pulse width, and are applied at a frequency of 400 Hz. The measurement module, which contains the ground electrode and the piezoelectric sensor, is placed in a climate chamber. The amplifier, which is sensitive to temperature and humidity extremes, is placed outside the climate chamber in a separate module. This enables measurements at temperatures up to 85 °C, with up to 85% RH. A LeCroy WR62Xi oscilloscope operating at 5 GHz sampling rate is used to record the signal. In order to reduce background noise, each measurement collects data for one minute and averages the result. The theoretical resolution of the system is around 10 µm with a sensitivity of 0.2 C/m^3 [102], but the actual resolution is dependent upon the sample material, electrode configuration and measurement conditions. Experience with the system has shown, for example, that higher temperatures decrease resolution. Higher humidity does not appear to affect the measurement sensitivity or resolution.

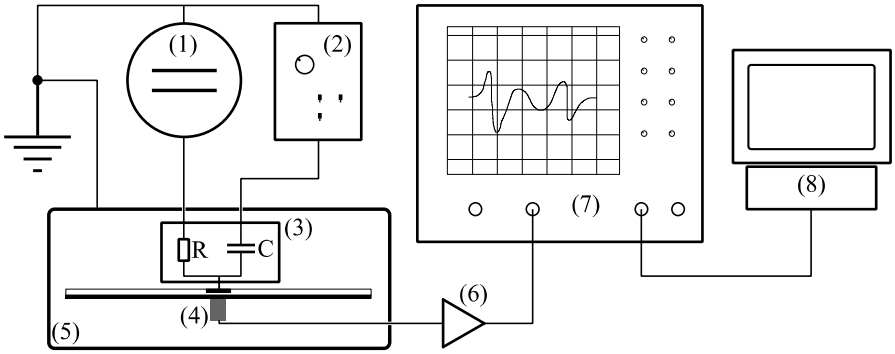

Figure 5. PEA measurement setup. (1) HVDC source; (2) Pulse generator; (3) High voltage electrode; (4) Piezoelectric sensor; (5) Climate chamber; (6) Signal pre-amplifier; (7) Oscilloscope; (8) Computer for data storage.

3.3.4 **Signal processing**

Due to the sensor, amplifier and transmission cables affecting the signal, the recorded data is run through a filtering and deconvolution procedure to extract the charge profile. A Matlab script developed by SINTEF, based on the principles originally presented by Maeno [95] and further developed by others [103-105], is used as the basis for the signal

processing. A digital low pass filter is used on the time-domain signals to suppress high frequency noise, while a Blackman frequency window is used on the signals in the frequency domain to eliminate ringing noise. The deconvolution procedure uses signals recorded without space charge in the sample as a basis. These signals were found by applying low DC voltage for a short time prior to measurement and then recording with voltage on. Both positive and negative polarity signals were recorded. By calculating the average of the two polarities, as illustrated in Figure 6, effects of fast space charge (i.e. charge fast enough to accumulate during calibration) will be eliminated. The average signal is also used to find the attenuation and dispersion factors of the pressure wave.

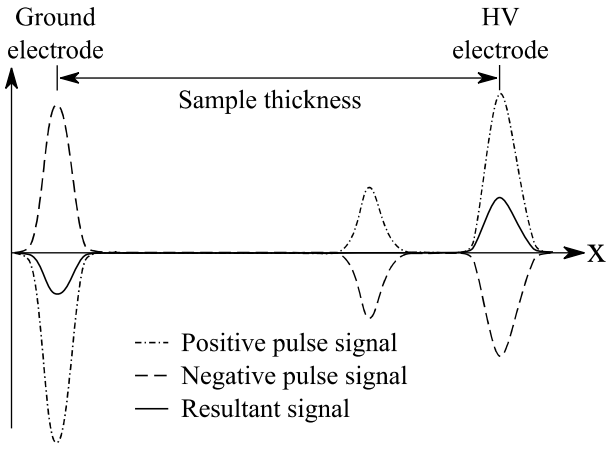

Figure 6. Signals with positive and negative DC polarity, and the resultant signal used as deconvolution basis. Signal amplitudes are not to scale.

3.3.5 **Signal interpretation**

Reading a calibrated PEA result is fairly straightforward; given that the amplitude of the voltage signal corresponds to the concentration of charge, the polarity of the signal corresponds to the polarity of the charge and the delay between a signal and the first electrode corresponds to the position of the charge in the sample, these can all be included in the signal processing procedure and read directly in the result. The width of the signal will also indicate the spatial distribution of the charge. However, an issue appears when charge concentrations with opposite polarities are in close proximity to each other. An illustration of this is shown in Figure 7, where a larger positive and smaller negative charge peak results in a positive charge peak with a secondary positive peak, and no net negative charge. Both peaks have different centre points and widths, the result of which is that the resultant primary positive peak will have a steeper incline on the side of the contributing negative peak.

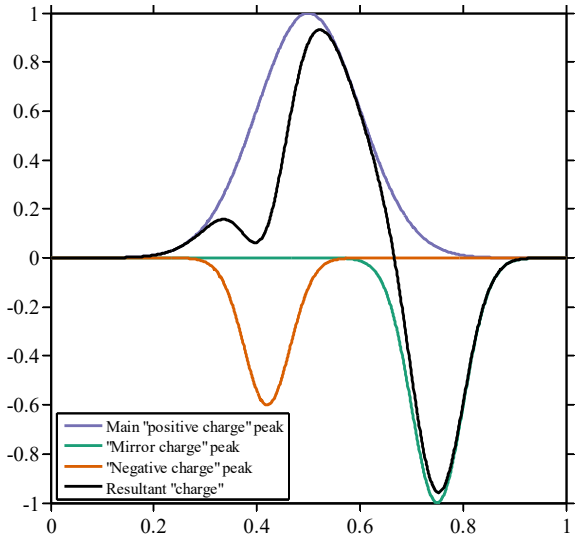

Figure 7. Illustration of interaction between positive and negative charge peaks.

3.3.6 **Test objects**

The test objects were 100 mm diameter XLPE plates with semiconducting polymer electrodes, as shown in Figure 8. The lower ground electrode had the same diameter as the XLPE insulation, while the upper high voltage electrode was 8 mm in diameter. The small high voltage electrode ensured that the distance from high voltage to ground was the same as for the PEANUTS high voltage electrode configuration, keeping the risk of flashovers low. This is especially important at high temperature and humidity levels.

The sample thickness was about 0.3 mm, which was also the thickness of the semiconductor electrodes. Manufacturing of the samples was done by hot pressing extruded XLPE and rolled semiconducting polyethylene. Initial hot pressing was done at 120 °C, with subsequent cross-linking at 170 °C. After pressing, the samples were annealed for 15 minutes at 120 °C and degassed at 90 °C for 3 days. These procedures removed any frozen-in stress and reduced the amount off cross-linking by-products present in the samples.

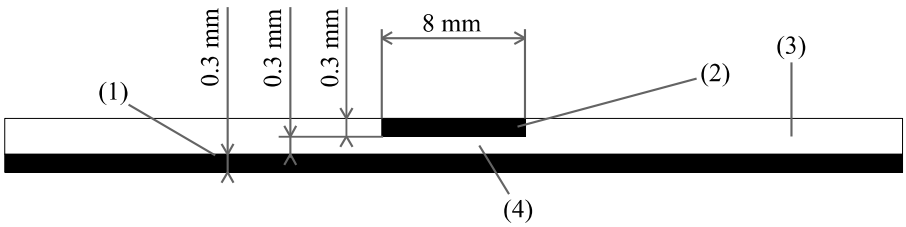

Figure 8. PEA sample geometry. (1) Lower semiconducting electrode; (2) Upper semiconducting electrode; (3) XLPE insulation; (4) Area under electric stress.

3.3.7 **Preconditioning and measurement procedure**

Each of the samples were preconditioned in the climate chamber prior to measurement. By controlling the temperature and relative humidity, the water content in the samples was varied. The preconditioning time depended on the temperature, an overview of which can be found in Table 4.

Table 4: Preconditioning of PEA samples

Temperature [°C]	Water content [ppm]	Preconditioning time [days]	Preconditioning method
20	5	4	60 °C < 1% RH, measurement at 20 °C 25% RH
	18	10	Climate chamber at 85% RH
	> 20	4	60 °C in water, measurement at 20 °C 75% RH
40	3	1	Climate chamber at 0% RH (~4% RH in chamber)
	44	1	Climate chamber at 85% RH
60	1	1	Climate chamber at 0% RH (< 1% RH in chamber)
	95	1	Climate chamber at 85% RH
80	1	1	Climate chamber at 0% RH (< 1% RH in chamber)
	187	1	Climate chamber at 85% RH

The applied DC voltage was 10 kV for all measurements. The time between measurements was short at the start of a series and increased to intervals of 1 hour during the first day of measurement. For the rest of the charging period, the interval was 24 hours. After 14 days of charging, space charge discharge was measured using the same measurement intervals. An overview of the measurement intervals can be found in Table 5.

Table 5: Overview of PEA measurement intervals

Time of measurement, *t*		
[min]	**[h]**	**[d]**
7		
12		
22		
One measurement every 20 minutes until *t* =		
122	2	
	One measurement every 30 minutes until *t* =	
	4	
	One measurement every hour until *t* =	
	24	1
		One measurement every 24 hours until *t* =
		14

When the DC voltage was applied, the induced charges at the electrodes are much larger than the space charge, which makes measuring the accumulated space charge distribution difficult. In order to increase the sensitivity of the measurements, the DC voltage was switched off during measurement. A voltage-off signal was then recorded, and the voltage switched on again. Signals with DC voltage applied were recorded before and after each voltage-off measurement. These were used to compare the apparent applied DC voltage, i.e. the integral of the electric field from the space charge signal, to the actual voltage applied by the HVDC source. By comparing the calculated apparent DC voltage to the applied DC voltage, a check of the numerical treatment of the data can be done. In addition, by comparing the voltage on signals recorded just before and just after each voltage-off measurement, any potential effects of switching off the voltage can be found. Qualitatively checking this for each measurement series, no significant difference was found between pre- and post-voltage-off measurements.

4 Experimental results and discussion

4.1 **Introduction**

This chapter contains the experimental results found in the measurements, with accompanying discussion sections. The discussion is primarily focused on two external stress factors, namely temperature and water absorption. The response of the insulation system to changes in the electric field will also be used as an input to discuss the underlying conduction mechanisms. The effects on conducted current, steady-state current (Section 4.2), time-dependent current (Section 4.4), and the accumulation of space charge (Section 4.3) will be investigated. Section 4.4 also contains a short discussion comparing the time development of conducted current and accumulated space charge measurement results.

4.2 Conduction current and mechanisms

4.2.1 Introduction

This series of measurements was performed to relate the temperature and electric field dependence of the XLPE samples to conduction mechanisms commonly found in the literature:

- Schottky injection [16,35], Section 2.2.2.2
- Poole-Frenkel conduction [16,38,39], Section 2.2.2.3
- Hopping conduction [29,30,39], Section 2.2.2.1 and 2.2.3.1
- Space charge limited current [16,40], Section 2.2.2.4
- Ionic dissociation, Section 2.2.3.2 and 2.2.3.3 (in combination with other mechanisms)

The results were analysed with regards to electric field and temperature response, and with regards to the response to water absorption.

4.2.2 Measurement procedure

The measurements were performed with the current measurement setup presented in Section 3.2.2. Charging and discharging currents were measured for 30 minutes at 40 °C, and 15 minutes at 60 and 80 °C. The time average of the last 10 minutes of the currents was used to calculate the conductivity, using Equation (3.5).

4.2.3 Results

The average measured conduction currents are plotted in Figure 9. The measured currents are sorted into categories by water content (see Table 6) such that the maximal deviation from the average water content in each category was 20% or less. The highest and lowest categories only contain results from measurements at a single temperature and have not been included in the single conduction mechanism analysis.

As can be seen in the figure below, the conducted current increased with increasing temperature, applied field and water content. The electric field dependence is exponential, which excludes ohmic conduction, but does not exclude any of the other proposed mechanisms. The temperature dependence is exponential as well, which fits well with all four of the conduction mechanisms.

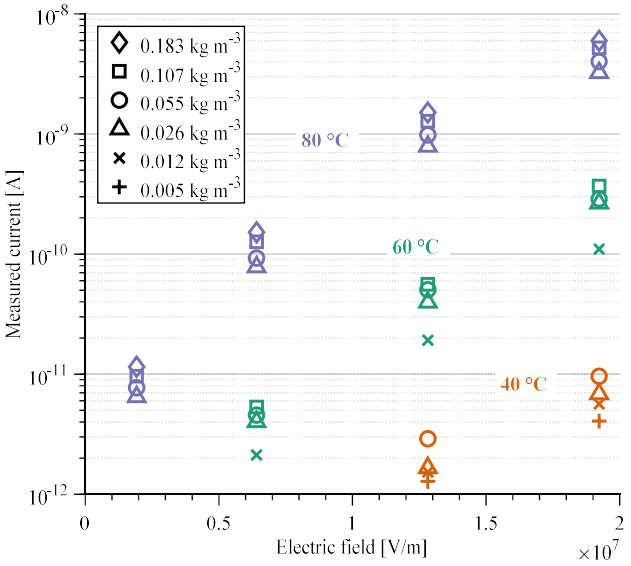

Figure 9. Measured current against applied electric field at 40, 60 and 80 °C.

Table 6: Water content categories for conduction current measurements

Category			Measurement conditions		
C_{av} [kg m^{-3}]	ΔC [kg m^{-3}]	$\Delta C/C_{av}$ [-]	T [°C]	RH [%]	C [kg m^{-3}]
0.005	-	-	40	10	0.005
0.012	0.002	0.16	60	10	0.010
			40	30	0.014
0.027	0.005	0.20	80	10	0.020
			40	60	0.028
			60	30	0.031
0.055	0.010	0.18	40	90	0.042
			80	30	0.061
			60	60	0.062
0.107	0.015	0.14	60	90	0.093
			80	60	0.122
0.183	-	-	80	90	0.183

To determine the conduction mechanism dominant in the XLPE samples, the electric field and temperature dependence of the conducted current is compared to the predicted dependencies of the different conduction mechanisms. As presented in Section 2.2, several conduction mechanisms have been suggested for XLPE. Here, four of the most commonly used – Schottky injection, Poole-Frenkel conduction, hopping conduction and space-charge limited current – will be fitted to the data in Figure 9. The analysis was

performed according to Table 6, meaning any systematic difference between the samples with different water content will be an effect of water absorption.

Instead of altering existing conduction mechanisms, it is possible that absorbed water introduces a second charge carrier species in addition to the existing one, for instance through ionic dissociation of water molecules. In Section 4.2.4.2 this is investigated by assuming that an independent ionic dissociation mechanism is added to a conduction mechanism found likely to be dominant in Section 4.2.4.1.

4.2.4 Conduction mechanisms

4.2.4.1 Single dominant conduction mechanism

The equations used for fitting are presented in Table 7, and are simplifications of the equations describing the temperature and electric field dependence of the conduction mechanisms, as presented in Section 2.2.2. Each water content category was treated separately, and the mechanism assumed to be dominant for the entire measurement range. The equations were fitted to the data with Matlab's fminsearch function, which uses an unconstrained nonlinear multivariable minimisation based on the Nelder-Mead algorithm [106]. The conductivity is exponentially dependent on temperature and more-than-linearly dependent on electric field. In order to weight the entire dataset equally in the curve-fitting, a non-linear error function was used:

$$S(A,B,C)=\sum_{T,\mathrm{E}}\left(\log\left(\sigma_{\mathrm{c}}(T,E,A,B,C)\right)-\log\left(\sigma_{\mathrm{m}}(T,E)\right)\right)^2 \tag{4.1}$$

Here, S is the sum of the error estimates and σ_{c} is the calculated conductivity for a given temperature and electric field, based on the fitting parameters A, B and C. σ_{m} is the conductivity for the same temperature and electric field taken from the measured data set. For each conduction mechanism, A, B and C were varied in order to minimise S in Equation (4.1).

Table 7: Equations used in the fitting procedure. A, B and C are the fitting parameters, unique for each conduction mechanism

Conduction mechanism	Fitting equation	Base equation (from Chapter 2)	Equation number
Schottky injection	$\sigma=\frac{AT^2}{E}\exp\left(-\frac{B}{k_{\mathrm{B}}T}\right)\exp\left(\frac{C\sqrt{E}}{T}\right)$	(2.3)	(4.2)
Poole-Frenkel	$\sigma=A\exp\left(-\frac{B}{k_{\mathrm{B}}T}\right)\exp\left(\frac{C\sqrt{E}}{T}\right)$	(2.4)	(4.3)
Hopping conduction	$\sigma=\frac{A}{E}\exp\left(-\frac{B}{k_{\mathrm{B}}T}\right)\sinh\left(\frac{CE}{T}\right)$	(2.2), (2.6)	(4.4)
Space-charge limited current	$\sigma=\frac{A}{E}\exp\left(-\frac{B}{k_{\mathrm{B}}T}\right)V^C$	(2.5)	(4.5)

4.2.4.1.1 **Schottky injection**

Using Equation (4.2), Schottky injection was fitted to the measured currents as shown in Figure 10, with the resulting parameters being listed in Table 8. As can be seen in the figure, the coefficients found by the procedure provide a reasonable fit, which is also reflected by the low error estimates (*S* in Table 8). From the figure, the largest difference between measurements and the fitted curves appears to be at 40 °C, likely from the low currents at 40 °C being more susceptible to noise.

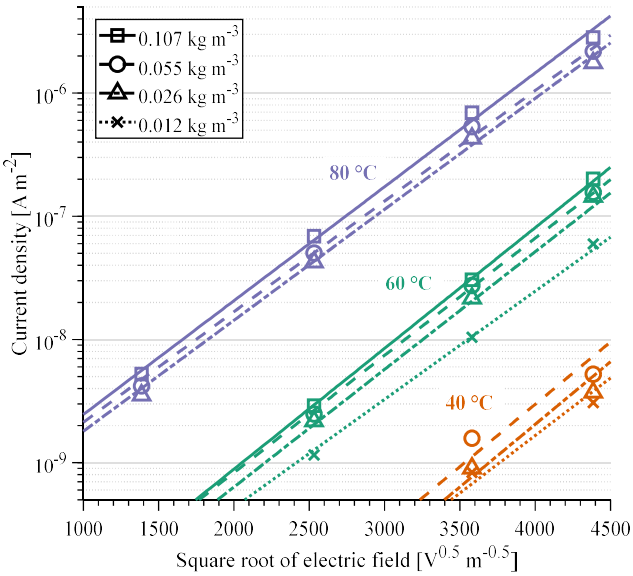

Figure 10. Current density and fitted curves for measured results at different levels of water content. The lines are fits based on Schottky injection.

Table 8: Fitting parameters for Schottky injection

WC*	*A*	*B*	*C*	*S*	ε_r
[kg m^{-3}]	[A m^{-2} K^2]	[eV]	[m$^{0.5}$ K V$^{-0.5}$]	[-]	[-]
0.012	$6.85 \cdot 10^4$	1.39	0.67	0.11	0.43
0.026	$5.57 \cdot 10^8$	1.65	0.73	0.21	0.36
0.055	$1.09 \cdot 10^8$	1.59	0.73	0.29	0.36
0.107	$1.38 \cdot 10^9$	1.66	0.75	0.06	0.34

* Water content

Looking at the changes of the fitting parameters with water content, parameter *C*, which contains the field dependency, slightly increases as the water content increases, while the two other parameters do not uniformly change. The largest change is from the

0.012 kg m^{-3} to the 0.026 kg m^{-3} water content levels. The activation energies, corresponding to *B* in Table 8, were found to be 1.39–1.66 eV, which is in the upper range of or above the activation energies found in [35].

The apparent relative permittivity can be calculated from fitting parameter *C* using Equation (4.2) and (2.3), yielding

$$\varepsilon_r = \frac{e^3}{4\pi\varepsilon_0 k^2}\frac{1}{C^2} \tag{4.6}$$

The calculated permittivity for each level of water content is listed in Table 8, and are between 0.34 (highest water content) and 0.43 (lowest water content). The relative permittivity for dry XLPE is 2.3. While alteration of permittivity due to high local concentration of water is one of the possible effects of water absorption, it should increase rather than decrease the permittivity. While some discrepancy is expected due to noise in the measurements, the values in Table 8 are significantly lower than the generally listed XLPE value of 2.3. Given this large difference, unmodified Schottky injection can be ruled out as a conduction mechanism.

Including the space charge modification of the electric field for the Schottky mechanism using the method from [35,36], the fitting parameter *C* can be used to find the modification term:

$$\gamma = \frac{e^3}{4\pi\varepsilon_0\varepsilon_r k^2 C^2} \tag{4.7}$$

Calculating γ from the parameters in Table 8, and using a constant $\varepsilon_r = 2.3$, yields $\gamma = 0.19$ for a water content of 0.012 kg m^{-3} and 0.15 for a water content of 0.107 kg m^{-3}. According to [36], this means a Schottky injection process dominated by homocharge. The small difference from low to high water content could indicate a small reduction of the local electric field at the cathode, reducing injection, but given the uncertainties in the measurement series it is likely too small to be significant. In addition, the comparison of those two categories of water content does not isolate the effect of water content from other variables, as the lower water content category contains measurements at 40 and 60 °C while the higher water content category contains measurements at 60 and 80 °C. Comparing the two middle categories, which both contain measurements at three temperatures, reinforces the point; the value of γ in both of those is identical at 0.16. In addition, as will be seen in Section 4.3, the space charge measurements do not show an increase in homocharge with absorption of water; this only occurs at 40 °C.

4.2.4.1.2 **Poole-Frenkel conduction**

For Poole-Frenkel conduction, Equation (4.3) was fitted to the measured data. Due to the similarity of the Schottky and Poole-Frenkel equations, the results of the fitting procedures are quite similar, as shown in Figure 11 and Table 9. This is also evident in the error estimates. None of the fitting parameters showed any systematic change with the water content. For Poole-Frenkel conduction, a change in A would mean a change in either the density of states in the conduction band, a change in the density of donors or a change in charge mobility. Of these, the latter is more likely, as water molecules have been found to be shallow traps for electrons [67]. A change in B would mean a change in the effective barrier height. Changes in the field-dependent C parameter would likely be related to the trap distribution, and water acting as shallow traps would perhaps affect this, but the changes in the C parameter are fairly small compared to A and B. Disregarding that the changes in the parameters do not appear to be uniformly dependent on the water content, the changes from 0.012 kg m^{-3} to 0.107 kg m^{-3} would comprise an increase in charge mobility of 10^5 combined with an increased barrier height of 0.3 eV. The fact that opposing changes in A and B are needed to obtain good fits when the water content increases makes it less likely that Poole-Frenkel conduction is a good description of the conduction process when water is absorbed.

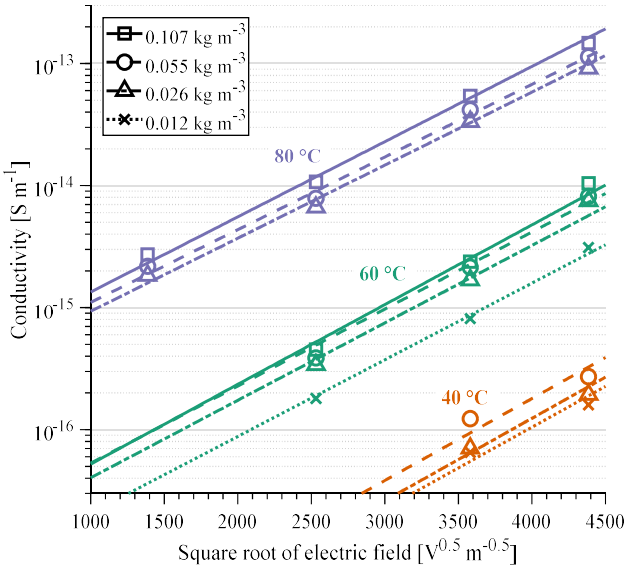

Figure 11. Conductivity and fitted curves for measured results at different levels of water content. The lines are fits based on Poole-Frenkel conduction.

Table 9: Fitting parameters for Poole-Frenkel conduction

WC* [kg m^{-3}]	A [S m^{-1}]	B [eV]	C [m$^{0.5}$ K V$^{-0.5}$]	S [-]	ε_r (no traps)	ε_r (single trap level)
0.012	$4.74 \cdot 10^3$	1.39	0.48	0.08	0.84	3.35
0.026	$4.86 \cdot 10^7$	1.63	0.49	0.17	0.82	3.28
0.055	$9.51 \cdot 10^6$	1.58	0.48	0.23	0.83	3.31
0.107	$3.93 \cdot 10^8$	1.69	0.50	0.11	0.77	3.09

* Water content

Using Equation (4.3) and (2.4), the apparent relative permittivity for Poole-Frenkel conduction can be expressed by

$$\varepsilon_r = \frac{e^3}{4\pi\varepsilon_0 k^2}\frac{1}{C^2} \tag{4.8}$$

for a system with no trap levels being present, and

$$\varepsilon_r = \frac{e^3}{\pi\varepsilon_0 k^2}\frac{1}{C^2} \tag{4.9}$$

for a system with a single trap level.

For no trap levels, the apparent relative permittivity in the measurements was between 0.77 and 0.84, significantly below the expected value of 2.3. For a single trap level, it was found to be between 3.09 and 3.35. This means that Poole-Frenkel conduction with traps provide a better fit than trapless Poole-Frenkel conduction. Given the variety of chemical impurities and physical imperfections that can act as charge traps, it seems likely that the trap distribution is more complex than the relatively simple single trap level used here, which might be the explanation for the difference in calculated ε_r. The activation energy, $B = 2\theta$ in Table 9, was found to be 1.39–1.69 eV, which is similar to what was reported for XLPE in [39], and higher than what was found for HDPE in [38].

In summary, while Poole-Frenkel conduction appears to provide good fits with reasonable fitting parameters for all levels of water content, the change in parameters required to obtain the fits is not systematic. This mechanism alone does not appear to be able to accurately describe the effect of absorbed water on the conductivity.

4.2.4.1.3 **Hopping conduction**

The results of fitting Equation (4.4) are presented in Figure 12 and Table 10. As can be seen in the figure, hopping conduction provides a reasonable fit to the measured data. The difference between the fitted curves and the results were larger than for the previous mechanisms, as is reflected in the larger error estimates. The activation energy was calculated to be between 1.3 and 1.6 eV, which is higher than what was found in [30], but corresponds with results reported in [39]. No clear correlation was found between the fitting parameters in Equation (4.4) and the water content. For hopping conduction, a change in A could be due to a change in the number of charge carriers, which would be expected if water ions are the carrier source. It could also mean a change in the hopping distance, or a charge in the average jump frequency. The jump frequency is unlikely to change with water content, as is the hopping distance; jump frequency is mostly dependent on temperature, while hopping distance is likely to be related to polymer morphology. B is related to the barrier height, which is related to the average trap depth. A change in C would comprise a change in hopping distance. It is possible that water could act as traps for electronic carriers, but this would likely be shallow rather than deep traps and should not affect the barrier height or the average hopping distance.

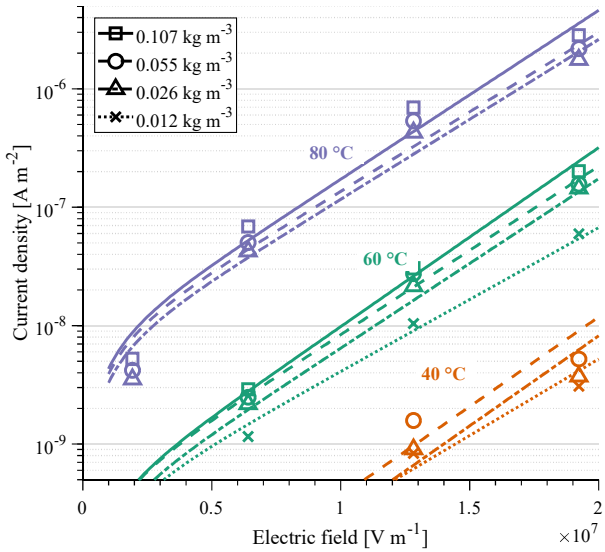

Figure 12. Current density and fitted curves for measured results at different levels of water content. The lines are fits based on hopping conduction.

Table 10: Fitting parameters for hopping conduction

WC* [kg m^{-3}]	A [A m^{-2}]	B [eV]	C [m K V^{-1}]	S [-]	a [nm]
0.012	$3.17 \cdot 10^{10}$	1.31	$9.31 \cdot 10^{-5}$	0.27	16.0
0.026	$1.99 \cdot 10^{14}$	1.56	$1.10 \cdot 10^{-4}$	1.08	18.9
0.055	$3.79 \cdot 10^{13}$	1.50	$1.09 \cdot 10^{-4}$	1.27	18.8
0.107	$1.82 \cdot 10^{14}$	1.55	$1.16 \cdot 10^{-4}$	0.67	20.0

* Water content

The hopping distance was calculated from fitting parameter C through Equation (4.4) and (2.2), yielding

$$a = \frac{2k_{\mathrm{B}}C}{e} \tag{4.10}$$

As shown in the table, the hopping distance was found to be between 16 and 20 nm. This corresponds closely with what was found in [39], and is also close to what can be inferred from the field-dependent parameter in [30]. For electronic hopping, the expected limiting distance depends on the charge carrier. For holes, where movement takes place along the polymer chains, the separation between chains, expected to lie around 0.5–1 nm, is the limiting factor, which is much lower than was found here. Electron movement likely takes place in the amorphous regions, as shown in [27], and will not be restricted to the polymer chains. Traps that would likely act as localisation sites for electron movement have previously been found to occur with an average distance of 10–20 nm [107,108], which would correspond well to the hopping distance found in this work. Ionic hopping, on the other hand, would be dependent on polymer morphology. The thickness of lamellae in crystalline regions in polyethylene have been found to be in the tens of nanometres range [109,110], which is the same range as the hopping distances found here. As crystalline regions are considered impermeable to molecules or ions, due to the constrained nature of polymer chains in these regions, they would constitute barriers to ion movement, and conduction of ions would be restricted to the amorphous regions. Previous studies have found ionic hopping distances to be affected by crystallinity in polypropylene [111]. It is therefore natural to also consider ionic carriers for hopping distances in this range.

4.2.4.1.4 **Space-charge limited current**

The space-charge limited current (SCLC) mechanism predicts a current density that is proportional to V^n, as shown in Section 2.2.2.4. An Arrhenius relation was assumed to be valid for the temperature dependency, resulting in conductivity from SCLC as described by Equation (4.5) in Table 7. Using the fitting procedure resulted in the parameters shown in Table 11.

Table 11: Fitting parameters for space-charge limited current

WC*	*A*	*B*	*C*	*S*
[kg m^{-3}]	[A m^{-2}]	[eV]	[-]	[-]
0.012	$7.77 \cdot 10^{-4}$	1.24	3.51	0.06
0.026	$1.81 \cdot 10^{3}$	1.47	2.87	1.12
0.055	$3.84 \cdot 10^{2}$	1.42	2.86	1.11
0.107	$9.91 \cdot 10^{4}$	1.59	2.90	1.02

* Water content

As can be seen from the straight lines in Figure 13, a power function field dependence of SCLC combined with an Arrhenius temperature dependence fits the measured data well.

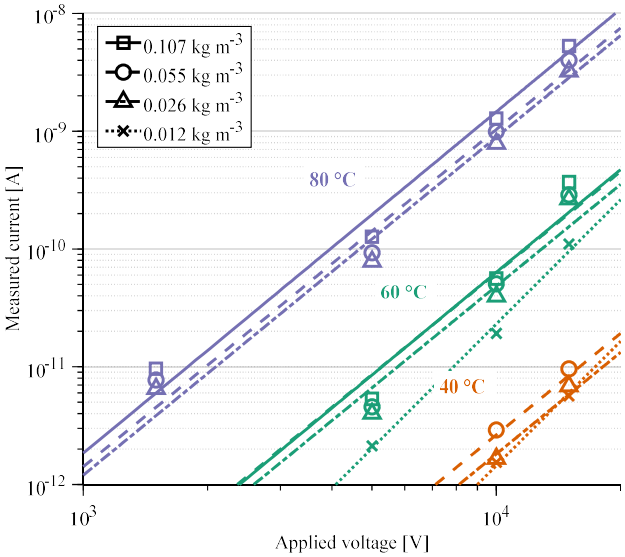

Figure 13. Measured current and fitted lines at different levels of water content. The lines are fits based on SCLC with an Arrhenius temperature relation.

Comparing error estimates, SCLC seems to be a poorer fit than Schottky and Poole-Frenkel conduction, except for the measurements at the lowest water content, and neither

better nor worse than hopping conduction. The *n*-factor, equal to fitting parameter *C*, is between 2.8 and 3.5, indicating that charge traps are limiting factors for conduction [40,112]. However, the change in the *C* parameter, from 3.5 for a dry sample to 2.9 for a wet sample, indicates a reduction in traps, which is the opposite of what would be expected for absorption of water. In addition, most of the change in *C* occurs between the driest and the three other sample categories, while the largest difference in water content is between the three driest and the wettest sample categories. Again, if water is leading to an increase in charge traps, the highest change in *C* would be expected to be between categories with the highest change in water content. A change in parameter *A* would mean a change in the ratio of conduction band electrons to trapped electrons. An increase in the number of traps would be expected to decrease the ratio, while the opposite trend is found in the measurements.

4.2.4.1.5 **Summary**

As presented in the previous sections, distinguishing a single dominating charge mechanism and identifying the effect of water absorption is difficult, given that all of the mechanisms yield reasonable fits. Schottky injection was found to fit when the basic equation was modified to accommodate field distorting space charge, but the change in the γ parameter value did not appear to correspond to changes in water content, and neither to the results of the space charge measurements. Poole-Frenkel conduction was found to fit in the same manner, when a single trap level was present. Fitting hopping conduction predicted a large hopping distance, which would indicate that the charge carriers might either be electrons limited by physical defects or ions hopping between traps formed by the polymer morphology. For space-charge limited current, good fits were found with an Arrhenius-type temperature dependence and traps affecting the voltage dependence.

None of the mechanisms needed parameters outside the expected range of the XLPE being tested to fit. Schottky injection provided the best fit for the highest level of water content and Poole-Frenkel conduction provided better fits for samples with intermediate water content, while Poole-Frenkel and SCLC provided equally good fits at the lowest water content. Hopping conduction provided worse fits than Schottky injection and Poole-Frenkel conduction at all levels of water content.

None of the tested mechanisms revealed any systematic change in parameters, which either means that the effect of water is too small to impact the mechanism except for a general increase in current or that there is a different dominating mechanism or set of mechanisms.

4.2.4.2 **Dual conduction mechanisms**

4.2.4.2.1 **Curve fitting**

As mentioned in Section 4.2.3, it is possible that the absorption of water introduces a second charge carrier mechanism in the sample. Since none of the conduction mechanisms in Section 4.2.4.1 yielded a satisfactory description of the current behaviour when water was absorbed, this section will look at the combined contribution of two different, independent conductivity mechanisms. The first mechanism is assumed to be dominant in dry XLPE and to not be affected by the absorption of water. This would be injection of electrons and holes, for example. The second species is dependent on the amount of absorbed water and is assumed to not be present in dry XLPE. Ionic dissociation of cross-linking by-products or ionic dissociation of water molecules themselves are likely candidates for this mechanism, as both are dependent on water being present to have an effect (see Section 2.4.1). However, as described there, the degassed state of the samples means that dissociable impurities such as cross-linking by-products are unlikely to contribute to the current, and dissociated water molecules are more likely to be the origin of the ions. This means that the increase in current originates from bulk generated carriers, where the conductivity is proportional to the square root of the concentration of water, as defined in Equation (2.9). Checking whether this fits with the measured data can be done by keeping the applied electric field and temperature constant, resulting in the conductivity being expressed as the sum of a humidity-independent and a humidity-dependent term:

$$\sigma = \sigma_{\text{dry}} + k\sqrt{n} \tag{4.11}$$

in which n is the water concentration, σ_{dry} is the conductivity with no water present and k is a fitting parameter, consisting of the humidity-independent parameters in Equation (2.9). As can be seen in Figure 14, the results from the measurements follow this relation well.

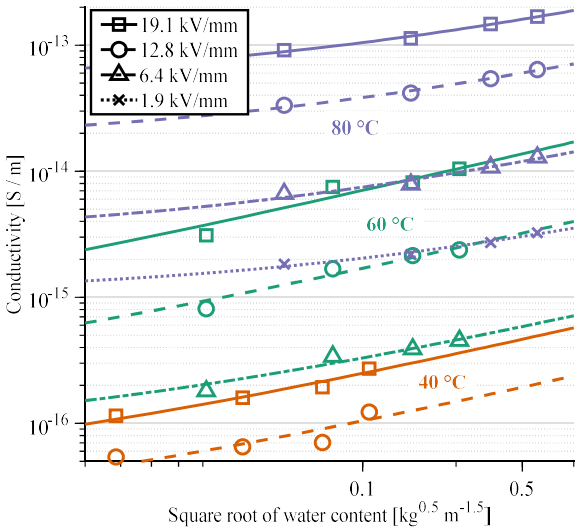

Figure 14. Conductivity and fitted lines plotted against the square root of water content. The lines are fit to Equation (4.11).

Incorporating field and temperature dependency in Equation (4.11) was done on the assumption that the two mechanisms were independent of each other. A general Poole-Frenkel mechanism was assumed to contribute to the dry-state conductivity. This could, however, likely be replaced with any of the other mechanisms, as all the other mechanisms were found to fit the data well. The second mechanism, field-dependent ionic dissociation, provided a square root dependency on concentration and an exponential dependency on field and temperature, using the description in Section 2.2.2.3. Inserting equations from Poole-Frenkel conduction, Equation (2.4), and field-dependent dissociation, Equation (2.9), into Equation (4.11) yields the conductivity as

$$\sigma(E,T,n) = A_{\sigma_{\mathrm{dry}}} \exp\left(\frac{B_{\sigma_{\mathrm{dry}}}}{kT}\right)\exp\left(\frac{C_{\sigma_{\mathrm{dry}}}\sqrt{E}}{T}\right) + A_{\mathrm{k}}\left(\frac{nT^{1.5}}{E^{0.75}}\right)^{0.5} \exp\left(-\frac{B_{\mathrm{k}}}{kT}\right)\exp\left(\frac{C_{\mathrm{k}}\sqrt{E}}{T}\right) \tag{4.12}$$

in which A, B and C are fitting coefficients for σ_{dry} and k, as denoted by their subscripts. A plot of the measurement results and the fitted data is shown in Figure 15. Equation (4.12) appears to be able to describe the measured data well, with parameters as shown in Table 12.

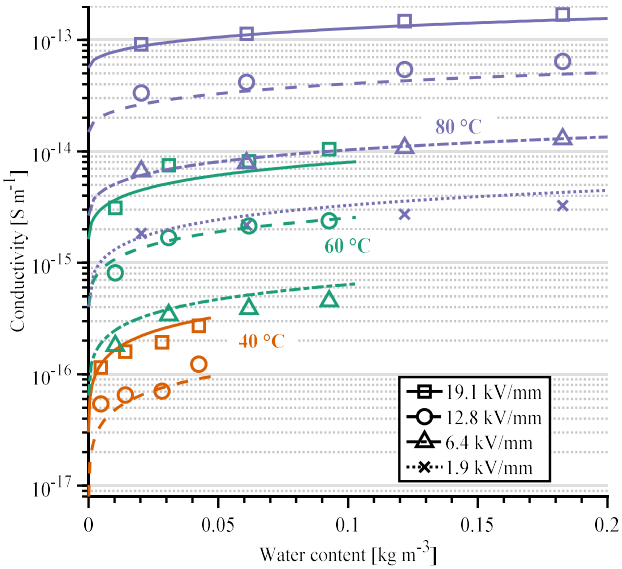

Figure 15. Conductivity and fitted curves plotted against water content. The lines are fits of the entire dataset to Equation (4.12).

Table 12: Dual mechanism conduction, with Poole-Frenkel and field-dependent dissociation

$A_{\sigma dry}$	$B_{\sigma dry}$	$C_{\sigma dry}$	A_k	B_k	C_k
[S m^{-1}]	[eV]	[K m$^{0.5}$ V$^{-0.5}$]	[S m^{-1} m$^{1.5}$ kg$^{-0.5}$]	[eV]	[K m$^{0.5}$ V$^{-0.5}$]
2.46E·10^{10}	1.83	0.41	2.43·10^{6}	1.50	0.59

4.2.4.2.2 **Discussion**

To evaluate the apparently well fitted combination of conduction mechanisms, the physical implications of some of the required fitting parameters were checked. The measured diffusion parameters of water in XLPE (see Appendix B) were also used to evaluate the feasibility of the model.

First, the known relative permittivity of polyethylene was checked against the parameters found from the fitting procedure. The $C_{\sigma\mathrm{dry}}$ and C_k parameters in Equation (4.12) can be used to calculate the apparent relative permittivity for the dry term and the concentration-dependent term, respectively. The dry term yielded $\varepsilon_\mathrm{r} = 1.18$ for a trapless Poole-Frenkel mechanism and 4.72 for a system with one trap level. This means that the trapless system is closest to the real value of 2.3, although a value of 1.18 for a solid is not realistic. The concentration-dependent term gave a relative permittivity value of 0.55, which is even further from the real value of XLPE. This means that even though Equation (4.12) can be well fitted to the measurement data, at least two of the parameters needed to provide the fit are not realistic. It is possible that further exploration of the mechanisms, similar to including the space charge in the Schottky mechanism in Section 4.2.4.1.1, would improve this.

Second, the rate of self-dissociation of liquid water can be used to estimate the number of ions. This can be combined with the measured conductivity to find the apparent mobility of the ions. When considering ionic dissociation, water molecules can exist in two ways in a polymer: as clusters of water where water molecules exist in distributed groups and as completely dissolved water where each water molecule is separated from the rest.

Starting with water clustering, the clusters are assumed to be large enough that the dissociating molecules are completely surrounded by other water molecules, and the dissociation occurs as if in liquid water. At 80 °C, the water self-dissociation constant is 12.6 [113], leading to an ion concentration of $5{\cdot}10^{16}$ ions/m^3 at 90% RH and $6{\cdot}10^{15}$ ions/m^3 at 10% RH. The mobility of water ions in XLPE can be found by finding the conductivity contribution of absorbed water. Using the difference between measured values at 0.18 kg m^{-3} (90% RH) and 0.02 kg m^{-3} (10% RH) in Figure 9, at 80 °C and 2 kV mm^{-1} applied field, this was found to be $1.4{\cdot}10^{-15}$ S m^{-1}. Combining this with the difference in charge carrier concentration leads to an ionic mobility of $1.8{\cdot}10^{-13}$ m^2 V^{-1} s^{-1}. This mobility is in the high end of reported charge mobilities in polyethylene, which lie between 10^{-13}–10^{-15} m^2 V^{-1} s^{-1} [14,114-117].

There are several limitations to this approach, however. The applied field, which would likely increase dissociation, and the effect of the surrounding polymer network, which would likely limit dissociation, could be taken into consideration for a more accurate

calculation. This has not been done, however, as clustering behaviour is not expected of the water molecules in XLPE based on the diffusion profile. For a material that follows Fick's and Henry's laws, as is the case for water in XLPE, the diffusing molecules are not significantly affected by the polymer structure or by each other, and move as separate molecules through the polymer matrix as completely dissolved water. To calculate the mobility is such a case, the absorbed water is considered to behave as water vapour having a temperature of 80 °C and a density of 0.18 kg m^{-3} (90% RH). The resulting self-dissociation constant becomes 56 [113], leading to an ion concentration of 10^{-5} ions/m^3. The corresponding numbers for 80 °C and 0.03 kg m^{-3} (10% RH) are 77 [113] and $5 \cdot 10^{-17}$ ions/m^3 for the self-dissociation constant and ion concentration, respectively. Both of these calculated ion densities are extremely low and would have negligible effect on any currents. In order to obtain the change in conductivity observed in the measurements, the mobility would have to be in the order of 10^8 m^2 V^{-1} s^{-1}. This is many orders of magnitude above the reported values in the literature [14,114-117], in addition to being completely unrealistic – with an applied electric field of 2 kV mm^{-1} the drift velocity would be faster than the speed of light.

Third, the diffusion coefficient of water molecules in XLPE can be used to estimate the mobility of water ions through the Nernst-Einstein-Townsend relation (e.g. [118]). This assumes that there is a single mobile ion or that the two oppositely charged ions have the same mobility. Of course, water ions will not have the exact same mobility as water molecules, as the size and shape of the ions are different to those of water molecules. In addition, the ionisation process does not produce identical ions with opposite charge, but one hydroxide ion comprising of an oxygen and a hydrogen atom, and a proton (which in most systems is quickly hydrated to a $H_{2n+1}O_n$ complex or otherwise bound). Disregarding this, with the diffusion coefficient of water in XLPE at 80 °C being 10^{-9} m^2 s^{-1}, calculated from Table 1, the mobility is calculated to be $3 \cdot 10^{-8}$ m^2 V^{-1} s^{-1}. This is much higher than the estimates for mobilities found in the literature [14,114-117].

4.2.5 **Summary**

As was shown in the sections above, the investigated conduction mechanisms could all be made to fit the data sets, with no one mechanism appearing to fit much better than the others. This is not surprising, as all the mechanisms have almost the same temperature and electric field dependence, i.e. an Arrhenius temperature dependence and an exponential or close-to-exponential electric field dependence. Testing the physical interpretation of the resulting fitting parameters did not result in the exclusion of any of the mechanisms, i.e. none of the fits required unphysical parameters. A major limitation of the mechanisms when tested singularly is that none of them appeared to exhibit systematic change when the water content was changed. For measurements in the driest conditions used in this work, Poole-Frenkel conduction and SCLC fit very well.

Using two separate conduction mechanisms as a basis to describe the whole dataset showed that predictions of the changes in conducted current with water content can be made. However, the base mechanisms tested in this work are likely not to be correct, as the parameters required by the dry mechanism to obtain a good fit resulted in a relative permittivity of XLPE far from the real value. In addition, ionic dissociation of the water molecules themselves, the basis for the water concentration dependence, was found to likely not be large enough to give the measured changes in the conductivity. This means that using the dual-mechanism fit does not hold merit when trying to explain what affects the current in a sample when water is absorbed, at least with these mechanisms. However, the dual-mechanism data fit does work well as an empirical tool to model how the conducted current through XLPE changes due to absorbed water.

4.3 Space charge accumulation and discharge

4.3.1 Introduction

Measurement series on space charge accumulation at 20, 40, 60 and 80 °C and at least two different relative humidities at each temperature were performed. The measurement results for samples with low and high water content are presented in Section 4.3.3 and 4.3.4, respectively, and the most important points are summarised in Section 4.3.5. A discussion on the implications of the results on the effect of increased temperature and water content can be found in Section 4.3.6.

4.3.2 Measurement procedure

Each of the space charge measurement series were performed over a 14-day period at high voltage and a 14-day period with no voltage applied, during which the samples were kept inside a climate chamber. A list of measurement conditions for the space charge measurements can be found in Table 13.

Applied voltage for all measurements was 10 kV, which for a 0.3 mm sample corresponds to an applied electric field of about 33 kV mm^{-1}. The samples varied slightly in thickness, as measured by microscopy analysis of the sample cross-sections after measurement. The sample thicknesses and resulting electric fields are listed in Table 13.

Table 13: Measurement conditions, sample thicknesses and applied electric field for space charge measurement samples

Temperature [°C]	Relative humidity [%]	Water content [kg m^{-3}]	Thickness [mm]	Electric field at 10 kV applied voltage [kV mm^{-1}]
20	25	0.005	0.31	32
	85	0.017	0.28	36
	Wet conditioned at 60 °C		0.32	31
40	4	0.002	0.27	37
	85	0.041	0.25	40
60	< 1	< 0.001	0.31	32
	85	0.088	0.27	37
80	< 1	< 0.002	0.30	33
	85	0.173	0.31	32

4.3.3 Measurement results at low water content

4.3.3.1 Space charge accumulation at 20 °C

The charge distribution in the dry sample is shown in Figure 16. Homocharge was present at both electrodes, which is likely accumulated injected charge. The magnitude of the homocharge peaks increased for the entire 14-day measurement period. Both the anode and cathode peaks were distributed over about a third of the sample thickness, with the peak maxima situated 0.04 mm from the respective electrodes after 14 days. Both of the homocharge peaks started out closer to their respective electrodes, shifting position further into the bulk over time. The peaks moved at different speeds; the anode peak reached its final position after 7 hours, while the cathode peak reached its final position after 2 to 3 days. The reason for the movement of the peaks is not known but may be connected to charge on the electrodes as follows: the measurements in Figure 3.1 are performed with the applied voltage off. At the start of the measurements, the signal is dominated by remnant charge from when the voltage was applied. Over time, the charge injected into the sample becomes large enough to set up a mirror charge in the electrode. This, combined with real charge spreading into the sample, can be observed as the charge peaks 'moving into' the sample. The area between the real and mirror charge peaks is where the signals 'overlap', i.e. it is observed as a no charge zone. If this were to be taken as literal charges distributed due to the trap distribution close to the electrodes, this would mean that there is either an area close to each electrode that is trap-free or that the area consists of unfilled traps, both of which seem improbable.

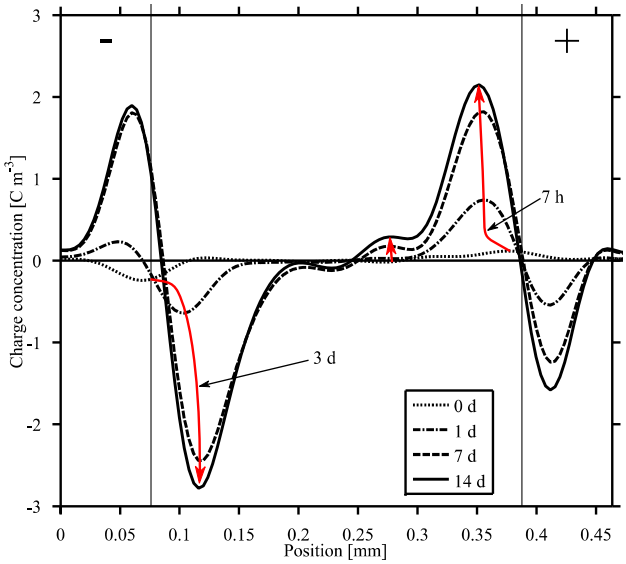

Figure 16. Charge distribution in sample with low water content, at 20 °C and 25% RH. The applied electric field was 32 kV mm^{-1}. The red arrows show the time development of different charge peaks, while the black arrows point to the charge magnitude of a peak at the time given by the accompanying text.

4.3.3.2 **Space charge discharge at 20°C**

The space charge distribution during discharge at 20 °C is shown in Figure 17. Here, accumulated charge can be seen to decrease without significant positional peak movement. The anode homocharge decreased at a faster rate than the cathode homocharge. Figure 18 shows the charge contained in the different peaks designated in Figure 17. Given that the magnitude of charge in the positive and negative charge peaks, and thereby the local electric field near the anode and cathode respectively, is similar at 20 °C, the faster reduction of the positive peak may be an indication of a slightly higher effective mobility of the positive carriers.

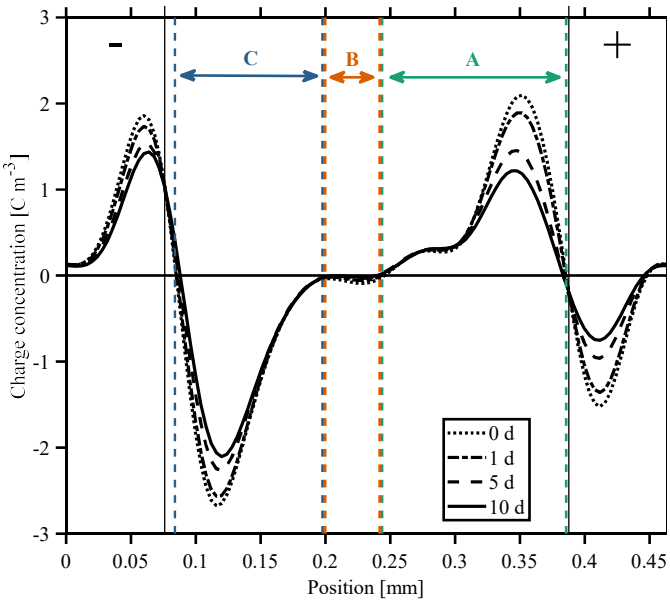

Figure 17. Space charge distribution for discharge of the dry sample at 20 °C. The coloured lines indicate the areas of, from left to right, the cathode peak (C), bulk peak (B) and anode peak (A).

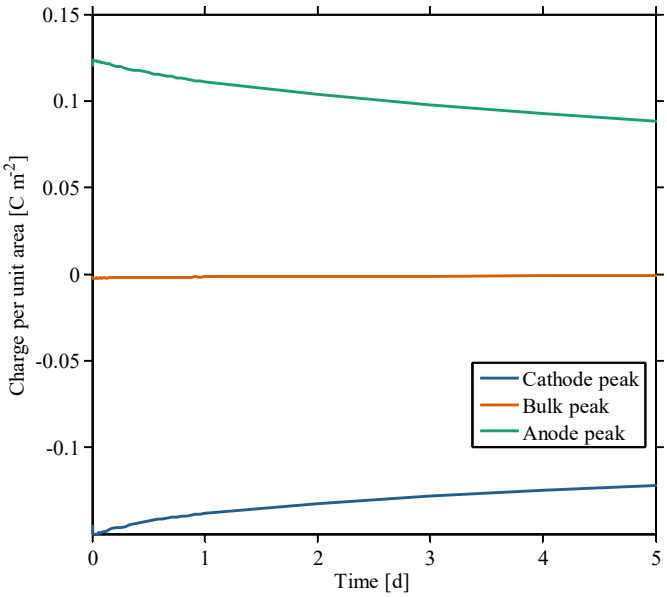

Figure 18. Summed charge per area in the dry sample at 20 °C. The peaks' positional limits correspond to the coloured areas indicated in Figure 17.

4.3.3.3 **Space charge accumulation at 40 °C**

When the temperature was increased to 40 °C, homocharge still accumulated at the anode, as shown in Figure 20. The accumulation rate was higher and the amounts of accumulated charge larger than at 20 °C. This corresponds to an injection-dominated charge distribution, similar to what was found at 20 °C, with a hole injection rate that increases with increasing temperature. A difference from 20 °C is that while the homocharge at the anode increased rapidly for the first 5 hours of the measurement, it then started decreasing until about 24 hours into the measurement. After the 24-hour mark, it started to increase again. This dynamic change in the charge accumulation is suspected to occur when the accumulated positive charge has grown large enough to reduce the electric field near the anode. The reduced field will reduce charge injection. Meanwhile the transport of positive charge away from the anode continues and may even be enhanced by high concentrations of positive charge. This will widen the peak but also reduce its maximum magnitude, leading to an increase in the local electric field. When the local concentration of charge has dropped low enough, the accumulation rate may go up again due to increased injection. Another difference from 20 °C is a second positive charge peak near the anode homocharge peak in Figure 20. This secondary peak increased in magnitude until around 3.5 hours into the test, and then decreased until 13 hours into the test, before increasing again. This is suspected to be an effect of trapped positive and negative injected carriers overlapping; the net positive charge concentration consisting of injected charge carriers at the anode is being reduced due to negative charge carriers from the cathode accumulating in the same area.

At the cathode, the accumulated charge was heterocharge, which increased throughout the measurement period. While the homocharge at the anode built up in a narrow peak, the heterocharge at the cathode was more widespread, with the tail end of the peak reaching about halfway into the sample. This charge has two possible origins: charge generation in the bulk, e.g. ionisation of dissociable impurity groups [77], including water, and injected charge at the anode moving through the sample and accumulating at the cathode [119]. In [34], a similar charge distribution as in Figure 19 was observed at 40 °C and 40 kV mm^{-1} in XLPE with semiconductor electrodes. There, the heterocharge at the cathode was attributed to bulk effects, suggesting the extraction of electrons and movement of low molecular weight polyethylene or impurities from the bulk to the cathode.

Considering bulk generation, an increase in temperature from 20 to 40 °C would be expected to increase the dissociation rate, as per Equation (2.7) and (2.9), and measurable heterocharge would appear if the increase was large enough. Significant accumulation of dissociated positive charge at 40 °C raises the question of where the negatively charged dissociation product is. No net negative charge was observed at 40 °C. This means that for the assumption of the cathode heterocharge being bulk generated to be valid, there

must be significant differences in trapping conditions for positive and negative charge. This can occur if, for instance, the bulk charge is larger positive ions that have lost an electron. The electrons are mobile and can be removed from the sample while the less mobile ions remain. Another possibility is ionic dissociation where the negative ions are much more mobile than the positive ions.

When considering only injected charge, any heterocharge at the cathode would have to have been transported across the sample. However, a similar trap distribution would be expected at the two electrodes, given that they are made with the same process and the same materials, meaning that the peak shapes at the electrodes would be similar at equilibrium. This can be explained by assuming that impurities are the most likely origin of traps near the electrodes, and that there is a decreasing impurity concentration with increasing distance from the electrode. Both assumptions are supported by the literature, as carbonyl groups have been found to be traps for both electrons and holes (e.g. [67,69]) and to diffuse into XLPE insulation [63]. Positive charge transported to the cathode will first arrive at the traps nearer to the bulk, meaning those traps will be filled first. In addition, injected negative charge would also be expected to affect the cathode charge peak. With similar trap distributions, it is possible that the peaks at the cathode and anode would attain similar shapes over time, but as can be seen in the measurements this did not occur during the 14 days of voltage stress.

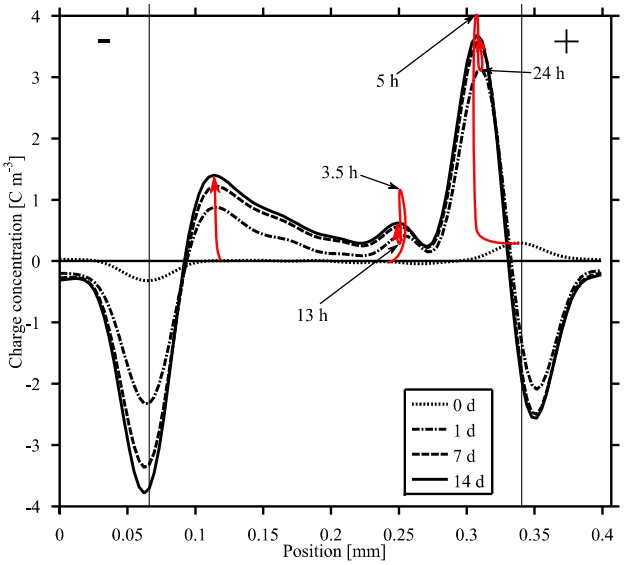

Figure 19. Charge distribution in sample with low water content, at 40 °C and 4% RH. The applied electric field was 36 kV mm^{-1}. The red arrows show the time development of different charge peaks, while the black arrows point to the charge magnitude of a peak at the time given by the accompanying text.

4.3.3.4 **Space charge discharge at 40 °C**

The charge distribution during sample discharge is shown in Figure 20. There did not appear to be any significant positional shifts in the charge peaks. The discharge rate for positive charge in different parts of the sample, shown in Figure 21, is fairly similar in the charge peaks close to the electrodes, but lower in the secondary anode homocharge peak. Similar discharge rates indicate that there are charge carriers with similar mobilities in the anode and cathode peaks; a charge carrier with significantly lower mobility would be expected to discharge at a slower rate, given the same charge concentration. In [120], slower discharge rates have been associated with deeper traps, meaning perhaps that the charge in the secondary peak is in deeper traps than the rest of the charge. Why there would be a narrow area of deep traps 50 µm into the sample from one side is not known, and seems to be unlikely to occur. The charge concentration in the secondary charge peak is lower, however, and the local electric field will therefore also be lower, which is perhaps a more likely reason for the slower discharge rate. Given that the discharge rate for the heterocharge peak at the cathode is similar to the rate of the homocharge at the anode at similar charge concentrations, it seems likely that they consist of charge carriers from the same species. This means that injected charge from the anode will have to have been transported across the sample.

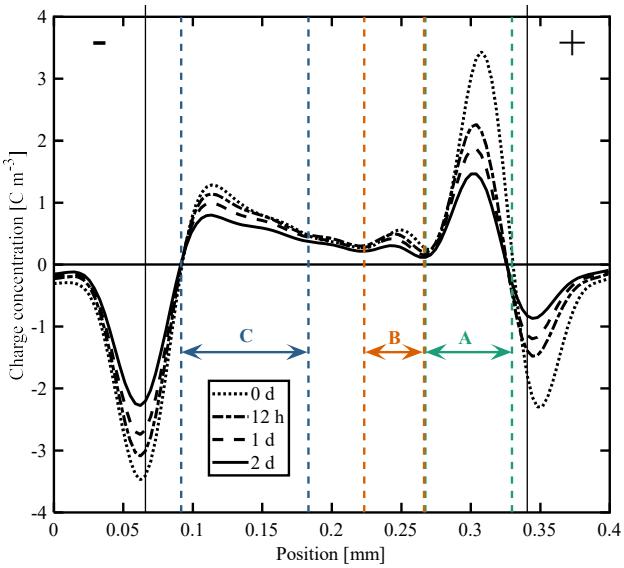

Figure 20. Space charge distribution for discharge of the dry sample at 40 °C. The coloured lines indicate the areas of, from left to right, the cathode peak (C), secondary anode peak (B) and primary anode peak (A).

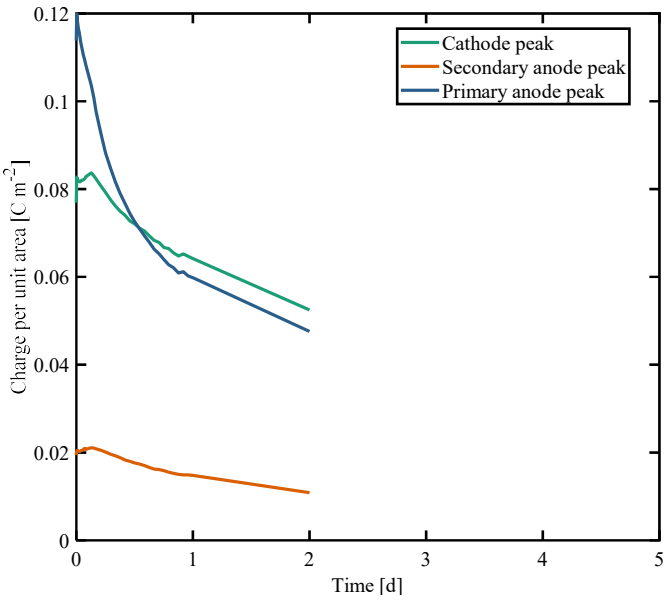

Figure 21. Summed charge per area in the dry sample at 40 °C. The peaks' positional limits correspond to the coloured areas indicated in Figure 20.

4.3.3.5 **Space charge accumulation at 60 °C**

For the dry sample at 60 °C, the charge distribution consisted mainly of homocharge at the anode and heterocharge at the cathode. Some positive charge was also present in the bulk. This is similar to what was found at 40 °C, indicating that space charge accumulation operates by the same mechanisms at both temperatures.

As seen in Figure 22, which shows the charge distribution at 60 °C, charge was initially present in the sample, which likely was residual charge left by the calibration procedure. The charge at the anode and in the bulk increased rapidly for about 10 hours, after which it stabilised and remained at near constant levels for the rest of the measurement period. Charge magnitude at the anode was 2.1 C m^{-3}, significantly lower than the anode homocharge in the dry sample at 40 °C. Charge magnitude in the bulk was approximately the same for both temperatures. At the cathode, the heterocharge increased to a maximum of 1.4 C m^{-3} after around 2.5 hours, and then decreased rapidly. A stable level was reached after about 1 day. At its maximum the charge was at about the same magnitude as the heterocharge in the dry sample at 40 °C after 14 days. A marked difference between the distribution at 60 °C and the lower temperatures is therefore that the accumulated charge apparently reaches equilibrium within the test period.

The accumulation rate of anode homocharge at 60 °C was higher than at 40 °C, and likely a result of a higher injection rate at 60 °C than at 40 °C. The lower equilibrium peak magnitude at 60 °C may be an effect of higher charge mobility at 60 °C. More charge is injected, leading to a rapid initial increase in charge concentration, but more charge is also transported away, leading to a lower amount of accumulated equilibrium charge. Both increases in injection and increases in mobility with temperature is in accordance with the literature [121,122].

At the cathode, the initial accumulation of heterocharge occurred more rapidly at 60 °C than at 40 °C. The amount of positive charge at the cathode increased until 2.5 hours into the measurement, at which time it started to decrease. One explanation for this is the interaction of two charge carrier species. The accumulation of positive charge carriers at the cathode will increase the local electric field there, increasing the injection of negative charge carriers. An increase in negative charge would decrease the net charge at the cathode, reducing the field. In a situation where injection at the cathode leads to less accumulated negative charge than positive charge, through a lower trapping rate (lower trapping cross-section or higher amount of detrapping) or a low injection rate, the net charge would be positive, but be affected by injection dynamics at the cathode, similarly as was hypothesised to occur at the anode at 40 °C. This would also explain why the cathode peak magnitude is reduced over time at 60 °C. In practice this is a process with two time constants: a lower one for the positive charge and a higher one for the negative charge. Charge extraction and recombination would also affect the charge peak dynamics.

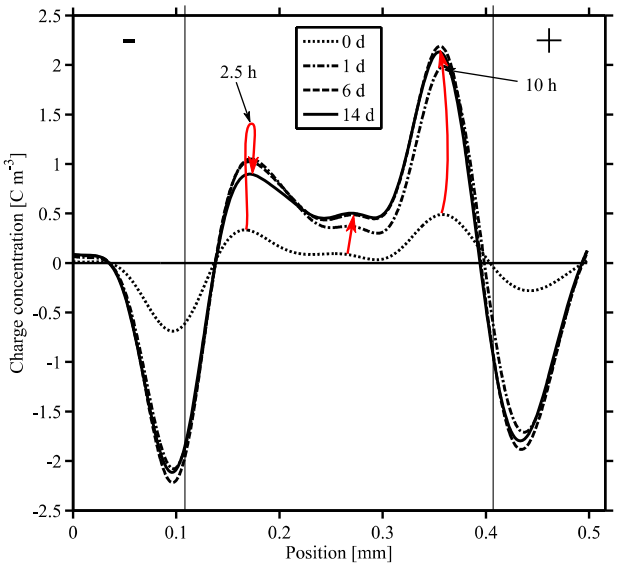

Figure 22. Charge distribution in sample with low water content, at 60 °C and < 1% RH. The applied electric field was 32 kV mm^{-1}. The red arrows show the time development of different charge peaks, while the black arrows point to the charge magnitude of a peak at the time given by the accompanying text.

4.3.3.6 **Space charge discharge at 60 °C**

At 60 °C, mainly positive charge was present in the sample. The effect of charge concentration on discharge rate can be seen in Figure 23, where charge at the anode discharged at a higher rate due to the initial higher magnitude. This is most easily shown by plotting charge magnitude per unit area at 60 °C, as shown in Figure 24. As was the case at 40 °C, this was probably a consequence of the higher local electric field at the anode due to a higher local density of charge. After around 1 day, the charge concentration at the electrodes and in the bulk at 60 °C was roughly of the same magnitude, and the discharge throughout the sample occurred at more or less the same rate. A initially high discharge rate followed by a slower discharge, similar to what occurred during the first day of discharge at 60 °C, was suggested to be due to different trap levels discharging at different time scales in [123].

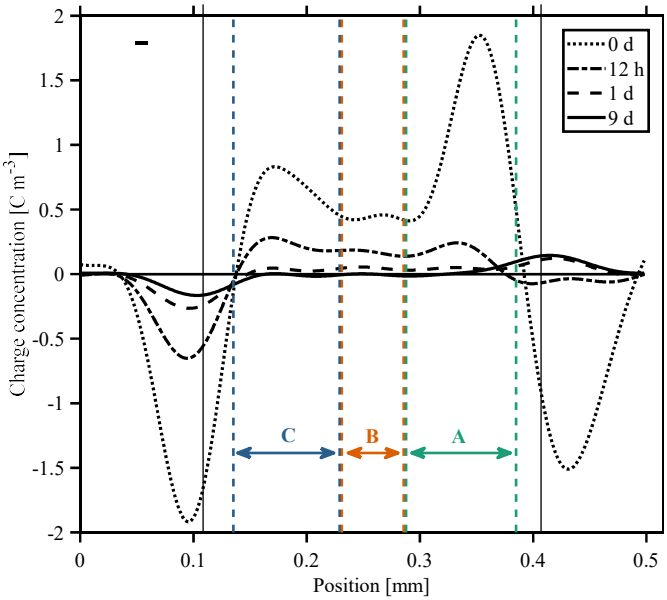

Figure 23. Space charge distribution for discharge in dry conditions at 60 °C. The coloured lines indicate the areas of, from left to right, the cathode peak (C), bulk peak (B) and anode peak (A).

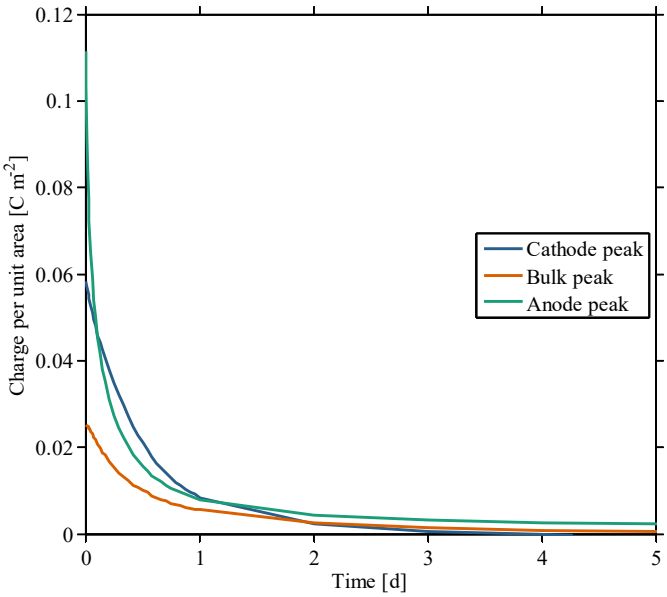

Figure 24. Charge per area in different peaks in dry conditions at 60 °C. The peaks' positional limits correspond to the coloured areas indicated in Figure 23.

4.3.3.7 **Space charge accumulation 80 °C**

The charge distribution at dry conditions at 80 °C is shown in Figure 25. As for the samples at 60 °C, there was initially some charge present, likely remnant charge after calibration. As voltage was applied, homocharge accumulated at the anode, while heterocharge accumulated at the cathode. This is similar to what occurred at 40 and 60 °C, suggesting similar mechanisms being dominant.

The cathode heterocharge increased until 20 minutes into the measurement, and then decreased, before finally disappearing after about 6 days. This is similar to the heterocharge at 60 °C, which also decreased after some time. The heterocharge started to decrease at an earlier time at 80 °C, showing that increasing the temperature affects the processes responsible for the dynamic changes. This may be related to increases in injection and mobility, which both have previously been found to increase with temperature [121,122]. The cathode heterocharge was roughly of the same maximum magnitude as for 40 and 60 °C, but the maximum occurred at an earlier time. This is likely due to the mobility of positive charge increasing with temperature, and also due to the injection of negative charge increasing with temperature. Hypothetically, a higher mobility would lead to increased cross-sample transport of positive charge, as well as a lower residence time of positive charge in traps. Without any negative charge, this would result in the charge reaching a maximum magnitude where all traps were filled at an earlier time than at the lower temperatures. The charge peak would remain at the maximum as long as the applied voltage is constant. When injection of negative charge is also included, the result would be negative charge accumulating in the traps near the cathode, which would reduce the cathode heterocharge peak magnitude. This is consistent with the measured results. At the end of the measurement period, the negative charge peak at the cathode reduced in magnitude and broadened, and appeared to move into the sample. It is uncertain whether this is negative charge accumulating, a result of the mirror charge peak reflecting the changes in the rest of the charge distribution, or a combination. A previous study suggested that the lowering and broadening of a charge peak indicated injection of charge [124].

The homocharge at the anode increased to a maximum at 5 hours. After this, the charge magnitude fell to a value of about 70% of the maximum within the first day. The rate of decrease then fell, the peak reaching its final value of approximately 60% of the maximum at the end of the 14-day charging period. The charge peak widened during the measurement, reaching the centre of the sample after 7 days. Comparing the charge distribution to what was found at 40 and 60 °C, it shows quite similar behaviour though the time scale is shorter at 80 °C. The anode homocharge magnitude was lower at 80 °C than at 40 and 60 °C. The difference between the anode peaks at the lower temperatures and 80 °C may be due to, for example, injected positive charge being rapidly transported away from the anode, or higher amounts of negative charge leading to a more rapid net

charge decrease. This is the same process as has been suggested at the lower temperatures, and occurs on a shorter time scale due to higher charge mobility.

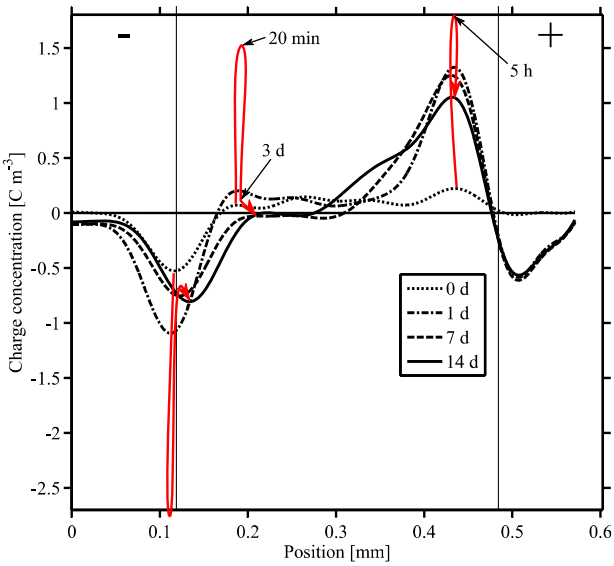

Figure 25. Charge distribution in sample with low water content, at 80 °C and < 1% RH. The applied electric field was 33 kV mm^{-1}. The red arrows show the time development of different charge peaks, while the black arrows point to the charge magnitude of a peak at the time given by the accompanying text.

4.3.3.8 **Space charge discharge at 80 °C**

At the end of the charging measurement period at 80 °C, the charge peaks of significant magnitude were homocharge peaks at both electrodes. As mentioned before, the cathode homocharge peak may be real charge combined with the mirror peak or just the mirror peak alone, although the former seems more likely [124]. The charge distribution during discharge is shown in Figure 26. The rate of discharge, shown in Figure 27, was initially high, and was reduced as the charge density lowered. This is similar to what occurred during discharge at 60 °C, and is likely connected to different trap levels being present in the insulation [123].

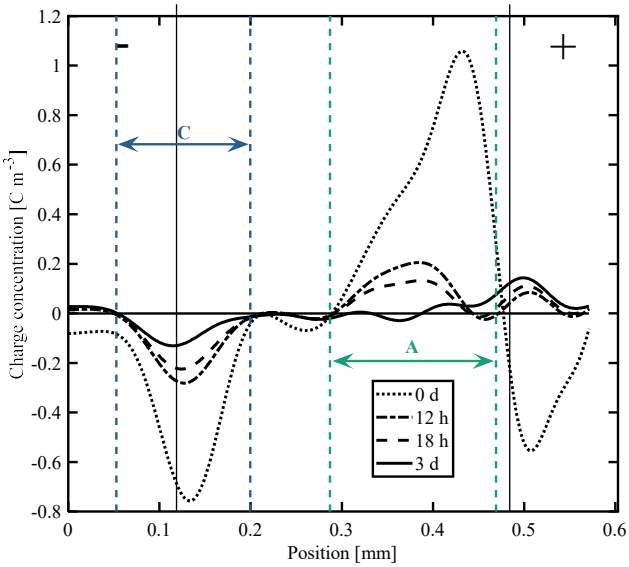

Figure 26. Space charge distribution for discharge in dry conditions at 80 °C. The coloured lines indicate the areas of, from left to right, the cathode peak (C) and anode peak (A).

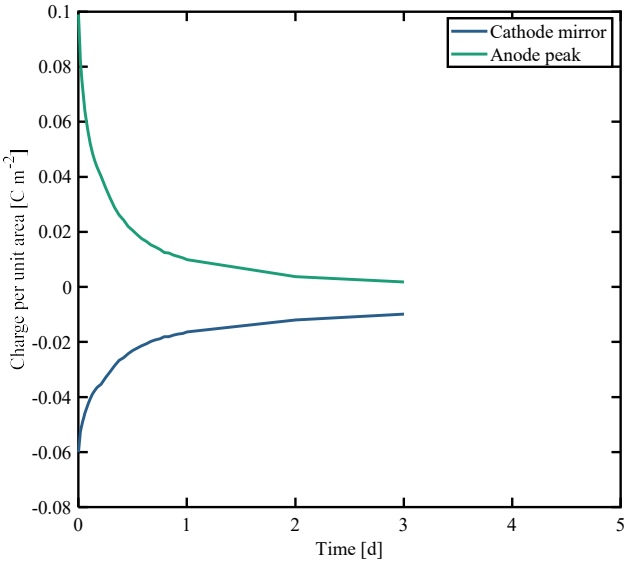

Figure 27. Charge per area in different peaks in dry conditions at 80 °C. The peaks' positional limits correspond to the coloured areas indicated in Figure 26.

4.3.4 Measurement results at high water content

4.3.4.1 Space charge accumulation at 20 °C 85% RH

At 85% RH, the charge distribution, shown in Figure 28, was initially dominated by homocharge, showing that accumulated injected charge remained dominant at 20 °C when the water content was increased. The homocharge peaks were relatively wide, with the negative and positive peaks covering a third of the sample thickness each, respectively near the cathode and anode, and the tail of the negative peak covering the centre third of the sample. The net negative charge at the centre of the sample reached a maximum after about 2 days, and then began to decrease. A possible origin for this is that the charge in this area was at first dominated by injected charge from the cathode. Over time, charge from either the bulk or from the anode accumulated in the same area, which after 5 days resulted in the net charge in the centre becoming positive. The now positive charge peak increased for the rest of the measurement. Some apparent negative charge between the positive centre charge and the anode homocharge can also be seen, appearing after about 4 days. The amount of charge is very low, however, and close to the sensitivity limit of the measurement system. If it is assumed to be real charge, the resulting semi-symmetrical heterocharge does match the pattern for bulk-generated charge such as dissociated ions quite well. The cathode homocharge reached a maximum after about 5 days and then started to decrease. The homocharge peaks at the end of the measurement were slightly narrower in this case than for the dry sample, and the amplitude was about 75% of what was observed at dry conditions.

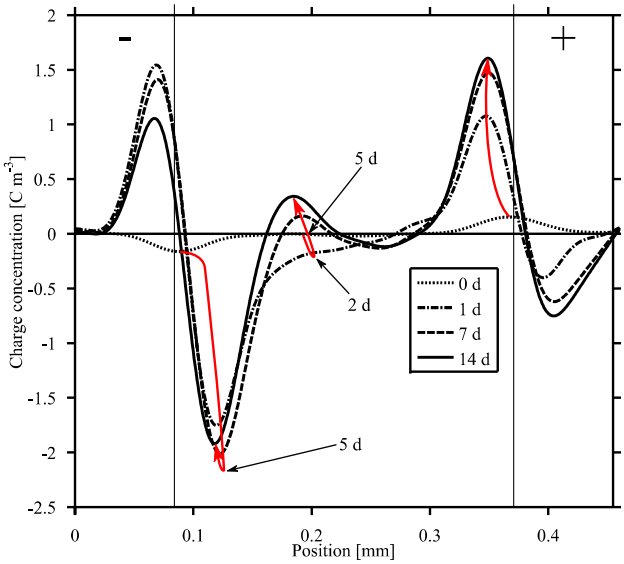

Figure 28. Charge distribution in sample with high water content, at 20 °C and 85% RH. The applied electric field was 31 kV mm^{-1}. The red arrows show the time development of different charge peaks, while the black arrows point to the charge magnitude of a peak at the time given by the accompanying text.

4.3.4.2 **Space charge discharge at 20 °C 85% RH**

Unfortunately, the recording of the discharge measurements stopped after 34 minutes. During this time, it showed the same discharge tendencies as the dry samples (see Section 4.3.3.2 and 4.3.3.4), e.g. more rapid discharge in areas with higher charge concentrations, indicating that similar mechanisms dominate.

4.3.4.3 **Space charge accumulation in a supersaturated sample at 20 °C**

Figure 29 shows the charge distribution in the supersaturated sample. Homocharge accumulated at the anode, again showing that injected charge was dominant there. At the cathode, heterocharge accumulated, meaning that the high amount of water in the sample changed the net charge there to positive. This is different from what was observed in the dry and the 85% RH samples at 20 °C (see Section 4.3.3.1 and 4.3.4.1). More positive charge was also present in the bulk. Both homocharge and heterocharge accumulation appeared to start immediately after the DC voltage was applied. During the first 4 hours of measurement, symmetrical heterocharge accumulated at both the cathode and anode, although the charge concentrations were low. The anode heterocharge peak stopped growing after 4 hours and started to decrease in magnitude. After 5 days, the anode heterocharge was gone, and only positive charge was present in the sample. The cathode heterocharge reached a peak after about 4 days, and then started to decrease. After 9 days, it seemed to have reached a steady state. The anode homocharge increased for the whole measurement period. The difference in charge accumulation between 85% RH and supersaturation is due to higher amount of water; either the water increased the mobility of injected positive charge or there was an amplification of bulk generation. If the latter is the case, the bulk-generated negative charge will have to have significantly different properties from the positive charge in the supersaturated sample, as the anode heterocharge disappeared early while the cathode heterocharge grew significantly during the measurement. It is of course possible that the observed pattern is a result of both processes occurring simultaneously: the symmetrical heterocharge is due to bulk generation while the large cathode heterocharge and anode homocharge peaks are due to hole injection and transport enhancement.

The fact that heterocharge started accumulating very quickly after voltage application means that either there was bulk-generated charge accumulating at the cathode, or that the injected charge at the anode had high enough mobility so that significant amounts of charge have been transported across the sample and accumulated during the time before the first measurement 5 minutes after voltage application. A crossing time of 5 minutes corresponds to a mobility of $3 \cdot 10^{-14}$ $m^2 V^{-1} s^{-1}$, which is within the range of mobilities found in the literature [115,125,126]. Bulk-generated charge has also been found to occur in polyethylene insulation [12,13,44,46,75,76,80], however.

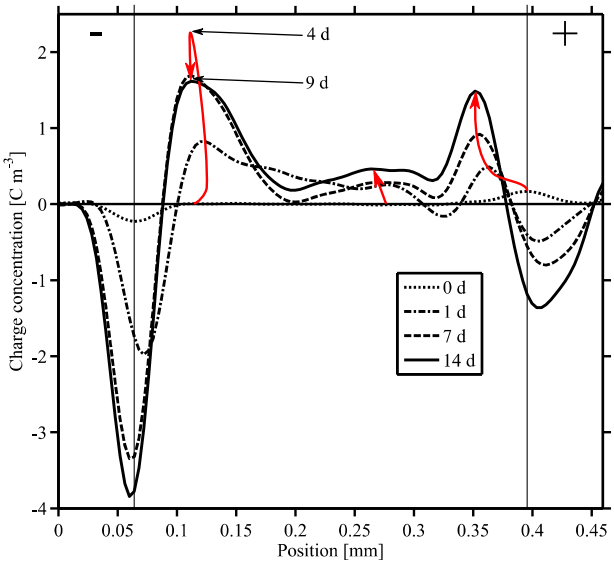

Figure 29. Charge distribution in supersaturated sample, at 20 °C and 75% RH. The applied electric field was 35 kV mm^{-1}. The red arrows show the time development of different charge peaks, while the black arrows point to the charge magnitude of a peak at the time given by the accompanying text.

4.3.4.4 **Space charge discharge in a supersaturated sample at 20 °C**

The charge distribution of the supersaturated sample during discharge at 20 °C is shown in Figure 30. The charge per unit area in the coloured areas shown in the figure is plotted in Figure 31. Comparing the homocharge and heterocharge peaks shows that the heterocharge discharges at a slower rate than the homocharge peak, even though the charge peaks are of a similar magnitude. This was different than for the dry samples, where charge peaks of similar magnitudes discharged at similar rates.

For charge peaks of equal magnitude containing the same charge carrier species, located in areas with similar trap distributions, discharge rates would be expected to be equal. Even though differences in trap distributions seems to be the suggested origin of the difference in discharge rates in [123], a difference in trap distribution between the anode and cathode is here unlikely, as both electrodes were made of the same semiconducting acrylate ethylene copolymer, and were subjected to the same conditioning procedure. If, on the other, hand two different charge carrier species are assumed to be responsible for the respective positive charge peaks at the anode and cathode, a difference in mobility between the carrier species could explain the difference in discharge rates. In that case, the cathode heterocharge, consisting of carriers being retained longer, would be of a species having a lower effective mobility than the carrier species at the anode. The presence of lower mobility heterocharge would indicate bulk charge generation, such as ionic dissociation, appearing in addition to the previously established injected charge.

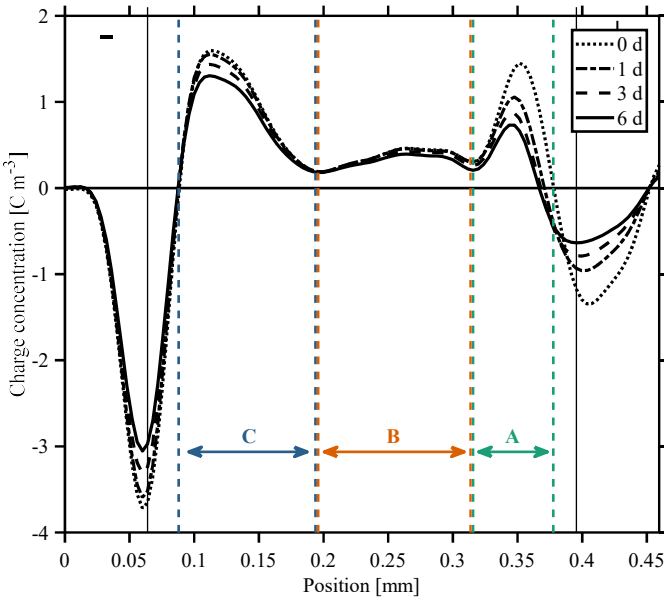

Figure 30. Space charge distribution for discharge of the supersaturated sample at 20 °C. The coloured lines indicate the areas of, from left to right, the cathode peak (C), bulk peak (B) and anode peak (A).

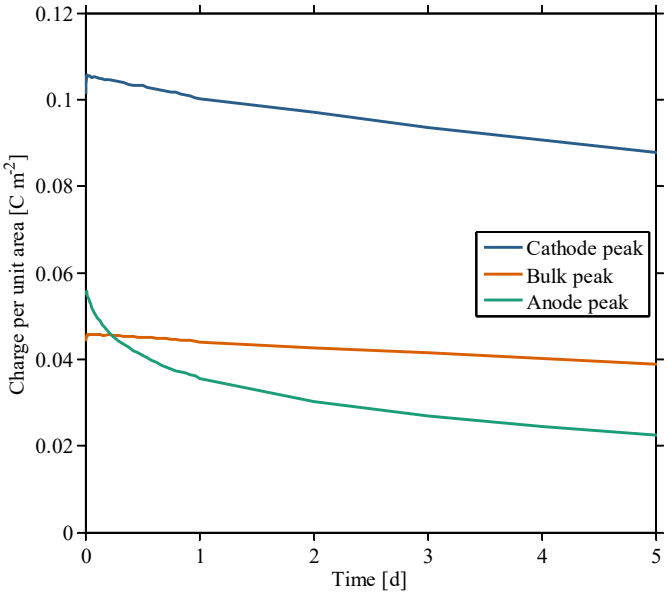

Figure 31. Charge per area in different peaks in the supersaturated sample at 20 °C. The peaks' positional limits correspond to the coloured areas indicated in Figure 30.

4.3.4.5 **Space charge accumulation at 40 °C 85% RH**

At 40 °C, as shown in Figure 32, the positive charge accumulating in the whole sample resembles what was measured for dry conditions (see Section 4.3.3.3). This implies that there are similar mechanisms responsible for the space charge at 40 °C 85% RH as there was for the dry sample at 40 °C. There are also similarities with the supersaturated sample at 20 °C. The charge accumulation rates at 40 °C 85% RH were similar to what was found for the dry sample, but the maximum charge magnitudes at high water content were lower. As was found in the dry sample, the homocharge at the anode in Figure 32 increased rapidly in the period after voltage application. It then decreased for about a day, before starting to increase once more. This occurred at an earlier time for the wet sample than for the dry sample; the anode peak started to decrease after 3.5 hours, 1.5 hours before the corresponding decrease in the dry sample anode peak. Assuming similar mechanisms being dominant in the dry sample and the 85% RH sample at 40 °C, the earlier shifts in accumulation rates at 85% RH would likely be the result of a higher mobility of charge carriers.

A rapid shift in the location of the cathode heterocharge peak can be observed after 7 days of measurement. This was due to a communications problem between the oscilloscope and the computer software that recorded the data, resulting in the oscilloscope resetting some settings to default. Among these were the sampling frequency. This was partly compensated for in post-processing of the data, but while the charge magnitude after compensation remained roughly the same as before, the placement of the peaks shifted slightly, and was most noticeable for the cathode heterocharge.

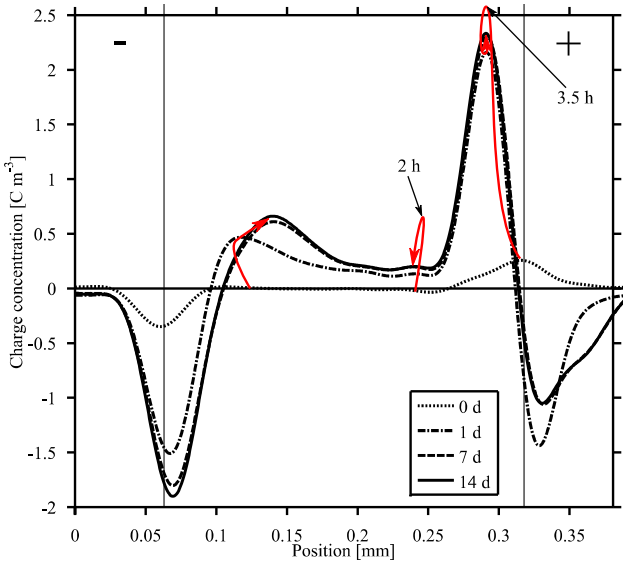

Figure 32. Charge distribution in sample with high water content, at 40 °C and 85% RH. The applied electric field was 39 kV mm^{-1}. The red arrows show the time development of different charge peaks, while the black arrows point to the charge magnitude of a peak at the time given by the accompanying text.

4.3.4.6 **Space charge discharge at 40 °C 85% RH**

At 40 °C, there is no significant difference between the discharge of the wet sample, shown in Figure 33 and Figure 34, and the discharge of the dry sample. The discharge rates in the dry sample were slightly higher than in the wet sample, likely due to the initial charge magnitude being higher in the dry sample. The discharge rates indicate that the mobilities of the carriers during discharge are similar.

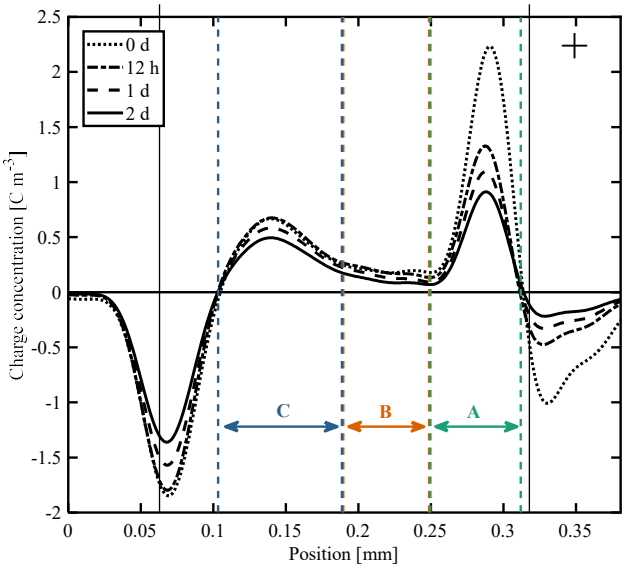

Figure 33. Space charge distribution for discharge of the sample with high water content, at 40 °C and 85% RH. The coloured lines indicate the areas of, from left to right, the cathode peak (C), bulk peak (B) and anode peak (A).

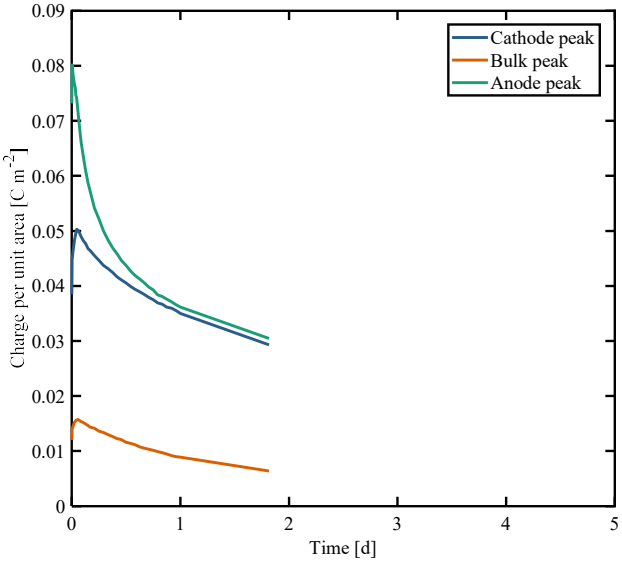

Figure 34. Charge per area in different peaks in the sample at 40 °C and 85% RH. The peaks' positional limits correspond to the coloured areas indicated in Figure 32.

4.3.4.7 **Space charge accumulation at 60 °C 85% RH**

Some space charge was initially present, possibly residual charge from the calibration procedure similar as in the dry sample. Heterocharge accumulated at the cathode and homocharge at the anode, as shown in Figure 35. Positive charge accumulated in the bulk. The similarity between the charge distribution in this sample and the dry sample at 60 °C, both samples at 40 °C, and the supersaturated sample at 20 °C suggest that similar mechanisms are also dominant with absorbed water present at 60 °C. The charge accumulated at a faster rate than what was found for the dry sample, which, as in Section 4.3.3.3, can be due to an increase either in the charge injection rate or in the charge trapping rate near the electrode. Similar to what was found at 40 °C, changes in the charge accumulation rate at 60 °C 85% RH occurred earlier than in the dry sample at 60 °C, indicating that absorbed water increased the charge carrier mobility. From about 1–2 days into the test, the cathode mirror charge peak started to move into the sample. This may be an indication of negative charge building up close to the cathode, especially as at the end of the measurement period there seems to be a positive mirror charge peak appearing in the cathode. The movement of the cathode peak into the sample is similar to what was found in dry conditions at 80 °C (see Section 4.3.3.7), where positive charge was found to accumulate more rapidly than negative charge so that measurable negative charge appeared much later than measurable positive charge. It is probable that the effects of the slower negative charge injection and accumulation is therefore the origin of the cathode heterocharge peak movement [124].

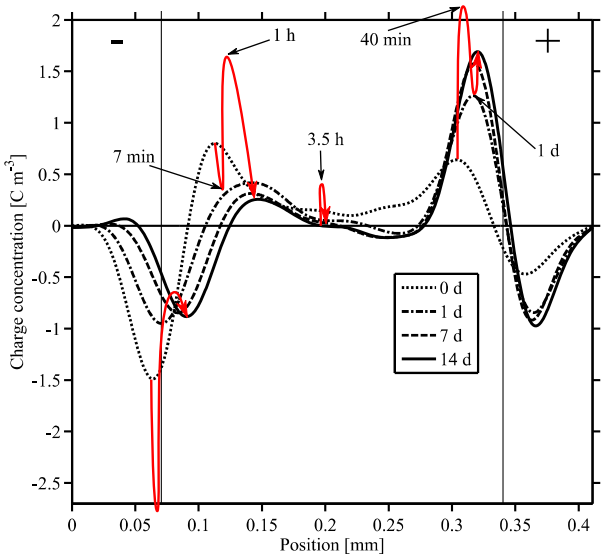

Figure 35. Charge distribution in sample with high water content, at 60 °C and 85% RH. The applied electric field was 37 kV mm^{-1}. The red arrows show the time development of different charge peaks, while the black arrows point to the charge magnitude of a peak at the time given by the accompanying text.

4.3.4.8 **Space charge discharge at 60 °C 85% RH**

As the sample at 60 °C 85% RH suffered a breakdown at the end of the charging period, no discharge measurements could be performed.

4.3.4.9 **Space charge accumulation at 80 °C 85% RH**

As shown in Figure 36, there was initially heterocharge at both electrodes, which was probably remnant charge from the calibration procedure. This was replaced by homocharge during the first half hour after voltage application.

At the cathode, the homocharge accumulated very close to the electrode. As was the case for cathode heterocharge at lower temperatures, the magnitude of charge initially increased, then decreased, and then increased again. It is not unlikely that the changes in charge accumulation rate is due to the interaction between two different charge carrier species, one of them being the injected electrons. However, as for anode homocharge in dry conditions at 40 °C, this could also be a result of the local electric field affecting the injection and transport of electrons. Similar to the dry sample at 80 °C, the changes in charge peak accumulation rate occurred earlier in the wet sample at 80 °C than at the lower temperatures. A noticeable difference from what was found for wet samples at the lower temperatures was that the cathode heterocharge at 80 °C never increased much above the initial values and disappeared soon after measurement start. Given that the initial accumulated heterocharge was most likely an effect of the calibration procedure (remnant charge after the negative polarity calibration, i.e. injected homocharge), this means that there was only homocharge accumulation at the cathode at 80 °C 85% RH. This can be due to a reduction of positive charge, through suppressed transport or reduced bulk generation, or through an increase in the accumulation of negative charge due to increased injection or trapping. Looking at the high build-up of positive charge between the middle of the sample and the anode, it is possible that the lack of cathode heterocharge is related to increased trapping of positive charge carriers. In addition, the size of the cathode homocharge peak indicates an increased presence of negative carriers, although this may also be a result of the mirror charge peak at the cathode being large due to the large positive charge accumulation in the bulk. The peak does move into the sample during the first day of measurement, however, which, much as for 60 °C and 85% RH, is an indication of charge injection.

At the anode, homocharge built up to a peak around 0.1 mm from the electrode, and increased in magnitude for the entire measurement period. Towards the end of the measurement period, the peak of the positive charge concentration shifted slightly towards the cathode. Some heterocharge also appeared at the anode towards the end of the test. The amount of anode homocharge was significantly higher in the wet than in the dry sample. It is possible that this is related to the water concentration, which at 80 °C 85% RH is much higher than at 85% RH at the lower temperatures. In that case, there is apparently a critical limit of either water concentration alone or water concentration combined with temperature over which water enhances charge accumulation significantly.

The positive charge concentration appeared to move towards the cathode during the measurement period, which contrasts with the charge at lower temperatures which remained mostly stationary. This may be the main concentration of trapped charge moving, or it may be an effect of negative charge accumulating near the anode. There is some evidence of this in the broadening of the mirror charge peak at the anode, which is similar to what occurred at the cathode at 60 °C 85% RH.

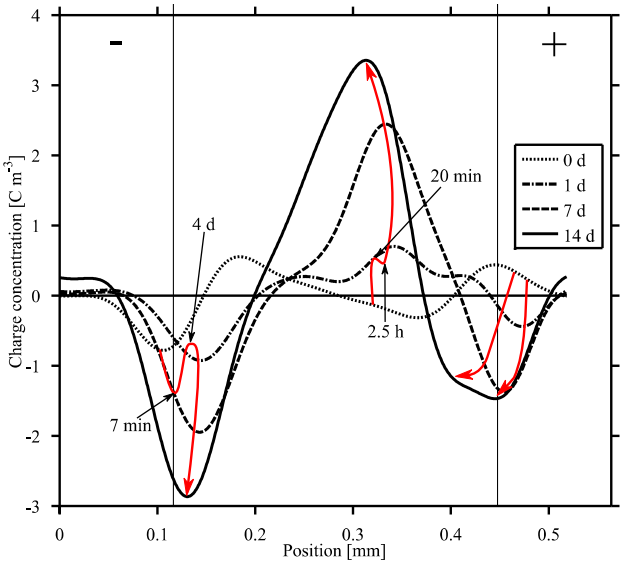

Figure 36. Charge distribution in sample with high water content, at 80 °C and 85% RH. The applied electric field was 32 kV mm^{-1}. The red arrows show the time development of different charge peaks, while the black arrows point to the charge magnitude of a peak at the time given by the accompanying text.

4.3.4.10 **Space charge discharge at 80 °C 85% RH**

Discharge of the wet sample at 80 °C, shown in Figure 37 and Figure 38, was initially at a higher discharge rate than in the dry sample. However, when comparing the discharge rates of charge concentration peaks of similar magnitudes in the wet and dry samples, the discharge rates were similar, indicating that the charge carriers moving in the samples are the same for dry and wet samples.

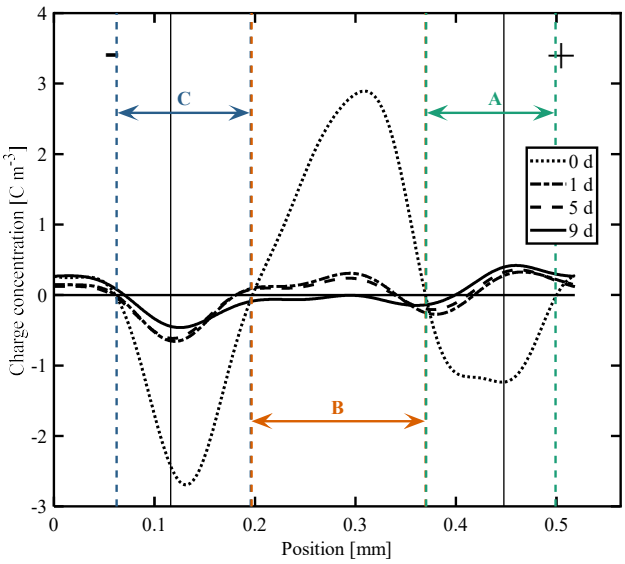

Figure 37. Space charge distribution for discharge of the sample with high water content, at 80 °C and 85% RH. The coloured lines indicate the areas of, from left to right, the cathode peak (C), bulk peak (B) and anode peak (A).

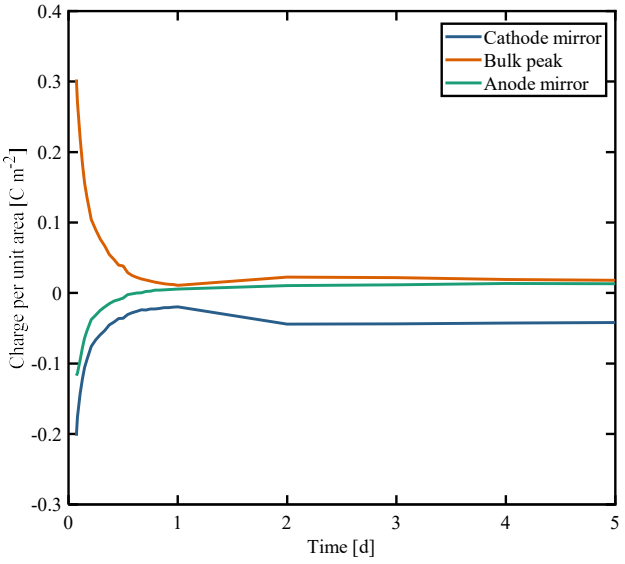

Figure 38. Charge per area in different peaks in the sample at 80 °C and 85% RH. The peaks' positional limits correspond to the coloured areas indicated in Figure 37.

4.3.5 **Summarised results**

Table 14 lists the most important aspects of the charge distributions at the various temperatures and relative humidities.

At 20 °C, the absorption of water facilitated positive charge accumulation in the bulk and near the cathode. The magnitude of accumulated homocharge at the anode was reduced by the absorbed water. Supersaturation increased the accumulation of positive charge in the bulk and at the cathode, changing the net charge at the cathode to heterocharge.

Increasing the temperature to 40 °C increased the magnitude of the accumulated charge, while further increases in temperature reduced the magnitude. Higher temperatures increased the rates of charge accumulation, dissipation and discharge.

Absorption of water at 40 °C reduced the overall magnitude of accumulated charge. At 60 °C water absorption reduced the anode homocharge peak, while the magnitude of cathode heterocharge remained similar to the magnitude in the dry sample. The charge accumulation rate was equal in both dry and humid samples at 40 °C, while at 60 °C absorbed water increased the accumulation rates. At 80 °C, the absorption of water led to accumulation of significant amounts of positive charge in the bulk.

Table 14: Space charge results summary

T [°C]	RH [%]	Cathode	Bulk	Anode	Comments
20	25	Homocharge	None	Homocharge	Uniform charge increase
	85	Homocharge	Positive charge closer to cathode	Homocharge	Cathode heterocharge appeared after 5 days
	100	Heterocharge	Positive charge	Homocharge	
40	4	Heterocharge	Positive charge	Homocharge	Charge increased for 5 hours, decreased for 20 hours, then increased again
	85	Heterocharge	Positive charge	Homocharge	Charge increased for 3 hours, then decreased slightly for the rest of the measurement
60	0	Heterocharge	Positive charge	Homocharge	Charge increased for 10 hours, then remained constant
	85	Heterocharge	Positive charge, disappears over time	Homocharge	Charge increased for 10 minutes. Cathode heterocharge then decreased for the rest of the measurement. Anode homocharge decreased, reaching a constant level after 1 day
80	0	Heterocharge, disappears	Positive charge, disappears over time	Homocharge	Cathode heterocharge increased rapidly up to 20 minutes, then decreased. Bulk charge increased for 2 hours, then disappeared gradually. Anode homocharge increased for first 5 hours, then fell. It also spread into the sample
	85	Homocharge	Positive charge	Homocharge, possibly heterocharge at end of measurement	Bulk positive charge peak present, which combined with anode homocharge after about 1 day. Positive charge in bulk dominating charge distribution, increasing for the entire measurement period. Indications of negative charge accumulation at near electrodes

4.3.6 **Discussion**

This section contains the discussion of the space charge measurements collectively. First, the space charge results with regards to the effect of temperature are discussed and the likely sources of charge carriers in dry samples assessed. Next, two hypotheses that exist in the literature for the effect of water on space charge, water-induced shallow traps and generation of dissociated ions (see Section 2.4.1), are used to evaluate the measured results with high water content. Then, a macroscopic model [64] connecting the influence the semiconductor electrodes can have on trap distribution is presented, and its effect on the conductivity and space charge accumulation is compared to the measurement results. Finally, given that indications of temperature- or water content-dependent charge carrier mobilities were found in the measurement results, the discharge patterns of the different samples are analysed and the apparent mobilities calculated.

4.3.6.1 **Effect of increased temperature on dry samples**

Increasing the temperature seemed to increase the charge injection rate at the anode, which has also been found in the literature [121]. This is likely the reason for the overall increase in charge magnitude from 20 to 40 °C and may also explain why positive charge dominates at 40 °C and higher. Positive charge injection has also been found to be dominant for XLPE with semiconducting electrodes in [41]. Changes in the charge peaks occurred at shorter intervals at higher temperatures, which can be linked either to an increase in mobility or an increase in negative charge in the sample. The decrease in overall magnitude from 40 to 60 °C and 80 °C is the opposite of what would be expected from the increase in injection. However, increased mobility of charge carriers with temperature [121,122,127] could result in reduced charge magnitude even with an increased injection rate, for example through a shorter charge residence time or through an increased transport of negative charge to the anode, leading to negative charge accumulation that would reduce the net positive charge in the measurement.

While the changes in homocharge due to increased temperature can generally be explained by injected charge and temperature dependence of the mobility, the accumulation of heterocharge, which is present at 40 °C and higher, is often connected to bulk-generated charge. The question of the origin of the heterocharge in the dry samples will be evaluated in Section 4.3.6.1.1. In addition, some observations regarding mobility for injected charge resulting in heterocharge accumulation will be presented in Section 4.3.6.1.2.

4.3.6.1.1 **Bulk-generated heterocharge**

Although the most referenced sources of bulk-generated charge in XLPE are cross-linking by-products and additives such as antioxidants [43-46], degassing has previously been found to remove most of the effect of the by-products as described in [44,46,77,79]. Given that all of the samples used in the space charge measurements were degassed, it is likely that cross-linking by-products and antioxidants likely have a very limited effect on the charge accumulation in the samples.

Another potential source of bulk-generated charge is absorbed water, through the dissociation of water molecules. The samples described as dry still retain around 0.005 kg m^{-3} of water, as they are in equilibrium with the air inside the climate chamber during the measurements. The water content of the air inside the chamber is determined by the relative humidity in the lab, which was measured to be on average 25% at 25 °C during the measurements. However, ionic dissociation results in both positive and negative ions being generated, leading to the expectation of heterocharge at both electrodes. Instead, only cathode heterocharge is observed. This would occur if, for instance, the negative ions were more mobile and could be more easily removed from the insulation. In general, for water the negative hydroxide ions and their water complexes

are less mobile than the positive protons and their complexes, although this is in liquid systems. There is no expected affinity between either of the ions and the non-polar polyethylene chains. The similarity of the ions means that the asymmetry in having positive heterocharge with no negative heterocharge could be due to a dissimilar mobility, as the less mobile species would accumulate as space charge more easily: if the mobility was similar, a symmetrical charge distribution would be expected. Given that at 40 °C and higher the charge distribution is asymmetric, there is either a significant difference in mobility, e.g. through effective ion size or the traps that can respectively affect either of the positive or negative ions, or there could be an interaction effect between several charge carrier species, such as accumulation of injected positive charge masking the accumulation of negative ions at the anode.

The main argument against water ions affecting space charge accumulation is the number of dissociated ions required. Disregarding the potential injected negative charge in the dry sample at 40 °C, the positive charge concentration at the cathode requires on average 1 ion per 20,000 water molecules, calculated using a water content of 0.005 kg m^{-3}. In contrast to this, when using self-dissociation rates in liquid water at 40 °C , only 1 ion per 300,000,000 water molecules is obtained [113]. The number of ions will increase with increasing temperature, but even at 80 °C, the amount is still only 1 ion per 100,000,000 water molecules. As discussed in Section 4.2.4.2.2, the amount of self-dissociation in a XLPE sample could likely be expected to be orders of magnitude lower, due to the lower density of water and non-polar structure of XLPE. Looking at the diffusion properties, it is likely that water molecules do not form clusters in XLPE but move as individual molecules, leading to an even lower number of ions per water molecule. This means that self-dissociation alone can probably not provide enough ions to obtain the charge concentrations found in the heterocharge peaks, even if the amount required to remove the effect of injected negative charge is disregarded. In addition, it is likely that negative charge injection at the cathode also takes place at 40 °C. It could be possible that a strongly field-dependent dissociation process could be able to explain the difference in measured charge concentration and estimated dissociated ion concentrations, however, as field-dependent dissociation has not been included in the estimates. The effect of this process, assumed to be independent of conduction in completely dry XLPE, would still strongly depend on the concentration of water, as the amount of water molecules available determines the amount of ions generated. Unless the electric field dependence for the dry conduction mechanism and for the ionic dissociation mechanism are very similar, the electric field dependence would therefore be expected to change from a dry sample to a sample with high water content. The water dissociation mechanism would become more dominant as water content increases. However, in the current measurements presented in Figure 9, the electric field dependence of the conduction current seems to be mostly unaffected by the water content of the samples.

4.3.6.1.2 **Injected charge as heterocharge**

For injected charge to lead to heterocharge accumulation at the cathode, there would need to be an increased amount of trap-states near the cathode or an extraction barrier for positive carriers. For a single carrier type, a symmetrical trap distribution when comparing the electrodes is likely, given that the anode and cathode both consist of the same semiconducting polymer. The positive charge mobility required to accumulate heterocharge at the cathode can be estimated by looking at when positive net charge appears in the measurement. At 40 °C, this occurs after approximately 1 hour. If the heterocharge is assumed to exclusively consist of injected charge that has been transported across the sample, an average crossing time of 1 hour combined with the sample thickness and applied electric field from Table 13 would correspond to a mobility of $2 \cdot 10^{-15}$ $m^2 V^{-1} s^{-1}$. This is not an unreasonable value, as the literature reports mobilities in the range from $5 \cdot 10^{-17}$ to 10^{-13} $m^2 V^{-1} s^{-1}$ [115,125,126].

The calculated mobility above uses an average crossing time based on the appearance of measurable ($Q > 0.2$ C m^{-3}) space charge. However, in order to obtain a measurable charge concentration after 1 hour, the actual accumulation would have to have started before this time. The actual charge mobility will in that case have to be higher than the mobility found from the measurable charge peak at the cathode. Using the upper limit of the reported mobilities in the literature, 10^{-13} $m^2 V^{-1} s^{-1}$ yields a crossing time of 1 minute, which is short enough to enable the cathode charge accumulation in the measured results. Using the lower mobility limit, $5 \cdot 10^{-17}$ $m^2 V^{-1} s^{-1}$ results in a crossing time of around 2 days, however, which would be too long to result in the observed charge accumulation.

At higher temperatures, the cathode heterocharge appears at an earlier time, which means a shorter crossing time and a correspondingly higher charge mobility. This is in accordance with the literature, where higher temperatures have been found to increase charge mobility [121,122,127].

4.3.6.1.3 **Homocharge peak dynamics**

Looking at the homocharge peak at the anode, the charge concentration reaches a maximum after around 5 hours at 40 °C, and then decreases until 1 day after measurement start. A similar change in the accumulation rate also occurred at 80 °C. The change from increasing to decreasing the accumulated charge has at least three possible explanations, even when limiting the carrier type to injected holes and electrons. In addition, if more charge carrier types such as dissociated ions are included, the interaction of these with the injected carriers may also give rise to dynamically changing charge peaks.

The first possibility is that the accumulated positive charge in the sample reduces the electric field at the anode, thereby limiting injection. While charge is transported away from the anode, it will still contribute to the reduction in the local electric field at the anode. The balance between injection and transport of charge will change over time,

leading to an oscillation of the charge peak. While this would explain the change in accumulation rate, it does not explain why there is an additional positive homocharge peak appearing near the centre of the sample at 40 °C.

The second possibility is that the reduction is due to transported negative charge. In that case, negative charge moves across the sample and is trapped near the anode. This will reduce the measured net positive charge, which will therefore be lower than the real positive charge present there. A transported negative charge build-up does not necessarily have the same localisation or concentration as a peak consisting of injected positive charge. While injected charge will start filling up traps closest to the electrode, charge moving through the bulk will fill up traps on the way. If the trap density increases with increasing proximity to the electrodes, this will result in increased charge concentration closer to the centre of the sample. The observed reduction in the positive charge concentration that occurs near the centre of the sample at 40 °C could be an effect of this, as the net charge in the region would be reduced. The timing of the reduction also corresponds well with this hypothesis, as it occurs at about 3.5 hours into the measurement, while the anode peak reduction starts at 5 hours into the measurement – transported negative charge would start affecting the positive net charge closer to the cathode earlier and affect charge peaks closer to the anode later.

The third effect that can lead to reduction of charge is recombination. As the accumulated charge in the measurements at 40 °C and higher is mostly positive, recombination will most likely be between injected free electrons and trapped holes. For the anode peak to be affected, the electrons would have to move an average distance corresponding to three quarters of the sample thickness in the 5-minute time from when the high voltage is switched on to when a measurable effect on the charge is observed. This would require an electron mobility of $2 \cdot 10^{-14}$ m^2 V^{-1} s^{-1}, calculated using the average applied electric field at 40 °C in the measurements, which is within the range of mobilities reported in the literature [115,125,126]. Recombination or superposition would also occur between injected electrons and transported holes in the region near the cathode. There is no way to distinguish between recombination and superposition from the PEA measurements, as both phenomena would result in a reduction of net charge. To tell the difference between these phenomena, other effects such as electroluminescence due to recombination would have to be observed, requiring different measurement techniques. Electroluminescence measurements has previously been used to show recombination occurring in LDPE [53], but have not been considered for this work.

It is also possible that field-dependent injection, recombination and co-located trapping occur simultaneously in the samples. Charge accumulation rates would be affected by all three mechanisms simultaneously and given the complex behaviour of charge accumulation in the samples this seems to be quite likely to occur.

4.3.6.2 **Effect of increased water content**

The effects of water absorption on the space charge distributions will be discussed based on the hypotheses that were presented in Section 2.4.

It is important to note that in the measurements at higher humidity the effect of the higher water content will likely occur in addition to the effects in dry samples; the observed effects that are present in dry samples are not necessarily expected to disappear when increasing the water content. The following discussion will use the measurements of the dry samples as a basis. For dry samples at 20 °C, bipolar injection was the dominant source of charge carriers. Increasing the temperature to 40 °C increased charge injection, and either increased positive charge mobility at 40 °C leading to positive heterocharge, or increased the antioxidant-related bulk charge generation leading to positive heterocharge. Further increasing the temperature to 60 °C increased the injection and mobility of positive charge, while increasing the temperature to 80 °C increased positive charge mobility and negative charge injection.

4.3.6.2.1 **Increased mobility of electronic carriers due to introduction of shallow traps**

As shown in Section 4.3.4.1, the presence of water at 20 °C resulted in a lower amount of homocharge combined with increased injection. This is consistent with water molecules increasing shallow trap density, which in turn increases charge transport. Increased injection would lead to an increased accumulation of charge, but the increased transport of charge into the bulk limits the amplitude of the charge peak. Due to the similarity between the charge peaks of the 85% RH sample and the peaks in the dry sample, it seems likely that the deep trap distribution in the samples is unaffected by water absorption. The small amount of positive charge near the sample centre can be explained by injected charge having moved through the middle of the sample. The slow accumulation of positive charge will be a result of the time it takes for the charge carriers to move there from the anode. There is no corresponding negative charge having crossed the other way, even though negative charge injection still appears to be high. This means that either the mobility of negative carriers is not affected as much by the presence of water, or that water creates a difference in the deep trapping of positive and negative charge that was not evident in the dry sample. The latter seems unlikely, however, as an increased density of deep traps would decrease the mobility of charge, and likely increase the accumulation of homocharge. In addition, water has only been found to give rise to increased shallow trapping for electronic charge carriers [10,67,69].

Supersaturation at 20 °C resulted in a continuation of the changes introduced by the absorption of water at 85% RH. Due to the more rapid accumulation of positive heterocharge, when compared to the 85% RH sample, this means that positive charge

mobility is further increased by the increased water content. Negative charge mobility may also have been affected, as some negative heterocharge can be observed appearing and subsequently disappearing during the first day of measurement. Compared to the 85% RH sample, positive charge is much more dominant in the supersaturated sample. The amount of positive charge is also higher. Since only injected charge is considered in this discussion, this means that either positive charge injection will have to have increased significantly more than negative charge injection, or that the shallow traps from absorbed water are deep enough to enhance the accumulation of positive charge.

At 40 °C, the lower amount of accumulated charge can be explained by the increased mobility due to absorbed water leading to a change in the balance between trapping and detrapping. The increased number of intermediate states (shallow traps) means that carriers can move out of deeper traps more easily, lowering the net residence time.

The similarities of the charge distributions of the dry sample and the sample at 85% RH indicate that the similar charge transport mechanisms remain dominant at 40 °C when increasing the humidity. This is consistent with water affecting shallow traps, increasing the effective mobility of injected charge, while affecting deeper traps much less [10]. Indeed, the interaction with deeper traps, which is central to where charge is trapped, does not seem to be affected very much, given that the shape of the charge distributions at 40 °C seems to be unaffected by water absorption. Indications of an increase of the mobility of negative charge carriers can be seen at 40 °C, as the reversal of the anode homocharge peak occurs earlier, at 85% RH, than in dry conditions, as can be seen when comparing Figure 20 and Figure 32. This reversal would occur when injected negative carriers crossing the sample arrive and accumulate in the same volume as the positive anode peak. Carriers with a higher mobility would be expected to arrive earlier. However, as for dry samples, the reversal could also occur due to decreased injection from a homocharge affected decrease of the local electric field at the anode.

At 60 °C, the measured results seem to support the assumption that absorbed water leads to increased mobility. This is based on an increased heterocharge accumulation rate at the cathode, which would occur if positive charge could be transported across the sample more easily. This is consistent with what was observed at higher humidities for both 20 and 40 °C. Negative charge mobility also seems to be affected by humidity, as negative charge appears near the anode towards the end of the measurement period. For the dry sample, no negative net charge was present. In addition, the homocharge accumulation rate at the anode peak reversed earlier for the sample at 85% RH, than for the dry sample. An earlier reversal compared to the dry sample at 40 °C also occurred at 40 °C 85 % RH. This is consistent with negative charge arriving at an earlier time, due to a higher charge mobility in the sample at higher humidity. The cathode heterocharge also started accumulating again after reversal, at an increased rate. This requires that there either be

an increase in negative charge injection, an increase in positive charge extraction or that there is significant recombination.

At 80 °C and 85% RH, the charge accumulation process initially seems to be similar to lower temperatures, as cathode heterocharge accumulated for the first minutes of the measurement. The accumulation of positive charge does not appear to be as dominant in the first few hours compared to the lower temperatures, as homocharge also was present at the cathode, reminiscent of what occurred at 20 °C 85% RH. This is different from 40 °C and 60 °C, where only heterocharge was observed. There was also some heterocharge at the anode, which, while being the opposite of what was observed at lower temperatures, would indicate an increased transport of negative charge due to increased mobility. The lack of positive charge dominance for the first minutes could have been explained by increased mobility; the mobility of positive charge has increased to such a degree that detrapping occurs with the same frequency as trapping, leading to no significant build-up of positive charge. However, following the first minutes of measurement there is a massive build-up of positive charge. The charge peak is located further into the bulk than the anode homocharge peaks were at the lower temperatures. Another difference between 80 °C and the lower temperatures is negative charge peaks located close to both electrodes. The massive build-up of positive charge in the centre of the sample does not appear to be consistent with the hypothesis of higher mobility; there is no reason for highly mobile charge to be contained in the centre of the sample. Trapping of charge in the bulk is also different from the observed charge distributions at lower temperatures and in the dry sample at 80 °C, which were dominated by charge trapped near the electrodes.

4.3.6.2.2 **Ionic dissociation of water molecules**

For ionic dissociation, the appearance of cathode heterocharge at 20 °C 85% RH is the first indication. As equal amounts of positive and negative charge are created by dissociation, some symmetry in heterocharge could be expected, although this depends on the properties of the ions. The asymmetry in heterocharge that was found in the measurements, particularly at higher temperatures, seems to slightly contradict this, but could possibly be explained with trapping or other differences in mobility. As there was significantly more positive heterocharge than negative charge, positive ions would appear to be more easily trapped. There is not any apparent reason to expect a barrier to extraction for either of these ionic groups through the polymer electrodes, as the semiconducting polymer has comparable water permeability to that of the XLPE (see Appendix B). The transport through the semiconducting electrodes will likely be lower than through the insulation, as there is no electric field affecting the ions there, but this should affect both the positive and the negative ions more-or-less equally. If the difference in heterocharge is due to a difference in the trap distribution for positive and negative ions, there is asymmetry in trap depths and densities between positive and negative ions. Based on the

charge distributions, there would have to be considerably more positive ion trapping than negative ion trapping.

In the supersaturated sample, the charge distribution when assuming bulk generation of ionic carriers again would indicate a difference in trapping. The increased amount of charge compared to the 85% RH sample would occur due to more dissociable water being present in the sample. As negative ions are seemingly absent, this indicates a lower likelihood of trapping, similar to the sample at 85% RH. Negative ions are removed from the area close to the anode faster than they accumulate. In addition, the higher trapping rate of positive ions means that higher amounts of negative charge will need to accumulate to be detectable; small amounts of trapped negative ions will be masked by higher concentrations of trapped positive ions.

At 40 °C, the heterocharge at the cathode in the 85% RH sample is what would be expected for ionic dissociation. However, the main difference between the charge distributions of the dry sample and the sample at 85% RH is a lower charge concentration magnitude and more rapid processes, making it reasonable to assume that similar mechanisms are dominant for both samples. This means that, when ionic dissociation is assumed for the 85% RH samples, the decrease in charge magnitude at 85% RH compared to the dry sample would be the opposite of what would expected, given the increase of dissociable molecules when water is absorbed. Increased temperature has been found to increase the likelihood of detrapping [128], which would lead to a reduction of accumulated charge, but this would also occur in the dry sample. Another possibility is that the increased amount of dissociated ions leads to increased accumulation of negative charge, which would reduce the net positive charge in comparison to the dry sample. This could be feasible at the anode, as negative ions would migrate there due to the applied electric field. However, in order to also reduce the cathode heterocharge, negative ions would also need to accumulate there, which is more unlikely, as negative ions affected by the electric field would migrate away from the cathode.

At 60 °C, there was again similarities between the charge distributions of the dry sample and the sample at 85% RH, indicating that similar mechanisms are in play. The lower amount of accumulated charge again would be opposite to expectations if ionic dissociation is assumed, due to the higher availability of dissociable molecules in the 85% RH sample. In addition, the earlier reversal of the accumulation rate of positive charge at the cathode in the sample at 85% RH does not seem plausible if ionic dissociation is the only effect of increasing humidity. In order for this to occur, negative ions would have to accumulate near the cathode, which is unlikely, as negative ions would be transported away from, not towards, the cathode.

Ionic dissociation would, similar to the lower temperatures, be expected to lead to heterocharge superimposed on the charge distribution of the dry sample at 80 °C. The

measured results show no significant heterocharge at the start of the measurements; rather, there is only positive charge located in the bulk. The amount of charge is higher in the sample at 85% RH, which is different from what occurred at lower temperatures. Charge of a single polarity being dominant does not correspond well to the ionic dissociation hypothesis, given that, as above, a charge distribution including both polarities would have been expected. However, differences in trapping, where positive charge is more easily trapped than negative charge, might explain why mainly positive charge accumulated.

4.3.6.3 **Macroscopic model: increased conductivity in near-interface regions**

Defects and impurities in the sample will affect the trap distribution and conductivity, as explained in Chapter 2. As impurities have been found to migrate from semiconducting polymer electrodes during production, it is likely that the concentration of impurities increases with proximity to the electrodes [72], leading to increased conductivity in those regions [63]. To test whether this effect can explain the space charge distributions found in Section 4.3, a macroscopic model, originally described in [64] and summarised in Section 2.3, was used.

Equation (2.15) was implemented into a finite element model. The bulk conductivity was based on Poole-Frenkel conduction, using Equation (4.3), with parameters corresponding to a water content of 0.012 kg m^{-3} from Table 9, and a temperature of 20 °C. The initial conductivity distribution used in the model is shown in Figure 39, in which the parameters are $x_\sigma = 3$ µm and $m_\sigma = 10$. As can be seen, this increases the conductivity near the electrodes up to a maximum of 3 times the bulk conductivity. Converting the normalised position in Figure 39 by using the thickness of the real sample at 20 °C in dry conditions, this corresponds to the increased conductivity reaching a depth of around 60 µm from the electrodes before bulk values are reached. The applicability of the model was investigated using two parametric sweeps, one each for the m_σ and x_σ parameters, with sweep values as shown in Table 15.

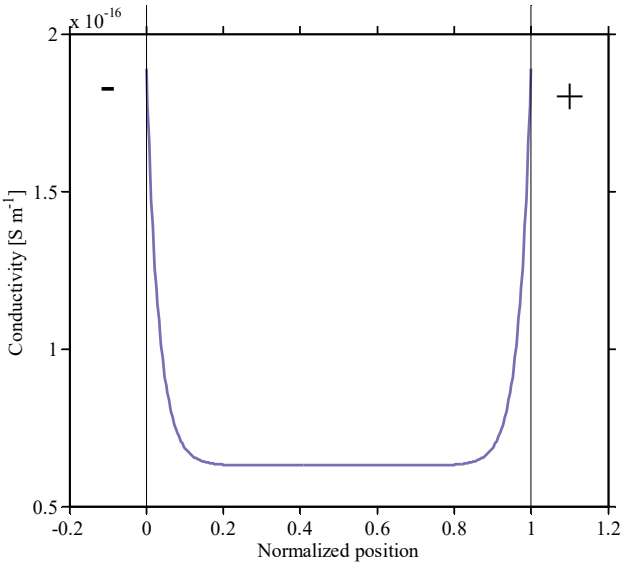

Figure 39. Conductivity gradient used in the modelling, with $x_\sigma = 3$ µm, $m_\sigma = 10$, and T = 20 °C.

Table 15: Parameter values used in the modelling

Parameter	Sweep values				
m_σ [-]	3	10	30	100	1000
x_σ [µm]	10	20	40		80

4.3.6.3.1 **Distance factor and enhancement factor fitting at 20 °C**

Figure 40 shows the measured results for the dry sample at 20 °C after 14 days at 10 kV, along with some results from the parameter sweep. As can be seen, the modelling results in a symmetrical peak structure similar to the measurement result. Using peak placement and magnitude as a starting point, the parameter set yielding results most similar to the measurements was with $m_\sigma = 30$ and $x_\sigma = 40$ µm. This solution yields a steady-state peak magnitude at ±2.5 C m^{-3}, which is very close when compared to 2.1 C m^{-3} at the anode and -2.8 C m^{-3} at the cathode from the measurements. The peak shapes in the model are much wider than what was found in the measurements, however. Narrower peaks are obtained by decreasing x_σ. As can be seen in Figure 40, decreasing x_σ from 40 to 20 µm obtains peaks of similar width to what was observed in the measurements, but with almost double the peak magnitude. The charge in the centre third of the sample is in both cases higher than in the measurements. Further decreasing x_σ to 10 µm leads to no charge being present in the centre third, peak magnitudes that are much too high and narrower and steeper peaks compared to the measurement results. However, the parametric sweep shows that it is likely that an optimised combination of x_σ and m_σ can be found, and that the macroscopic model appears to be sufficient to explain the charge concentrations observed in dry conditions at 20 °C.

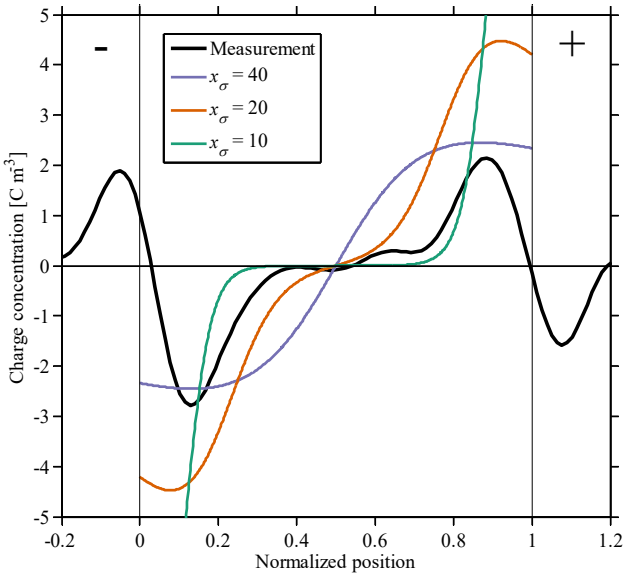

Figure 40. Space charge from finite element calculations with conductivity gradient, x_σ parameter sweep, $m_\sigma = 30$, $T = 20$ °C, along with measurement results for the dry sample at 20 °C.

4.3.6.3.2 **Temperature sweep**

Given that modelling at 20 °C was found to yield satisfactory results, the model was also implemented at 40, 60 and 80 °C. The results are shown in Figure 41, along with the measurement results at the same temperatures. As can be seen, there are discrepancies between the model and the measurements at higher temperatures. The most obvious are the heterocharge peaks in the measurement results at 40 and 60 °C, which are not present in the calculations. In addition, the remnant space charge in the measurements after 14 days at 80 °C was lower than what was present at 20 °C. In the calculations, the steady-state space charge increases when the temperature increases. This is because the absolute differences between the conductivity in the bulk and the conductivity near the electrodes will increase when the temperature increases, due to the temperature dependence of the underlying mechanism, even if the relative differences stay the same. In the measurements after 14 days, the homocharge was higher for 40 °C than at 20 °C. For 60 °C, the homocharge at the anode was of the same magnitude as was measured at 20 °C, while at 80 °C it was lower than all other measured temperatures. The lack of proper description of these phenomena by the model means that the premise of the model, injection combined with a conductivity gradient, while possibly valid at 20 °C, is not sufficient at higher temperatures. Given that the space charge distribution observed when

water is absorbed is similar to the distributions at increased temperatures, the model will also be insufficient to describe the effect of absorbed water.

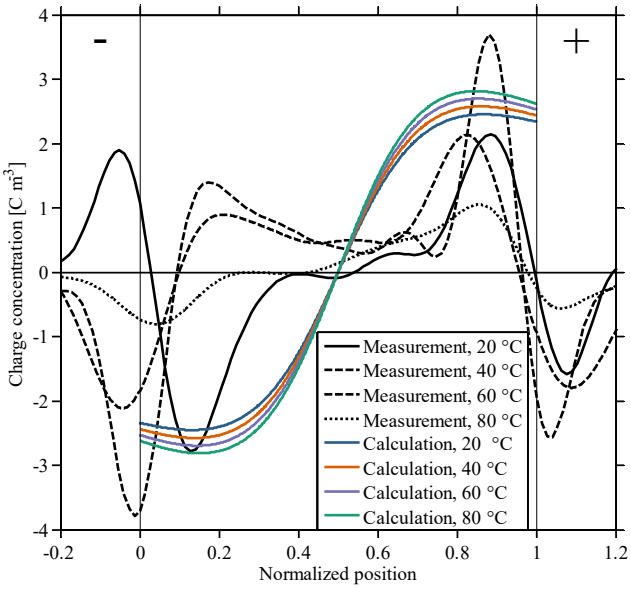

Figure 41. Space charge from finite element calculations with conductivity gradient, T parameter sweep, $m_\sigma = 30$, $x_\sigma = 40$, along with measurement results at 20 – 80 °C.

4.3.6.4 **Improving model fit**

Given the poor fit of the model at higher temperatures, more complex mechanisms must be included to replicate the results found in the space charge measurements. A model of bipolar injection, trapping in a single deep trap level and transport through a sample has been developed in [31] and shown experimentally to work well for space charge and conducted current in [53]. The model has also been expanded to include distributed trap levels as well. Replacing the simplistic macroscopic model using conductivity variance by using the mobility-based charge transport would yield more flexibility to account for phenomena in addition to the trap distribution near the electrodes. Obtaining a long-term defined homocharge, measured at 20 °C in dry conditions, may require using a geometry-dependent trap distribution, where the trap density is higher closer to the electrodes, to replace the conductivity variance. In addition, differentiating the mobility of the two injected charge species would lead to differences in charge transport, e.g. positive charge moving through the sample faster, possibly enabling asymmetric heterocharge accumulation.

4.3.6.5 **Apparent mobility**

Increased mobility of injected charge was found to be a likely explanation for the phenomena observed in the space charge measurements. To check this, charge mobility was estimated from space charge discharge measurements by calculating the apparent mobility, using the procedure from [65] and [66], as described in Section 2.3.2.

4.3.6.5.1 **Low water content**

Using Equation (2.18) on the measured space charge discharge profiles yielded apparent mobilities as shown in Figure 42. The gaps in the 20 °C and 40 °C mobility estimations are due to the calculation returning negative values, which shows that in this case the uncertainty of these kinds of calculations is high. However, the 10^{-15} – 10^{-13} m^2 V^{-1} s^{-1} range of apparent mobilities compares well to the range of mobilities found in the literature [115,125,126]. The apparent mobility increases with temperature, at least up to 60 °C, which is consistent with prior findings [129]. There is also some consistency at 40 °C with the observations on mobility obtained during the space charge accumulation measurements, discussed in Section 4.3.6; the mobility of positive charge was estimated to around $2 \cdot 10^{-15}$ m^2 V^{-1} s^{-1}, slightly lower than the calculated bipolar apparent mobilities here. There is, however, no difference found between the apparent mobility at 60 °C and the apparent mobility at 80 °C. This is different from the indications of increased mobility at 80 °C that was found in the space charge accumulation measurements in Section 4.3.3.7.

The feasibility of the values of the calculated apparent mobilities can also be checked by comparing charge carrier crossing times. The average apparent mobilities in Figure 42 would yield crossing times of around 10 minutes at 40 °C, and 3 minutes at 60 and 80 °C. Comparing this to the times at which heterocharge appears in the measurements (1 hour for 40 °C), this is enough time for the charge to have already crossed. At 60 and 80 °C, the remnant charge from calibration makes it difficult to assess when significant heterocharge would have accumulated, but in both cases the charge increase was higher than the sensitivity of the instrument within the first 5 minutes, which, when taken as the crossing time, is in the expected range based on the estimated crossing time from apparent mobility.

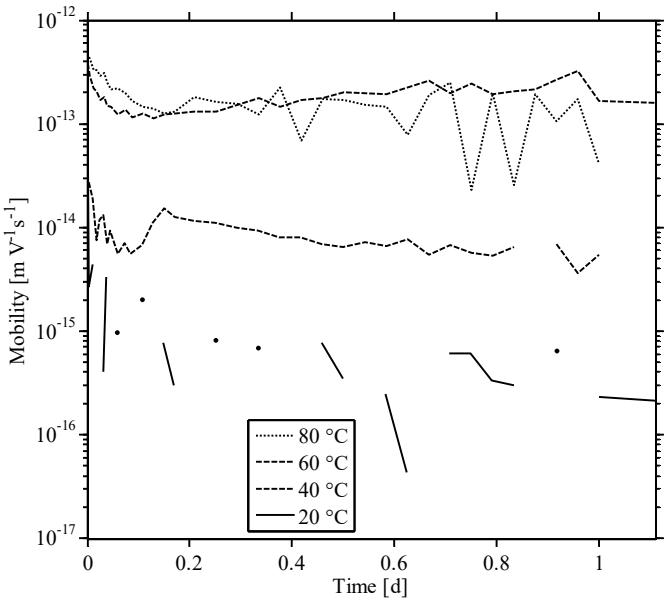

Figure 42. Calculated charge mobility from space charge discharge measurements in dry samples.

Using an average value of the mobility at the different temperatures, an apparent activation energy can be calculated. A plot of the average mobilities against inverse temperature after 1 day of discharge is shown in Figure 43. As can be seen in the figure, an Arrhenius relation using an activation energy of 1.1 eV fits the data well. For comparison, the activation energy for the second driest sample category from the current measurements in Section 4.2.3, calculated using an Arrhenius relation, was between 1.1 and 1.3 eV, which is in the range of the activation energy from the apparent mobility. This is fairly close, especially given that some discrepancy in values would be expected due to the different measurement methods, and the high uncertainty of the current measurement data at the lower temperatures.

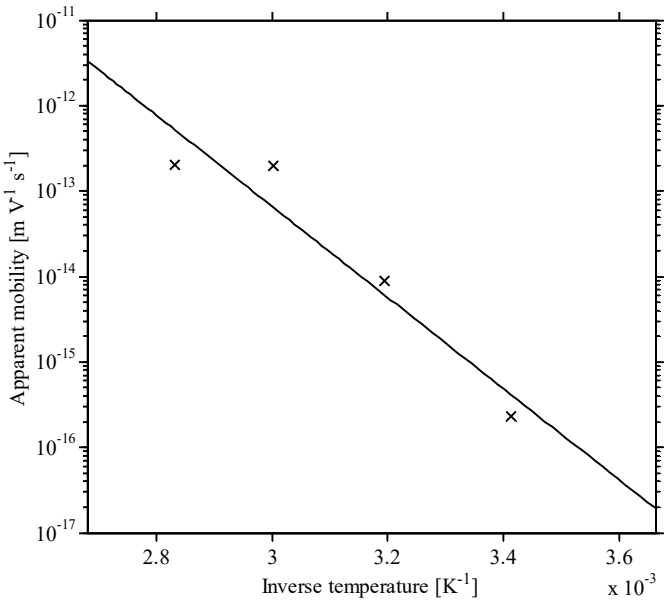

Figure 43. Temperature dependence of average 1-day apparent mobility in dry samples. The straight line is an Arrhenius relation fit with a 1.1 eV activation energy.

4.3.6.5.2 **High water content**

The estimated mobilities for samples with increased water content, calculated using Equation (2.18), are shown in Figure 44. Mobility estimations for the sample at 60 °C and 85% RH were not possible, since no discharge measurements were performed due to sample breakdown during charging. For the sample at 20 °C and 85% RH, only data for the first 30 minutes was available.

At 20 °C, the mobilities of the dry and wet (85% RH) samples are similar. This is also the case at 40 °C. This is different from what would be expected of samples with increased water content, which in a previous study was found to exhibit an increased apparent mobility [10]. The increased apparent mobility there was found for $t < 1000$ s however, which in Figure 44 is seen to be an area with very high uncertainty in the results. The mobility of the supersaturated sample at 20 °C is somewhat higher than the dry sample mobility, appearing to be more in line with the results in [10], but as can be seen the uncertainty is still quite high. It is worth noting that while [10] presented results for 95% RH samples at 185 kV mm^{-1}, an applied field far higher than the applied field in the space charge measurements performed in this work, it also found similar results with regards to increased mobility through measurements of the conducted current at 30 kV mm^{-1}.

Most interesting, though, is that the apparent mobility of the wet sample at 80 °C is lower than the mobility of the dry sample. This is the opposite of what would be expected from a case where water increases the mobility due to an increased number of shallow traps [10]. A lower effective mobility would be expected if there was a higher amount of deep traps, leading to more immobilised charge, or if the remaining charge after voltage application in wet samples contained a significantly higher amount of charge carriers having a lower mobility. For the latter case, ionic carriers generated when water is present in the sample would be expected to have a different, possibly lower, mobility than the injected carriers in dry samples. The appearance of dissociated ionic carriers does not explain why there is mainly positive space charge present – dissociation of water would be expected to result in both negative and positive space charge. For the former case, thermal ageing of the samples would cause deep traps to appear, specifically in the form of carbonyl groups, the time for such ageing to occur in any significant amount is likely much longer than the measurement time, even at the highest temperature [130]. It is possible that the change in behaviour at 80 °C is related to the higher amount of water; at lower temperature samples the water content is 0.02 and 0.04 kg m^{-3} for 20 and 40 °C respectively, significantly lower when compared to 0.17 kg m^{-3} at 80 °C. However, there is no apparent reason to not expect a continuation of the change with water content when the temperature increases – the drastic change in behaviour at 80 °C seems odd without some other mechanism being in effect as well.

The activation energy for the wet samples has not been calculated, as there are measurements of sufficient duration at only two temperatures with the same relative humidity.

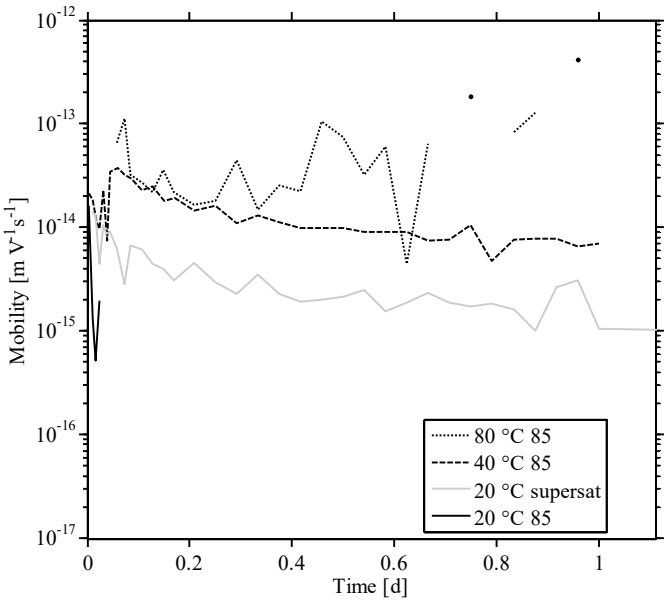

Figure 44. Calculated charge mobility from space charge discharge measurements in wet samples.

4.3.6.6 **Summary**

Analysis of the space charge measurements showed that the origin of space charge in dry samples was probably injected charge – the number of ions required to obtain the measured space charge was much higher than the number of ions likely to be generated through ionic dissociation. Bipolar injection and transport, with increased temperature increasing charge mobility, were also found to be able to explain the observed charge dynamics at higher temperatures. Calculations of apparent mobility also showed increasing mobility for the temperature range 20–60 °C, whereas similar mobilities were found for 60 and 80 °C.

For wet samples, the observed accumulation of charge and dynamics was found to be explainable by bipolar injection and enhanced charge mobility from absorbed water for the temperature range 20–60 °C. Ionic carriers seem to be less likely, given the asymmetric charge distributions and the decrease of charge magnitude in wet compared to dry samples. Apparent mobility calculations were too uncertain at short times to evaluate whether shallow traps were affecting the space charge accumulation. At 80 °C the behaviour of the space charge distribution was markedly different in the wet compared to the dry sample, and also when compared with wet samples at lower temperatures. Calculation of apparent mobility showed that absorbed water apparently reduced the mobility at 80 °C, although the origin of this is not clear.

4.4 Time-dependent currents

4.4.1 Measurement procedure

The measurement conditions of the two sets of time-dependent current measurements are presented in Table 16. The first set examined the charging and discharging currents immediately after voltage application and removal. These measurements were performed at three temperatures and four levels of humidity. Due to low signal-to-noise ratios, parts of the measurements set are not included in the presented results. The second measurements set investigated the long-term effects of applied voltage by measuring the charging and discharging currents for 14 days each. These measurements were performed at 40 °C at relative humidities and applied electric fields similar to what was used in the space charge measurements, enabling comparison between measured space charge and currents.

Table 16: Measurement conditions for current measurement samples

Measurement series	Temperatures [°C]	Relative humidity [%]	Measurement time*	Applied voltage [kV]	Electric field [kV mm^{-1}]
1	40 - 60 - 80	10 - 30 - 60 - 90	1 min	0.6	2
				1.5	5
				3	9
				4.5	14
				6	18
				7.5	23
				9	28
2	40	0 - 85	14 days	15	32

4.4.2 **Short-time measurements**

4.4.2.1 **40 °C**

Charging current

At 40 °C, only the currents at the four highest voltages were above noise level. The charging currents started at a high value, and then quickly decreased to semi-stable values. Figure 45 shows charging currents for two of the voltage levels. As can be seen, the current initially followed a power law decay profile, but diverged after about 4 seconds. This is consistent with the current initially being dominated by polarisation currents, followed by a steady-state conduction current [131]. During the power law decay, the differences between currents at various humidities were not significant. There were significant differences between the following conduction currents, which appear to be dependent on water content. Higher humidity in the sample resulted in higher currents. The conduction current at 90% RH was on average 3 times higher than the current at 10% RH. The conduction currents also appeared to increase slightly with time. The increase was more pronounced at higher water content. This could be an effect of more traps being filled over time, resulting in an increasing amount of semi-mobile charge as the traps are filled. The results show that water at 40 °C mainly affects the slower charge transport processes and has less effect on faster processes dominated by polarisation.

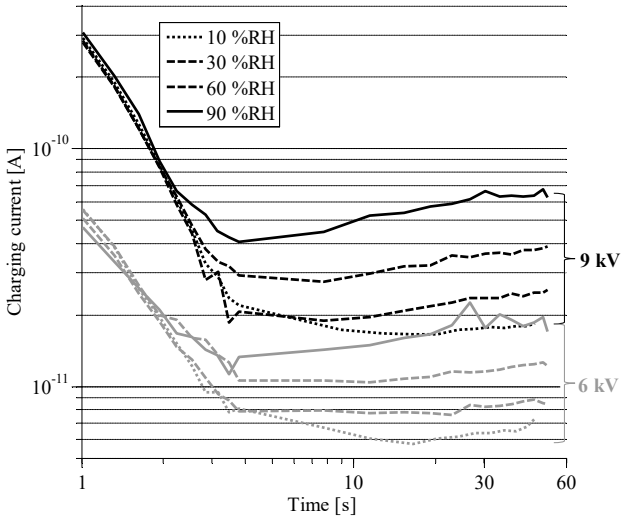

Figure 45. Short-time charging currents at 40 °C.

Discharging current

The log-log plotted discharging currents, shown for two voltage levels in Figure 46, form straight lines for the three lower levels of relative humidity, which correspond to the power law decay profile expected from regular depolarisation currents [59,132]. There appeared to be no difference in current magnitude for the three lowest humidities, which suggests that humidity has little impact on the polarisation processes, which is in accordance with the findings for the charging current. At the highest humidity at 6 and 9 kV, divergence from this trend was observed. The most probable explanation for this was the setup causing interference through the guard electrode; high humidity and possibly even condensed water on the sample surface may lower the resistance between the measuring and guard electrodes.

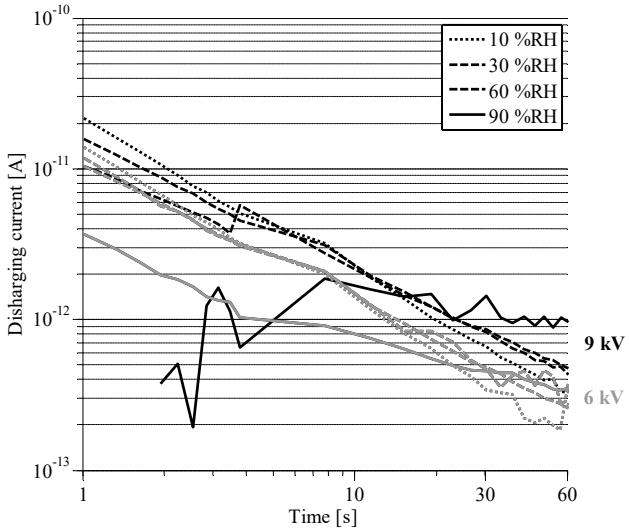

Figure 46. Short-time discharging currents at 40 °C. The currents are inverted.

4.4.2.2 **60 °C**

Charging current

At 60 °C all charging currents except for the lowest voltage level were above noise levels. The currents for three of the voltage levels are shown in Figure 47. At 4.5 kV and lower the current rose for an initial period of around 20 seconds, and then fell. At 6 kV it initially fell, then increased for about 30 seconds and then fell again. This does not conform to the common power law decay to steady-state current. At 7.5 and 9 kV the current initially decreased, and then increased for the rest of the measurement. The initial decrease appeared to follow a power law decay profile. For all voltages, higher humidity resulted in higher currents, on average with a factor of 1.4. The increase in current due to humidity was apparent from the start of the measurements. If the same mechanism is assumed to be active at 40 and 60 °C, the results indicate that the conduction current increases more with temperature than the polarisation current. The peak that appears in the charging currents may be related to space charge effects, and will be discussed further in Section 4.4.2.4.

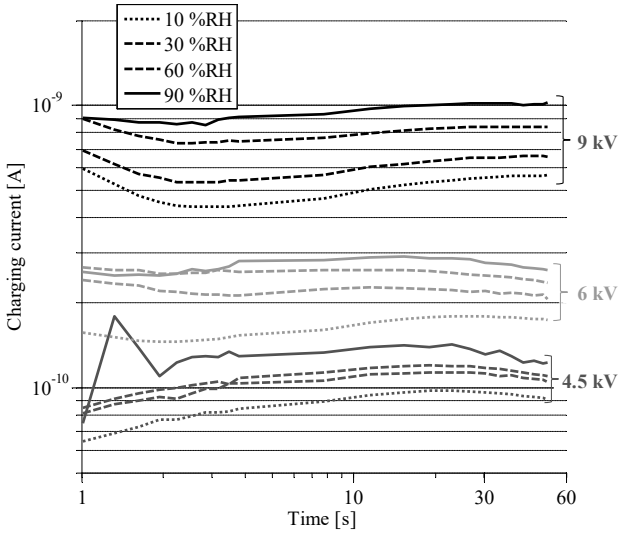

Figure 47. Short-time charging currents at 60 °C.

Discharging current

The discharge currents, shown for three voltage levels in Figure 48, fell for the entire measurement period, following an exponential decay profile. This diverges from the standard power law decay discharge current found at 40 °C. The discharge currents increased with higher humidities, which is also different from 40 °C, where the currents were not affected by humidity. Within the measurement period, the increase in currents due to higher humidity appeared to be for the most part constant, as the differences between currents at the same voltage levels but different humidities did not change appreciably over time. It is possible that this is related to increased charge mobility due to shallow traps from absorbed water, as was indicated in Section 4.3.6.2.

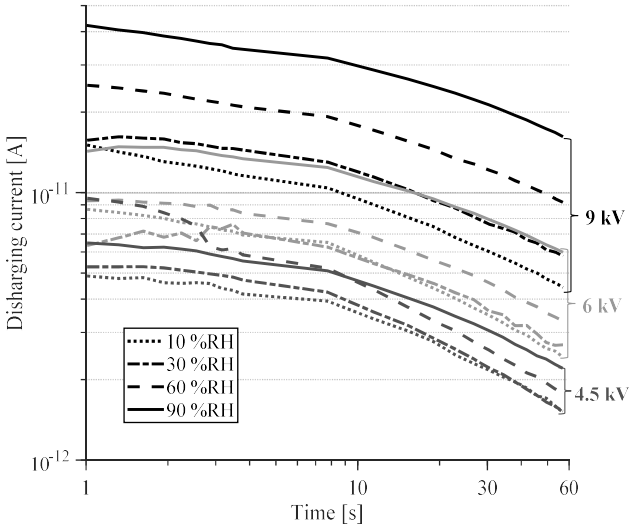

Figure 48. Short-time discharging currents at 60 °C. The currents are inverted.

4.4.2.3 **80 °C**

Charging current

At 80 °C, all voltage levels yielded charging currents above noise levels. The charging current at 80 °C, shown for three voltage levels in Figure 49, decreased from an initial high value at the start of each measurement. At 4.5 kV applied voltage and lower, this continued for the entire charging period. At higher voltages, the charging current started to increase after some time at higher humidities. At 6 kV, the current at the highest humidity level started increasing after about 40 seconds; at 7.5 kV, the charging current started increasing after about 30 seconds at the second highest and after 25 seconds at the highest humidity level; at 9 kV, the currents corresponding to the three highest humidity levels started increasing at 35, 20 and 15 seconds, with shorter times corresponding to higher humidities. While it is likely that this would eventually lead to a peak in the current, as will be discussed in section 4.4.2.4, the measurements are too short to conclude on this. In general, higher water content yielded higher charging currents.

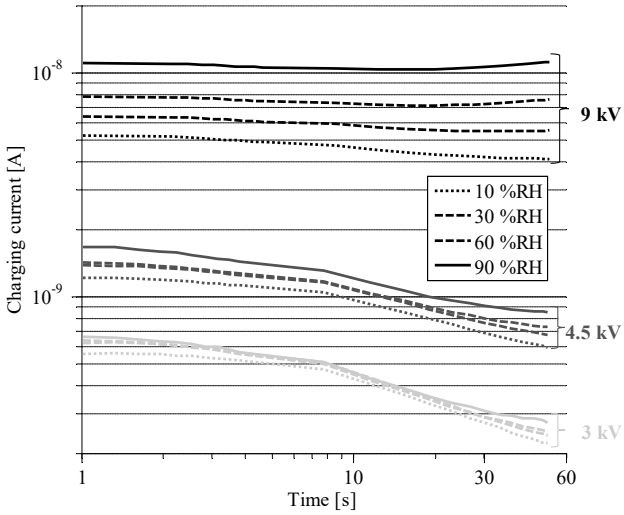

Figure 49. Short-time charging currents at 80 °C.

Discharging current

The discharge currents, shown in Figure 50, fell from the start of the measurement, at a rate which increased with time. This was similar to what occurred at 60 °C. An apparent difference was that while currents at higher humidity at 80 °C initially had higher magnitude than currents at the same voltage and temperature and at lower humidity, the differences were reduced with time. At 60 °C, the difference in currents at different levels of humidity did not appear to change with time.

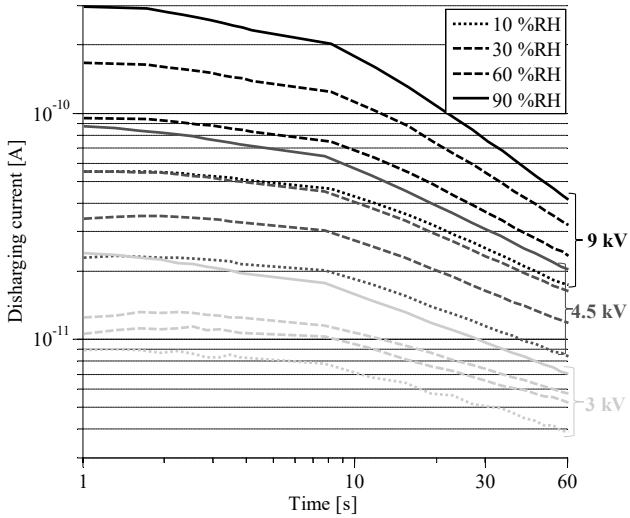

Figure 50. Short-time discharging currents at 80 °C. The currents are inverted.

4.4.2.4 **Effect of increased temperature**

As the temperature increased from 40 °C to 60 °C, and further from 60 °C to 80 °C, the time dependence of the charging current changed. From 40 to 60 °C, a peak in the current within the measurement period appeared. In the literature, several different explanations have been proposed to explain observed peaks in charging currents, including ionic hopping [56], space-charge limited current with trapping [54], interaction between homocharge and heterocharge [55] and conduction by electrons hopping between Poole-Frenkel trap sites [52].

For the phenomena described by hopping conduction, both ionic and electronic, increasing the applied field would decrease the time needed to reach a peak in charging current [52,56], as the mobility of the charges increases with increasing field. However, as seen in Figure 47, the measurements at 60 °C did not follow this behaviour, as the time to the peak in the current increased with increasing voltage.

For space-charge limited current, the peak corresponds to an injected charge front crossing from one electrode to the other [54]. In this case, the time from applied voltage to the current peak is the time it takes for the front to move between the electrodes. Using the crossing times at 60 °C, being between 20 and 40 seconds, this leads to a mobility of $0.5–1.0 \cdot 10^{-12}$ m^2 V^{-1} s^{-1}, which is in the upper range of mobilities reported elsewhere [115,125,126]. As for hopping conduction, increasing the voltage should in this case increase the mobility of the charge carriers, decreasing the crossing time and thereby the time needed before a current peak appears; however, at 60 °C the opposite occurs.

The presence of heterocharge near an electrode may in some circumstances lead to changes in the current similar to the observed results. According to [55], injected electrons assumed to accumulate at the cathode will result in reduction of the local electric field. A reduced electric field will lower the injection rate, lowering the conducted current. Positive charge generated elsewhere in the sample accumulating at the cathode will have the opposite effect. This means that a current peak would not only be dependent on charge crossing the sample from one electrode to the other, but also be a result of the balance between injected homocharge and accumulated heterocharge, due to changes in the local electric field. This has been introduced previously when discussing the space charge measurements in Section 4.3.6. Injection affected by same-polarity charge reducing the applied electric field at an electrode would be able to affect the current almost immediately after voltage application. In order for heterocharge to have an effect, it would have to accumulate quite rapidly, as the charging current already increases after 1 second, the earliest measurement time after electrification in the experiments. If the accumulating charge is injected, this would require the mobility to be higher than $2 \cdot 10^{-11}$ m^2 V^{-1} s^{-1}, an order of magnitude larger than what has been observed in the literature [115,125,126].

At 80 °C, the charging current showed no indication of an initial power law response and there were no peaks within the measured time frame; the currents followed a roughly exponential decay trend, which at higher voltages appeared to start levelling out. The departure from exponential decay became more pronounced with increasing voltage, and the currents started to increase at the end of the charging period at the highest voltages. This is consistent with increased temperature decreasing the time constants of the underlying mechanisms, i.e. polarisation, conduction of injected charge and accumulation of hetero- and homocharge. The polarisation currents may not have been present due to the measurements starting after the polarisation currents have died out. The increase in current found at 40 and 60 °C, probably due to the filling of shallow traps over time, was also not present at 80 °C. The initial decrease of current over time at the lower voltages may be a result of homocharge build-up decreasing injection due to lowering of the local electric field, which could also be seen at the end of the charging measurements at 60 °C. The subsequent increase in current at 80 °C may be a result of accumulation of heterocharge increasing the electric field again, as injected charge having crossed the bulk of the sample accumulates at the electrode of the opposite polarity. Using the increase in current as a base for the crossing time means the charge should arrive fairly soon after measurement start, i.e. after 1–2 minutes. This yields a mobility in the order of 10^{-13} $m^2 V^{-1} s^{-1}$, which is within the range of observed charge mobilities in the literature [115,125,126].

Regarding discharge current, while at 40 °C it appeared to follow a standard power law depolarisation process, at 60 and 80 °C it appears that this process is no longer as dominant. The slower decay of the discharge currents may be an indication of trapped charge being released over time, which by detrapping over time continues to contribute to the current. This would mean that space charge would be expected to have an increased impact at higher temperatures, which should be reflected in the space charge measurements. Comparing this to the space charge measurements directly is not possible, as the space charge measurements have no data at times less than 5 minutes. But when looking at the first minutes of space charge accumulation, it is apparent that space charge accumulation at short times increases with temperature, making it feasible that this effect could also be present in the current measurements.

4.4.2.5 **Effect of increased water content**

At 40 °C, the polarisation and conduction parts of the current responded differently when the amount of absorbed water was increased. The polarisation part was not affected by water absorption, as for the initial four seconds the current was largely identical for all humidities. The conduction part of the current increased with increased water content, showing that the polarisation and conduction parts of the current are a result of different processes. An increase in current could be the result of both increased number of charge carriers and an increase in mobility, although given that the space charge measurements indicate increased mobility as the most likely mechanism it seems more likely that this is also the origin here. The conduction current increased over time, which may be the increasing number of mobile charge carriers due to the filling of traps, as was observed at higher temperatures. The arrival of heterocharge would also lead to an increase in conducted current, but it seems unlikely to be the origin here as the process should be slower at 40 than at 60 and 80 °C. However, it may be that this is what is observed at later times in the current measurements over 14 days (see Section 4.4.3.2), where the current reached a peak after some hours.

At 60 °C, the response to increased water content seemed to be an increase in both charging and discharging currents. The response at 60 °C seemed to confirm that the mechanisms contributing to the polarisation part of the current are unaffected by humidity, while the conduction current increases with increasing water content, as the relative contribution from polarisation to the total current seemed to decrease with increasing humidity. Except for the difference in the balance between the polarisation and conduction part of the currents, the time development of the charging currents was fairly similar at all humidities. The peak in the current appeared to occur earlier at higher humidities. Going back to the mechanisms discussed in Section 4.4.2.4, an earlier peak could be explained due to an increase in mobility, which fits well with the hypothesis that absorbed water increases mobility through acting as shallow traps for injected charge.

At 80 °C, the effect of increased water content appeared to be dependent on the applied electric field. At voltages of 4.5 kV and lower, the time dependence of the charging currents was similar across all humidities, but with higher current values at higher humidities. This is likely due to an increase in conduction current, the same as was observed at 40 and 60 °C, and would then be explained by an increase in mobility. The currents at voltages higher than 4.5 kV, however, exhibited an increase in current with time that was humidity-dependent. This could be assumed to be the same effect as was observed at 40 °C, where the increase in current was found to result in a peak when the measurement was extended. Using the mobility hypothesis, the same explanation as for 60 °C could be used; higher mobility leads to a peak occurring earlier, and the increase in current is the start of the rise towards that peak. However, it is strange that the peak would occur later at 80 °C than at 60 °C, as charge mobility is expected to rise with

temperature. A possible explanation would be that there are two different processes that lead to charge peaks; e.g. the increasing amount of semi-mobile charge carriers in shallow traps and the accumulation of charge impacting the electric field at the electrodes and consequently charge injection. At 60 °C, the peaks are due to the more rapid process and the measurement stops before the slower process peaks occur, while at 80 °C the measurement starts after the more rapid process is done and the peaks are due to the slower process.

Moving on to discharge, at 40 °C the current is dominated by depolarisation, which is unaffected by the water content. For higher temperatures, and starting by comparing the results with the shallow trap hypothesis presented in Section 2.4.1.1, the increase in discharge current with increased water content at 60 and 80 °C would mean that thermal effects alone are enough to excite some charge carriers out of the shallow traps from water molecules. Water traps would in that case not themselves provide localisation points for the carriers at 60 and 80 °C, and the increase in mobility is present even with no applied field. Increased water content means a higher density of shallow traps, reducing the average distance between traps and increasing the effective mobility. At the end of the charging period, a significant part of the transported charge is currently in transit in the bulk of the sample. When the voltage is removed, this charge is not immediately eliminated, but must move some distance in order to either recombine or be extracted from the insulation. The increased mobility from higher concentrations of water leads to a higher current.

For the second hypothesis, dissociated ionic carriers will also be in transit when the electric field is removed. At 40 °C, there are fewer ions, leading to a polarisation-dominated discharge current unaffected by humidity. At 60 and 80 °C, however, there are enough remnant ions to have an effect on the discharge current. The contribution due to increased water content seemed to be almost constant within the period of the measurements, meaning no significant elimination of ionic charge carriers would have occurred during the measurement.

4.4.3 **Long-time charging and discharging currents**

4.4.3.1 **Low water content at 40 °C**

Charging current

Results from the long-time measurement with low water content can be seen in Figure 51. The power law decay in the initial part of the charging current, shown in the insert in Figure 51, was consistent with the short-time measurements in Section 4.4.2. In addition, the first part of the long-time charging current measurement also showed the rising current trend which was present in the short-time measurements between 4 and 50 seconds. This continued to a maximum in the long-time measurement after around 16 hours. If this is assumed to be a charge front having crossed the sample, using one of the mechanisms considered in section 3.1, the 16-hour crossing time would yield an average mobility of around $2.5 \cdot 10^{-16}$ m^2 V^{-1} s^{-1}, which is within the limits of estimated mobilities in the literature [115,125,126]. A similar current-time curve was observed in [58]. The broad shape of the charging current peak may be an indication of a spread in mobilities of the transported carriers, due to varying trap depths. It could however also indicate the arrival of low mobility bulk-generated charge. The principle is the same as for injected charge; charge will continuously be generated and increase the number of charge carriers in the sample, leading to the current increase. It will take a certain time, depending on the mobility of the carrier and the distance it has to travel, for the carrier to travel from where it was generated to the electrode. At the electrode, it will either be extracted or immobilised, which eliminates its contribution to the current. When charges from all generation points have reached the electrode, the current will be constant. For both injected charge and bulk-generated charge it is apparent that a second effect must be present, as the current resided at the maximum for around 11 hours before it decreased for the rest of the measurement. A third possibility is that space charge at the electrodes alter the electric field, affecting injection.

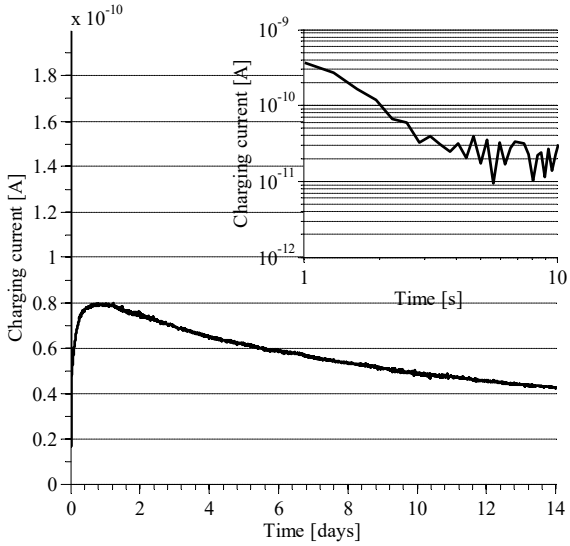

Figure 51. Long-time charging current at 40 °C for a dry sample. The insert is the first 10 seconds, on a log-log scale.

Discharging current

The discharging current also followed the power law for approximately the first 1,000 seconds. The current then gradually fell towards a steady-state value, stabilising after about 1 day. This is likely the same depolarisation phenomenon as was found in Section 4.4.2.1. Although the steady-state value is less than zero, around $-5 \cdot 10^{-14}$ A, the significance of this is limited; it is likely that the picoammeter zero-value had shifted slightly during measurement. As can be seen in the figure, the entire 14 days of discharging was not recorded. After about 9 days of discharging time the guard electrode shifted to make contact with the measuring cable, resulting in very high noise currents that rendered the rest of the discharging current indistinguishable from the noise.

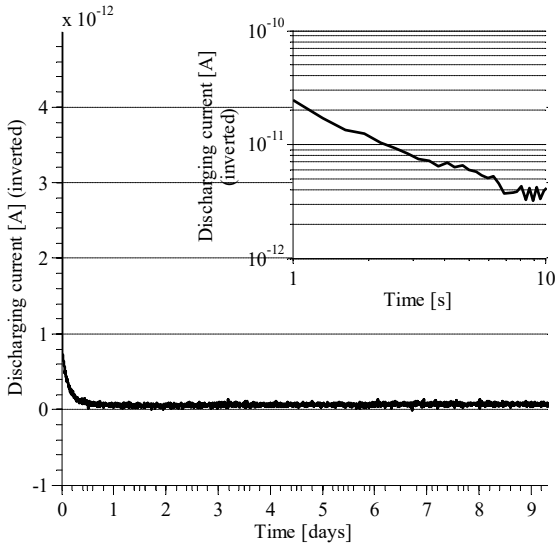

Figure 52. Long-time discharging current at 40 °C for a dry sample. The insert is the first 10 seconds, on a log-log scale. The currents are inverted.

Comparison with space charge measurements

The long-time current measurements can be compared to space charge measurements performed at the same temperature and applied electric field. The comparison starts at 5 minutes after voltage application (or removal), as this is the first measurement point of the space charge measurements. In addition, the comparison will be limited to long-time trends, as the space charge measurements record the average of the signal in 1-minute periods, making this the lowest possible partition of time in the space charge measurements.

Starting at the 5-minute mark, the space charge measurements found homocharge at the anode, which continued to grow until 5 hours into the measurement. Correspondingly, the electric field at the anode, shown in Figure 53, is reduced by the accumulated charge. The reduction in electric field from space charge at 5 minutes is quite small, around 0.4 kV mm^{-1}, while the maximum field reduction, occurring after 4 hours, is 4.4 kV mm^{-1}. Given that the applied field is 30 kV mm^{-1}, this would likely have an impact on the overall current by reducing injection at the anode. There is no corresponding decrease in the measured current around 4–5 hours, however. The subsequent increase in the local electric field due to the reduction in homocharge, seen in Figure 53 to start after 1 day, would result in increased injection, which would be expected to increase the current. In the current measurement, however, the current starts to decrease after around 1 day.

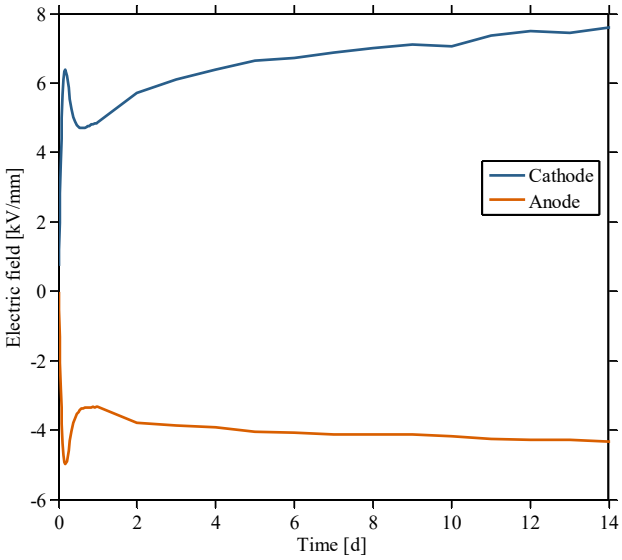

Figure 53. Space charge field at the anode and cathode during space charge measurements at 40 °C and dry conditions. The applied field was +30 kV mm^{-1}, meaning positive values will enhance the local electric field while negative values reduce local field.

The changes in electric field at the cathode are the mirror opposites of the changes in the field at the anode; when the field at the anode decreases, the cathode field increases. Since injection can be assumed to occur at both electrodes, the effects on the current from space charge at one electrode could be masked by the effects of space charge at the other. While this would limit changes in the conducted current, the magnitude of the field enhancement at the cathode is larger than the field reduction at the anode. However, the exact effect of the current would depend on the particular injection processes at the anode and cathode, which may respond differently to changes in the electric field. It is interesting that the electric fields at both electrodes appear to have local minimums occurring during the peak in the charging current at around 14–24 hours, corresponding roughly to the maximum in the measured current. This would in that case mean that the main mechanism affecting the current is injection of charge at the anode, where the field reduction momentarily decreases at 14–24 hours. This is not unreasonable, given that mostly positive space charge is observed in the samples at 40 °C.

At around 24 hours, the measured current started to decrease and continued to fall throughout the measurement period. In the space charge measurements, on the other hand, the field enhancement at the cathode reaches its maximum at the end of the measurement, which means that the injection would be expected to increase for the entire measurement period. The field reduction due to the homocharge at the anode is mostly unchanged from 10 hours onwards and is smaller than the change in field at the cathode. The expected change in current due to space charge, assuming that bipolar injection is taking place,

would therefore be a steady increase due to increasing injection of negative charge from around the same time that the measured charging current starts decreasing. If, on the other hand, bulk generated charge is assumed to be dominant, heterocharge would reduce the electric field in the bulk, leading to possibly reduced charge generation. For both cases, a lower bulk field may lead to lower charge transport velocity.

Electric field enhancement at the electrodes is not the only effect that can connect space charge and current measurements – immobilisation of carriers due to trapping will also affect both. When trapped, a charge carrier will be immobilised for some time, leading to a lower likelihood of other carriers being captured as fewer traps are available. This is similar to the trap-filling phenomenon in space-charge limited current described in Section 2.2.2.4. For trapping to reduce the current, a higher amount of charge will have to be trapped than detrapped. With a finite number of traps in the sample, the number of unoccupied traps would therefore necessarily go down with time. As the trapping rate is dependent on the amount of unoccupied traps, the trapping rate would therefore be expected to go down with time, given that more and more charge is trapped. If the heterocharge is assumed to be mainly responsible for the changes in current, it is therefore odd that the increased injection, in the previous paragraphs suggested to cause the early current increase, is dominant before the 16-hour mark, when the increase in electric field due to the heterocharge is small and the amount of available traps is high. Similarly, the decrease in current due to trapping would have to be dominant after the 16-hour mark, when the amount of available traps is lower and the increase in injection due to the increasing cathode electric field from accumulated heterocharge is high.

The discharge current mainly followed a standard power law discharge pattern, typically characteristic of depolarisation processes, as also found in the short-time current measurements. Discharge of the accumulated space charge seemed to indicate that both the homocharge and heterocharge was the same species.

4.4.3.2 **High water content at 40 °C**

Charging current

At 85% RH, the charging current, shown in Figure 54, exhibited similar time-dependent characteristics as the dry sample. Initially, it displayed a power function decay profile, followed by an increase towards a maximum. The initial power law part was larger for the wet sample than for the dry sample. This is different from the short-time measurements, where the initial power law decay of the charging current was independent of water content. The maximum was reached 7 hours after voltage application, 9 hours earlier than for the dry sample. The peak was also slightly narrower for the high humidity sample. Using the same principle of transit time as for the dry sample, this would correspond to a mobility of around $4.5 \cdot 10^{-16}$ $m^2 V^{-1} s^{-1}$, 1.8 times the mobility of the dry sample. After the maximum, the current then decreased and appeared to be moving towards a stable value when the measurement ended. No steady-state was reached during measurement, however. The charging current was higher at 85% RH than for dry conditions, but the ratio between them varied. For the first 3 hours the wet sample current was 3 to 4 times higher. The difference in current between the wet and dry samples then fell slowly during the rest of the measurement, ending up with the wet sample current being about 1.75 times higher than the dry sample current. This corresponds well with the differences in mobility calculated from the current maxima, which would be proportional to the conductivity and would produce a similar increase in the steady-state current if it was the only factor affecting the current.

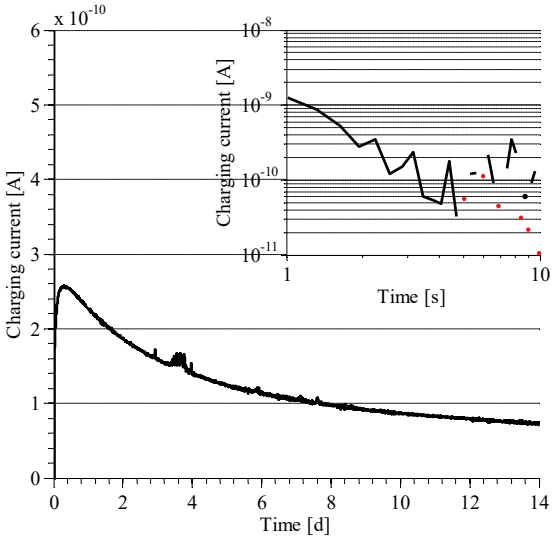

Figure 54. Long-time charging current at 40 °C for a sample at 85% RH. The insert is the first 10 seconds, on a log-log scale. The red dots are inverted negative current values.

As mentioned in Section 4.4.2, there are several hypotheses in the literature predicting a peak in the current through a sample [32,52,54-56]. In [32], a bipolar charge transport model was used to show similar patterns in the time-dependent conducted current as was observed in Figure 51 and Figure 54, although the results in the paper were calculated at higher applied electric fields. The model, which includes trapping and recombination of electrons and holes, shows that two carriers with different mobility will yield peaks in the conducted current at two different times. The peaks correspond to the time it takes for the mobile charge fronts, injected at their respective electrode, to cross to the opposite electrode. Although there is no evidence of a second current peak in either Figure 51 or Figure 54, a general observance can be made: in the model in [32], the higher mobility charge carriers (in that case, holes) arrived earlier at their extracting electrode than the lower mobility carriers, which for current measurements would mean that the current peak corresponding to the holes would occur at an earlier time. Assuming that similar mechanisms are dominant in the measurements in Figure 51 and Figure 54, the earlier occurrence of the current peak in the Figure 54 may indicate that the charge carriers in the wet sample has a higher mobility than the charge carriers in the dry sample. A similar observation was also made in [55].

Discharging current

The discharge current had, for the first 10 seconds, the same polarity as the charging current. This behaviour appeared to be of short duration, as after about 100 seconds the current behaved similarly to what was found in the dry sample. It is believed that the initial high positive discharging current is connected to issues with the guard at high voltage and high humidity. Similar behaviour was observed during initial testing when building the setup, in which case the behaviour was altered when the guard placement was changed. Apart from this, the discharging current at 85% RH behaved similarly to that of the dry sample.

The noise levels for the high humidity case were much higher both for the charging and discharging currents, and single-point current spikes occurred more often and at higher values in the charging current.

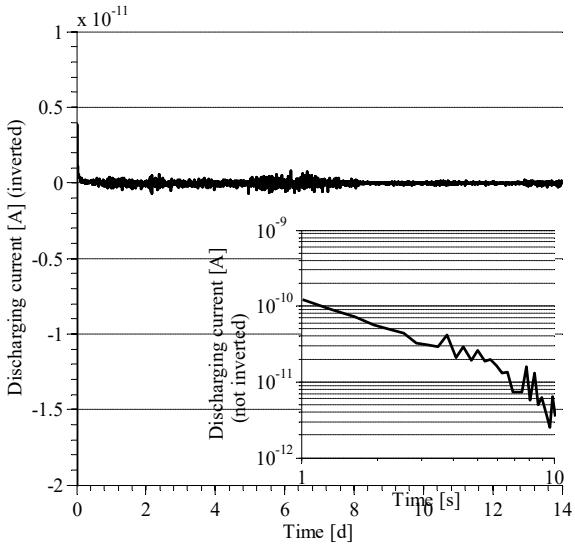

Figure 55. Long-time discharging currents at 40 °C for a sample at 85% RH. The insert is the first 10 seconds. The currents are inverted in the main plot but are not inverted in the insert plot.

Comparison with space charge measurements

As for the dry sample, the long-time current measurement was performed at the same temperature and relative humidity, and at similar applied electric field as one of the space charge measurements, in order to compare the two sets of measurement results.

Looking at the space charge distribution for 40 °C 85% RH in Figure 32 and the field distribution in Figure 56, the field reduction due to positive homocharge would decrease injection at the anode, while the field enhancement at the cathode due to heterocharge would lead injection to increase there. The similarity of the charge distributions of the dry and the wet samples leads to the expectation of a similar conducted current. The amount of charge and the resulting effect on the local electric field is lower for the wet sample, however, meaning that the expected effect on the conducted current would be expected to be lower. The measured currents show that this is not the case, however, as charging current for the wet sample appears to have a more pronounced peak than the dry sample current, as can be seen when comparing Figure 51 with Figure 54.

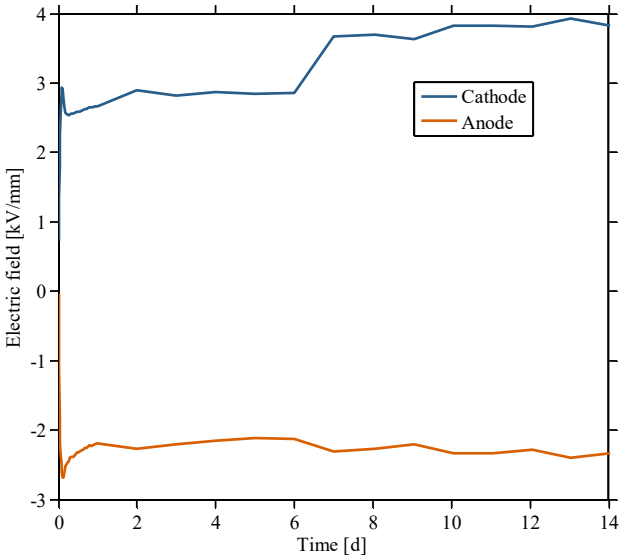

Figure 56. Space charge field at the anode and cathode during space charge measurements at 40 °C and wet conditions. The applied field was +30 kV mm^{-1}, meaning positive values will enhance the local electric field while negative values reduce local field. Note that the sharp increase in electric field at the cathode from 6 days to 7 days is due to a scaling problem between the oscilloscope and the recording computer.

While there were some changes in the electric field from space charge occurring around the same time as conducted current peaked, the impact of these changes is probably limited. First, the increase in electric field at the cathode was accompanied by a simultaneous reduction of electric field at the anode. The potential increased injection at the cathode would therefore be expected to be accompanied by a reduction of injection at the anode. The net effect this would have on the current would of course depend on the respective injection processes and the properties of the injected charge carriers. However, as for the dry sample, mostly positive charge is observed, meaning that assuming anode injection to be dominant would not be unreasonable. Secondly, the changes in charge accumulation occurred at around 3 hours, while the peak in conducted current was at 7 hours after electrification. In order to definitely conclude that the space charge field at the electrodes was the single dominating factor in charge transport in the sample, a clearer effect would be preferred. Similarly as in the dry sample, the homocharge at the anode reached a stable value after around 10 hours. A difference compared to the dry sample, in which the cathode heterocharge continued to increase for the duration of the measurement, was that the heterocharge near the cathode also reached a stable value, in this case after around two days. Any effect on the conducted current from the space charge field would therefore be expected to be more or less constant after this time. Although the relaxation time of the sample seems to be very long, it does not apparently correlate to

the time constants of the space charge accumulation. In fact, the conducted current does not show any clear connection to the dynamics of the space charge distribution.

4.4.4 **Summary**

Results from time-dependent current measurements showed that injected charge is likely the dominant process for dry samples, through a combination of polarisation currents, charge transport across the samples and space charge-affected field-dependent injection. Remnant space charge was found to likely affect the discharge currents at higher temperatures. Absorbed water was found to likely increase the mobility of the injected charge, but not to affect polarisation processes. Comparisons between current and space charge measurements in dry samples at 40 °C indicated that positive charge injection, limited by the accumulation of space charge at the anode, could be the dominant mechanism affecting the current. For wet samples, however, lower amounts of accumulated space charge would imply that smaller changes in the current should occur, while the current measurements showed larger changes occurring. Looking at the current measurements separately, increased mobility of injected charge seems to be a feasible explanation.

4.5 Results and discussion summary

The results from all three sets of measurements – conductivity mechanisms, space charge accumulation, time dependent current – have shown that a single set of measurement data is not sufficient to conclude what mechanism or mechanisms are responsible for charge transport and accumulation.

Conduction mechanisms for dry samples were narrowed down to either Poole-Frenkel conduction or space charge limited current. When adding the space charge measurement results, the most likely mechanism was found to be injected charge carriers, due to accumulation of homocharge. Heterocharge in dry samples was found to most likely be injected charge transported through the sample to reach the opposite electrode, due to the large amounts of ionic dissociation or extremely high mobility required to achieve the amounts of heterocharge found in the samples if bulk-generated charge was assumed. Some indications of bipolar injection were found, although charge at higher temperatures was mainly positive. For time dependent current measurement, it was found that increased mobility of injected charge with increased temperature and space charge affecting the electric field at the electrodes could explain the results. However, comparison between time dependent currents and space charge accumulation over a 14-day period did not reveal any clear correlation between the measurement results.

Absorption of water led to additional mechanisms fitting as well or better than Poole-Frenkel or space charge limited current. Including a second ionic dissociation mechanism in the analysis enabled the entire conductivity data set to be described, but required parameters outside values permissible by physics. Space charge measurements showed that both increased mobility of injected carriers and bulk-generated charge could explain the changes in heterocharge when water was absorbed. However, while the lower amount of accumulated charge at 40 and 60 °C could be explained by increased mobility of charge, it could not be easily explained by ionic dissociation. The accumulation of space charge at 80 °C diverged from the lower temperatures, resulting in increasing amounts of positive charge in the bulk for the duration of the charging measurement. Calculations of apparent mobility showed a reduced carrier mobility in the wet sample at 80 °C compared to dry conditions, which would explain increased accumulation of charge, but the origin of the divergence is still unclear. Analysis of the time dependent current measurements showed that water increasing mobility of injected charge could explain the results satisfactorily, although the results did not clearly disprove ionic dissociation.

In summary, bipolar injection with temperature and absorbed water affecting injected charge mobility seems like the more plausible hypothesis.

5 Conclusion

Measurements of field- and temperature-dependent conductivity, space charge accumulation and discharge, and time-dependent current measurements have been presented and discussed in this thesis. Based on this work, the following conclusions can be drawn:

- Charge accumulation and transport in XLPE insulation with semiconducting electrodes was found to be mainly due to injected charge.

- Higher temperatures led to increased injection of charge and increased charge mobility, leading to the conducted current being exponentially dependent on the temperature. Higher mobility also resulted in injected charge moving across the insulation to accumulate as heterocharge. The effects were more prominent for positive charge than negative charge. Positive charge was the main type of accumulated charge at higher temperatures.

- Several commonly used conduction mechanisms (Schottky, Poole-Frenkel, hopping and space-charge limited current) were found to describe the conduction current for dry samples, and also for samples with the same water content across temperatures. No systematic variation of fitting parameters with water content was found for any conduction mechanism.
    - Space-charge limited current provided good fits for low levels of water content.
    - Poole-Frenkel conduction provided good fits for low and intermediate levels of water content.
    - Schottky injection provided good fits for high levels of water content.
    - None of the conduction mechanisms included in the study were found to be able to predict the changes in conducted current when water was absorbed, and a combination of two conduction mechanisms (Poole-Frenkel and ionic dissociation) provided a good empirical fit.

- Water absorption increased the mobility of injected charge, increasing the current up to 3.5 times the current in dry samples.
    - Water absorption did not alter the electric field dependence of the conduction currents.
    - The increase in current from water absorption from close-to-dry to close-to-saturation is comparable to the increase in current when temperature is increased by 5–10 °C or the electric field by 3–5 kV mm^{-1}.

- The increased charge mobility from water absorption affected space charge accumulation through:
    - Faster charge accumulation dynamics, leading to changes in charge distributions occurring at earlier times for the wet compared to the dry samples;
    - Time to apparent equilibrium shorter at 40 and 60 °C;
    - Less charge accumulating, lowering of the amounts of net charge at 20–60 °C in wet samples compared to dry samples.

  Water absorption at 80 °C led to the space charge accumulation diverging from the lower temperatures, resulting in higher amounts of accumulated charge. The accumulation of charge did not stabilise during the duration of the measurements. The origins of this apparent shift in the mechanism are uncertain.

The changes in conducted current and accumulated space charge due to absorbed water do not appear to be critical to XLPE insulation systems in HVDC conditions for temperatures between 20 and 60 °C. The effect of absorbed water at temperatures closer to maximum allowable XLPE service temperatures should be investigated further, however, as space charge measurements at 80 °C revealed a potentially detrimental change in the mechanism.

Future work

Some suggestions for future work that arise from the results are listed below:

- Although small at temperatures of 20–60 °C, the changes in conductivity with absorbed water should be included when calculating the electric field distribution e.g. for joints in a wet-designed cable. This could be done by e.g. modifying the conductivity of XLPE in the model to include the dual mechanism described by Equation (4.12). The modified conductivity of the cable insulation could then be combined with calculations of water absorption and temperature gradient, to achieve a predictive model of the electric field distribution based on the accessory design.

- A bipolar injection model with trapping and recombination, where the mobility of charge carriers is modified based on the water content, should be developed and verified against the measurement results at 20–60 °C. Such a model could then be used to predict space charge effects in cables and cable accessories.

- While the measurements in this thesis have been performed on an XLPE insulation material with semiconducting electrodes, the composition of such materials will vary between different grades of material and between different material manufacturers. It is also suspected that HVDC grade materials will differ somewhat in composition from the AC superclean grade used here. The current- and space charge measurement techniques used in the thesis should therefore be used to characterise several different combinations of XLPE insulation and semiconductor materials for HVDC cable use.

- The effect of absorbed water on space charge accumulation at 80 °C did not follow the expected trend from the lower temperatures. It is also uncertain whether this charge accumulation would stabilise over time or continue to grow. It is also unclear whether a continued increase in temperature up to the traditional limit of 90 °C would exacerbate the issue. Further investigation of space charge accumulation in XLPE insulation exposed to high temperature and containing high amounts of absorbed water is therefore warranted.

Appendix A
Material datasheets

Polyethylene

Supercure™ LS4201S

Crosslinkable Insulation Compound

Description

Supercure LS4201S is a crosslinkable natural polyethylene compound, specially designed for insulation applications.

Applications

Supercure LS4201S is intended for insulation of XLPE High Voltage cables with rated voltages up to 220 kV.

Specifications

Supercure LS4201S meets the applicable requirements as below when processed using sound extrusion practice and testing procedure:

AEIC CS7-93 (3rd edition)
HD 632 S1
IEC 60840
ANSI/ICEA 108-720-2004

Special features

Supercure LS4201S is a ready-to-use natural compound. It is specially developed for high productivity through a reduced degassing burden and with an enhanced extrusion performance. The cleanliness property and excellent distribution of additives in Supercure LS4201S would result in superclean insulation.

Physical Properties

Property		Typical Value Data should not be used for specification work	Test Method
Density (Base Resin)		922 kg/m3	ISO 1872-2/ISO 1183
Melt Flow Rate (190 °C/2,16 kg) [1]		2 g/10min	ISO 1133
Tensile Strain at Break (250 mm/min) [2]		> 450 %	ISO 527
Tensile Strength (250 mm/min) [2]		> 17 MPa	ISO 527
Retention of Tensile Properties After Ageing (500 h, 135 °C) [2]		< 20 %	IEC 60811-1-2
Hot Set Test (200 °C, 0,20 MPa)	Elongation under load	75 %	IEC 60811-2-1
	Permanent deformation	5 %	
Göttfert Elastograph		0,56 - 0,67 Nm	
Methanol Wash		< 800 ppm	
Moisture		< 200 ppm	Karl Fischer-titration

[1] Base Resin
[2] Measured on crosslinked specimens

Borealis AG | Wagramerstrasse 17-19 | 1220 Vienna | Austria
Telephone +43 1 224 00 0 | Fax +43 1 22 400 333
FN 269858a | CCC Commercial Court of Vienna | Website www.borealisgroup.com

BOREALIS

Polyethylene
Supercure LS4201S

Electrical Properties

Property	Typical Value Data should not be used for specification work	Test Method
Dielectric constant (50 Hz)	2,3	IEC 60250
DC Volume Resistivity	> 10 POhm.cm	IEC 60093
Dielectric Strength (50 Hz)	> 30 kV/mm	IEC 60243
Dissipation Factor (50 Hz)	0,0005	IEC 60250

Processing Techniques

To produce a good and reliable cable, it is essential to ensure careful and very clean handling of the insulation material. Hence all material handling should preferably be conducted in closed systems and in clean room conditions. Practical advice is given in a separate brochure. Please contact your Borealis representative for more details.

Extrusion

Melt temperature	130 - 140 °C

Packaging

Package: Smallbins
Octabins

Storage

Supercure LS4201S has a shelf life of 12 months from production date if stored in unopened original packages, under dry and clean conditions at temperatures between 15 - 25 °C. The material could be stored (originally closed and in dry environment) at an ambient temperature up to 40°C for a certain period of time (6 months) without negative influence on the material quality. Before use, material shall be conditioned indoors (production room) at the ambient temperature.

More information on storage is found in our "Safety data sheet" / "Product safety information sheet" for this product.

Safety

The product is not classified as dangerous and is intended for industrial use only. Check and follow local codes and regulations!

Please see our "Safety data sheet" / "Product safety information sheet" for details on various aspects of safety of the product. For more information, contact your Borealis representative.

Borealis AG | Wagramerstrasse 17-19 | 1220 Vienna | Austria
Telephone +43 1 224 00 0 | Fax +43 1 22 400 333
FN 269858a | CCC Commercial Court of Vienna | Website www.borealisgroup.com

Polyethylene

Supercure LS4201S

Disclaimer

The product(s) mentioned herein are not intended to be used for medical, pharmaceutical or healthcare applications and we do not support their use for such applications.

To the best of our knowledge, the information contained herein is accurate and reliable as of the date of publication, however we do not assume any liability whatsoever for the accuracy and completeness of such information.

Borealis makes no warranties which extend beyond the description contained herein. Nothing herein shall constitute any warranty of merchantability or fitness for a particular purpose.

It is the customer's responsibility to inspect and test our products in order to satisfy itself as to the suitability of the products for the customer's particular purpose. The customer is responsible for the appropriate, safe and legal use, processing and handling of our products.

No liability can be accepted in respect of the use of Borealis' products in conjunction with other materials. The information contained herein relates exclusively to our products when not used in conjunction with any third party materials.

Borealis AG | Wagramerstrasse 17-19 | 1220 Vienna | Austria
Telephone +43 1 224 00 0 | Fax +43 1 22 400 333
FN 269858a | CCC Commercial Court of Vienna | Website www.borealisgroup.com

Polyethylene
LE0592
Crosslinkable Semiconductive Compound

Description
LE0592 is a crosslinkable black polyethylene compound, specially designed for bonded semiconductive screen applications.

Applications
LE0592 is intended for semiconductive applications in XLPE medium and high voltage cables. It can be used as inner and outer semicon for bonded constructions and as inner semicon for strippable constructions.

Specifications
LE0592 meets the applicable requirements as below when processed using sound extrusion practice and testing procedure:

AEIC CS7
AEIC CS8
BS 6622
DIN VDE 0276-620
DIN VDE 0276-263
HD 620 S1
HD 632 S1
IEC 60502
IEC 60840
ISO 1872-E/BA, KHXY, 23-G200, C40
NF C33-223
NF C33-226
UTE C 33-223
UTE C 33-223
ICEA S 93 639

Special features
LE0592 is a ready-to-use semiconductive compound. The excellent distribution of carbon black and additives in LE0592 would result in an outstanding smooth semiconductive screen.

Physical Properties

Property		Typical Value Data should not be used for specification work	Test Method
Density		1135 kg/m3	ISO 1872-2/ISO 1183
Tensile Strain at Break (25 mm/min)		200 %	ISO 527
Tensile Strength (25 mm/min)		22 MPa	ISO 527
Change of Tensile Properties After Ageing (240 h, 135 °C)		< 20 %	IEC 60811-1-2
Hot Set Test (200 °C, 0,20 MPa)	Elongation under load	25 %	IEC 60811-2-1
	Permanent deformation	0 %	
Göttfert Elastograph		1,14 - 1,38 Nm	
Moisture (1.000 ppm)		300 ppm	Karl Fischer-titration

Borealis AG | Wagramerstrasse 17-19 | 1220 Vienna | Austria
Telephone +43 1 224 00 0 | Fax +43 1 22 400 333
FN 269858a | CCC Commercial Court of Vienna | Website www.borealisgroup.com

Polyethylene
LE0592

Electrical Properties

Property	Typical Value Data should not be used for specification work	Test Method
DC Volume Resistivity (23 °C)	< 100 Ohm.cm	ISO 3915
DC Volume Resistivity (90 °C)	< 1000 Ohm.cm	ISO 3915

Processing Techniques

LE0592 provides excellent surface finish and outstanding output rates, when processing conditions are optimized for the actual processing equipment and cable dimensions. Optimal conditions may vary according to the equipment used.

Extrusion

Typical processing temperature ranges for LE0592 are shown below:

Hopper drying (4 h)	60 °C	Under agitation with dehumidified air.
Melt temperature	120 - 140 °C	

Packaging

Package: Smallbins
Octabins

Storage

LE0592 has a shelf life of 18 months from production date if stored in unopened original packages, under dry and clean conditions at temperatures between 10 - 30 °C (50 - 85 °F).

More information on storage is found in our "Safety data sheet" / "Product safety information sheet" for this product.

Safety

The product is not classified as dangerous and is intended for industrial use only. Check and follow local codes and regulations!

Please see our "Safety data sheet" / "Product safety information sheet" for details on various aspects of safety of the product. For more information, contact your Borealis representative.

Borealis AG | Wagramerstrasse 17-19 | 1220 Vienna | Austria
Telephone +43 1 224 00 0 | Fax +43 1 22 400 333
FN 269858a | CCC Commercial Court of Vienna | Website www.borealisgroup.com

Polyethylene
LE0592

Disclaimer

The product(s) mentioned herein are not intended to be used for medical, pharmaceutical or healthcare applications and we do not support their use for such applications.

To the best of our knowledge, the information contained herein is accurate and reliable as of the date of publication, however we do not assume any liability whatsoever for the accuracy and completeness of such information.

Borealis makes no warranties which extend beyond the description contained herein. Nothing herein shall constitute any warranty of merchantability or fitness for a particular purpose.

It is the customer's responsibility to inspect and test our products in order to satisfy itself as to the suitability of the products for the customer's particular purpose. The customer is responsible for the appropriate, safe and legal use, processing and handling of our products.

No liability can be accepted in respect of the use of Borealis' products in conjunction with other materials. The information contained herein relates exclusively to our products when not used in conjunction with any third party materials.

Borealis AG | Wagramerstrasse 17-19 | 1220 Vienna | Austria
Telephone +43 1 224 00 0 | Fax +43 1 22 400 333
FN 269858a | CCC Commercial Court of Vienna | Website www.borealisgroup.com

Appendix B
Water absorption and diffusion

B.1 Theory

Water absorption in non-porous polymers is determined by the available polymer-free volume, the interaction between the polymer matrix and water and the interaction between the water molecules themselves. In systems with low concentration of water and low interaction, Fick's and Henry's laws are the governing equations for water absorption and transport. Fick's law states that the water flux is proportional to the concentration gradient:

$$J = -D\nabla C \tag{B.1}$$

where J is the water flux, C is the concentration and D is a proportionality coefficient called the diffusion coefficient [133]. Obtaining time-dependent water concentration can be done by rewriting Equation (B.1) using the continuity equation, yielding

$$\frac{\partial C}{\partial t} = -\nabla \cdot \left(-D\nabla C\right) \tag{B.2}$$

where t is time [133]. Henry's law states that the concentration of water immediately inside a polymer surface is proportional to the partial pressure of water immediately outside the surface:

$$C = Sp \tag{B.3}$$

where p is the partial pressure of water and S is a proportionality coefficient called the solubility coefficient [134].

Solving Equation (B.2) with respect to concentration and combining the solution with Henry's law, the relation between the mass uptake of water for a thin film sample and the solubility and diffusion coefficients can be expressed as

$$C(t) = C_S\left(1 - \exp\left(-7.3\left(\frac{Dt}{l^2}\right)^{3/4}\right)\right) \tag{B.4}$$

where l is the sample thickness and C_S is the equilibrium concentration of water [135].

For a polymer film with different partial pressures of water on each side, combining Fick's and Henry's laws can be used to find the water flux:

$$J = P\frac{p_2 - p_1}{l} \tag{B.5}$$

where $p_2 > p_1$ are the partial pressures of water on the two sides, l is the thickness of the polymer film and $P = DS$ is the permeability coefficient.

Absorption, diffusion and permeation are thermally activated processes, and the solubility, diffusion and permeability coefficients can be assumed to follow Arrhenius relations [136].

Filler materials added to polymers, such as carbon black to increase conductivity, can affect the diffusion and absorption properties of the material. While inorganic fillers will absorb only small amounts of water themselves, due to their close-packed molecular structure when compared to e.g. polymers, surface adsorption and alteration of the interface region between polymer and filler can lead to increased solubility and decreased diffusivity. Carbon black and the interface region will likely be more hydrophilic compared to the polymer matrix, acting as secondary adsorption sites. Water molecules adsorbing to these sites will be partially immobilised, similar to permanent microvoids (or 'holes') in glassy polymers, which can be described by a Langmuir absorption isotherm [137]:

$$C = \frac{C'bp}{1 + bp} \tag{B.6}$$

where C' is a proportionality coefficient called the hole saturation constant and b is the hole affinity constant, which is related to the rate of sorption and desorption in the holes (or more generally adsorption sites). Modelling water absorption over time in a film of such a material starts with the equation set

$$\begin{aligned} D\frac{\partial^2 n}{\partial^2 z} &= \frac{\partial n}{\partial t} + \frac{\partial N}{\partial t} \\ \frac{\partial N}{\partial t} &= \gamma n - \beta N \end{aligned} \tag{B.7}$$

where n is the number of mobile water molecules, N is the number of immobilised water molecules, z is the position in the film thickness direction, γn is the rate of immobilisation (γ is the probability of immobilisation per unit time) and βN is the rate of remobilisation (β is the probability of remobilisation per unit time) [138]. Solving Equation (B.7), as

shown in [138], and substituting the time dependence for Fickian diffusion from Equation (B.4) [135], yields

$$C = C_S\left(\frac{\beta}{\gamma+\beta}\exp(-\gamma t)\left(-\exp\left(-7.3\left(D\frac{t}{l^2}\right)^{0.75}\right)\right)+\exp(-\beta t)\left(\frac{\beta}{\beta+\gamma}-1\right)+1\right) \quad \text{(B.8)}$$

B.2 Experimental procedures

Determining the diffusion and solubility coefficients can in principle be done in two ways: through water absorption measurements and through water permeability measurements. Water absorption measurements comprise placing a sample in a humid environment, either by exposing it to air with controlled relative humidity or by placing it in water and measuring the water content at regular intervals. Water permeability measurements comprises exposing one side of a sample to a humid environment, either air of controlled relative humidity or water, and measuring the amount of water that goes through the sample over time.

B.2.1 Gravimetric water absorption measurements

The water uptake in the semiconducting copolymer was characterised with gravimetric water absorption measurements. Sample discs, 0.5 mm thick, were made by initial roll milling and subsequent hot pressing. Individual samples, 15 mm in diameter, were prepared by using a hole punch. The samples were dried in vacuum at 80 °C for at least 3 days and left to cool to room temperature in vacuum. At the start of the water absorption measurements, each sample was individually removed from the vacuum chamber and the dry weight recorded. The sample was then placed in a heated water bath. At regular intervals, each sample was removed from the water bath, dried off with blotting paper, and the weight recorded. Equation (B.4) was used to find the Fickian approximate solubility and diffusion coefficients, while Equation (B.8) was used to find parameters for diffusion with immobilisation sites. Measurements were performed at 40, 60 and 80 °C.

B.2.2 Freeze-drying saturation concentration measurements

Based on earlier results in [139], the diffusion coefficient of the XLPE insulation material was expected to be too high to obtain good results with the weighing method. The more sensitive freeze-drying method was therefore chosen to measure the saturation concentration, which can be used to obtain the solubility through Henry's law (Equation (B.3)). The method, described in more detail in [139], utilises a sealed vacuum oven to extract the water from the sample and collects it with a cold trap. Samples were prepared from extruded film, press-cast and hole punched into rectangular samples weighing approximately 250–350 mg. After being dried, the samples were placed in a water bath for between 5 and 17 days, before being removed, dried with blotting paper and placed in the freeze-drying apparatus for measurement. The dry weight was measured after freeze-drying, and the water concentration calculated. Measurements were performed at 40, 60 and 80 °C.

B.2.3 Freeze-drying water permeability measurements

In order to obtain the water permeability of XLPE, a permeability test cell for the freeze-drying apparatus was used. The test cell, described in more detail in [140], places a sample film between a heated water bath on one side and the vacuum system with the cold trap on the other side. Water will permeate through the film, and the flux can be found by measuring the amount of water collected in the cold trap at regular intervals. At steady-state, the permeability coefficient can then be found using Equation (B.5). Measurements were performed at 40, 60, 80 and 90 °C.

B.3 Results

B.3.1 Water absorption in semiconducting copolymer

The measured increase in water concentration over time in the semiconducting copolymer is shown in Figure 57. As can be seen, Fickian diffusion fits well for the initial water absorption behaviour of the samples, while at higher concentration levels the fit becomes poorer. The coefficients obtained from the Fickian fits are listed in Table 17. It is likely that the polymer matrix dominates initially, and that when it is saturated with water the effects of the filler material becomes more prominent. The fit of Equation (B.8) is seen to better model the absorption behaviour of the semiconducting copolymer, matching the initial rapid sorption behaviour, the second rapid sorption and the end equilibrium reasonably well. The coefficients used for the dashed lines in Figure 57 are listed in Table 18.

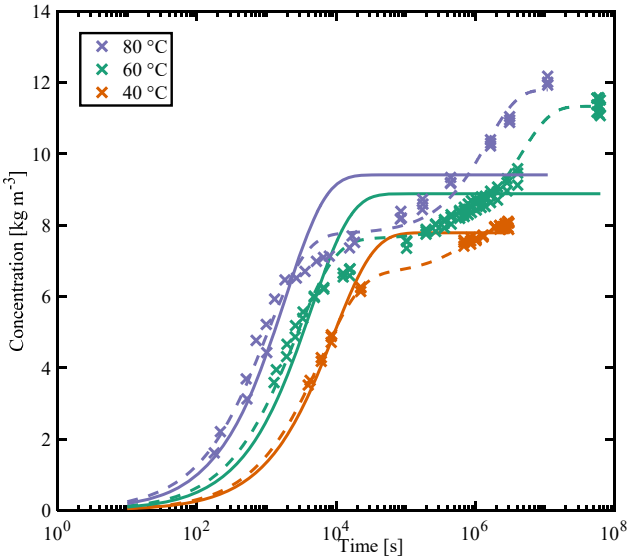

Figure 57. Water concentration in semiconducting copolymer. Solid lines are Fickian fits, dashed lines are fits for water absorption with immobilisation sites.

Table 17: Arrhenius coefficients for solubility and diffusion in the semiconducting polymer, based on Fick's and Henry's laws

S_0	E_S	D_0	E_D
[kg m^{-3} Pa^{-1}]	[J mol^{-1}]	[m^2 s^{-1}]	[J mol^{-1}]
$4.18 \cdot 10^{10}$	-38404	$4.32 \cdot 10^{-6}$	36540

Table 18: Non-Fickian water absorption and diffusion coefficients for semiconducting polymer

T	C_S	D	γ	β
[°C]	[kg m^{-3}]	[m^2 s^{-1}]	[s^{-1}]	[s^{-1}]
40	8.05	$2.98 \cdot 10^{-12}$	$2.68 \cdot 10^{-7}$	$1.23 \cdot 10^{-6}$
60	11.36	$6.82 \cdot 10^{-12}$	$1.10 \cdot 10^{-7}$	$2.24 \cdot 10^{-7}$
80	11.80	$1.77 \cdot 10^{-11}$	$3.52 \cdot 10^{-7}$	$6.73 \cdot 10^{-7}$

B.3.2 Water saturation concentration of XLPE insulation

The measured water saturation concentration is shown in Figure 58. Using water saturation vapour pressures, the solubility was found through Henry's law (Equation (B.3)), and fitted to an Arrhenius relation, yielding the parameters listed in Table 19. The Arrhenius parameters found for the modern type of XLPE in these measurements very closely matches the values found in earlier reported measurements on an older, steam-cured XLPE in [139].

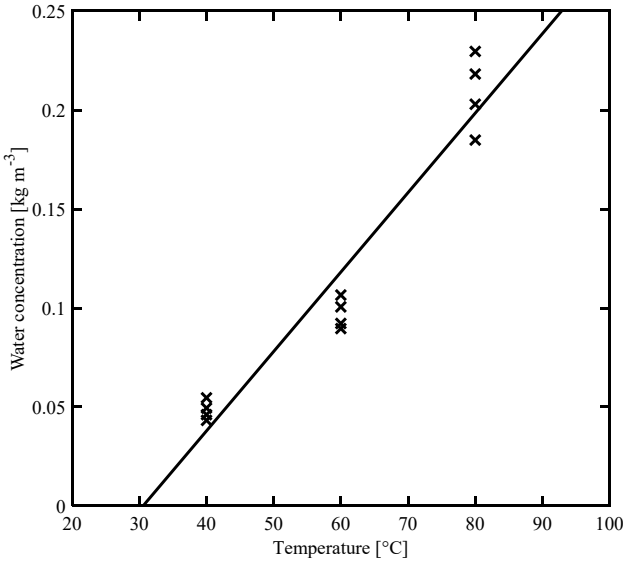

Figure 58. Water saturation concentration for XLPE. The line indicates the Arrhenius fit.

Table 19: Arrhenius coefficients for solubility in XLPE

S_0	E_S
[kg m^{-3} Pa^{-1}]	[J mol^{-1}]
$1.84 \cdot 10^7$	-9239

B.3.3 Water permeability measurements in XLPE

The measured flux of water through XLPE and the corresponding calculated water permeability can be found in Table 20, with the resulting Arrhenius coefficients listed in Table 21. Comparing the measured values with older data from [139] shows that water permeability in modern XLPE is less temperature-dependent than the previous results show. This may be related to different curing methods: the XLPE in [139] was steam-cured, while the modern XLPE is peroxide-cured.

Table 20: Measured water flux and water permeability in XLPE

T	J	P
[°C]	[kg m^{-2} s^{-1}]	[kg m^{2} s^{-1} m^{-3} Pa^{-1}]
40	$2.35 \cdot 10^{-8}$	$1.48 \cdot 10^{-15}$
60	$1.14 \cdot 10^{-7}$	$2.67 \cdot 10^{-15}$
80	$4.61 \cdot 10^{-7}$	$4.57 \cdot 10^{-15}$
90	$9.77 \cdot 10^{-7}$	$6.55 \cdot 10^{-15}$

Table 21: Arrhenius coefficients for water permeability in XLPE

P_0	E_P
[kg m^{-3} Pa^{-1}]	[J mol^{-1}]
$5.72 \cdot 10^{-11}$	27554

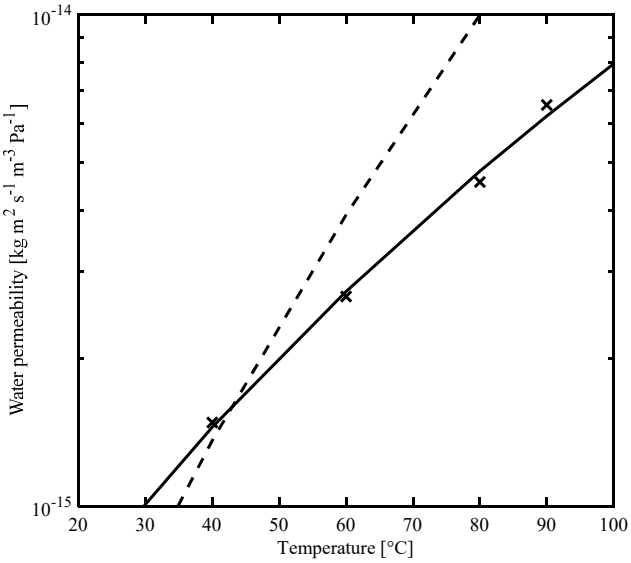

Figure 59. Water permeability in XLPE. Measured values and Arrhenius fit (solid line) for modern XLPE, and Arrhenius parameter fit for steam-cured XLPE from [139] (dashed line).

B.4 Numerical calculation of conditioning times

In order to ensure that the insulation in the test objects is in equilibrium with regards to water absorption and thereby representative for the intended temperature and humidity conditions, the test objects need to be pre-conditioned for a minimum amount of time. To estimate the minimum conditioning time for the Rogowski and plate test objects at the relevant temperatures and relative humidities, Finite Element Method (FEM) calculations were performed. The FEM modelling used discretisations of Fick's and Henry's laws, and was based on work previously published in [141]. Note that this modelling tool has not been developed for non-Fickian diffusion of the type described in Equation (B.8), and the approximate Fickian coefficients in Table 17 were used to represent the semiconducting copolymer. For the XLPE, the Arrhenius parameters for the solubility coefficient in Table 19 were used, while the diffusion coefficient Arrhenius parameters were calculated using $D = P/S$ from the values in Table 21 and Table 19.

B.4.1 Geometric models

Test object model geometries can be found in Figure 60 and Figure 61. The Rogowski test object was modelled by simplifying the Rogowski profile to a Bezier polygon, and otherwise keeping the measurements exact. Each test object in Table 2 was modelled with its individual insulation thickness. Examples of calculated water concentrations for conditioning of a Rogowski test object at 40 °C are shown in Figure 62. As can be seen, at 40 °C, the insulation reaches equilibrium after about 1 day of conditioning. The corresponding values are 0.5 days and 3 hours for 60 °C and 80 °C, respectively. Variations in insulation thickness did not change the time to equilibrium significantly. To allow for some margin of error due to the non-Fickian nature of the semiconducting polymer, the conditioning times in the experiments were doubled, compared to the estimated times from the calculations. The water concentrations for conditioning a plate test object to 85% RH at different temperatures is shown in Figure 63. As for the Rogowski test object, the conditioning times for the plate objects were selected to be longer than the times to equilibrium found in the calculations, to allow for some margin of error. For the pre-conditioning times used in the measurements, see Table 3 and Table 4.

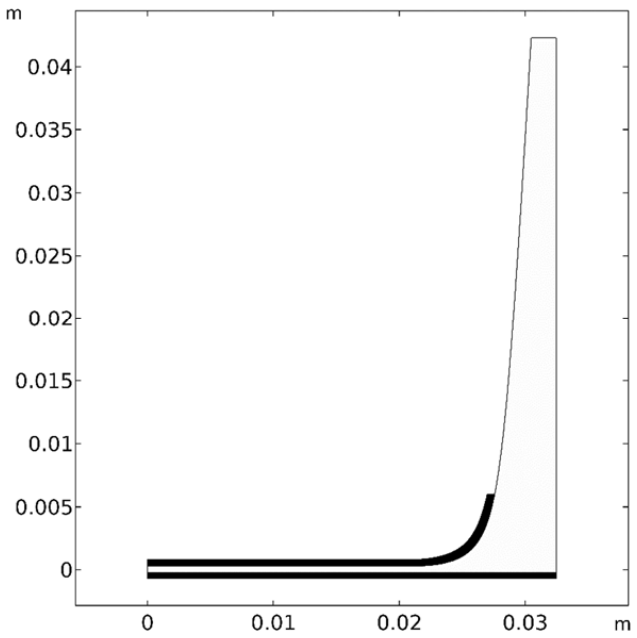

Figure 60. FEM model geometry, Rogowski test object. Black areas are semiconducting copolymer, white enclosed areas are insulation.

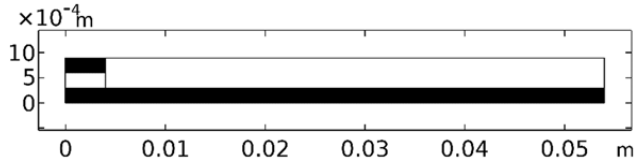

Figure 61. FEM model geometry, plate test object. Black areas are semiconducting copolymer, white enclosed areas are insulation.

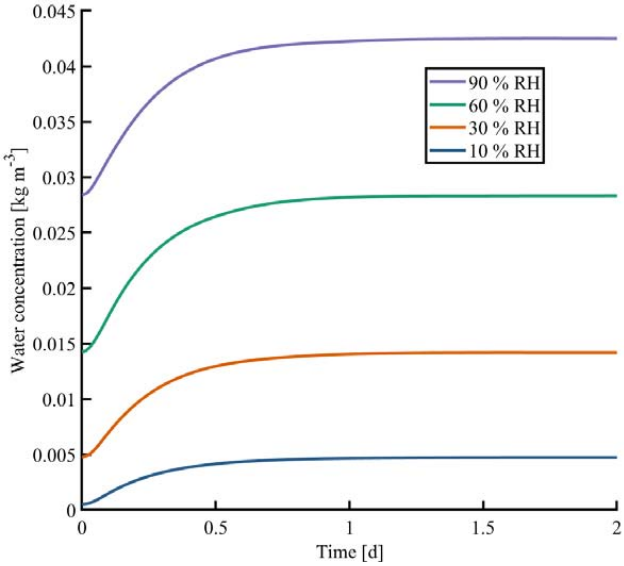

Figure 62. Water concentration in the FEM model of Rogowski test object during conditioning at 40 °C.

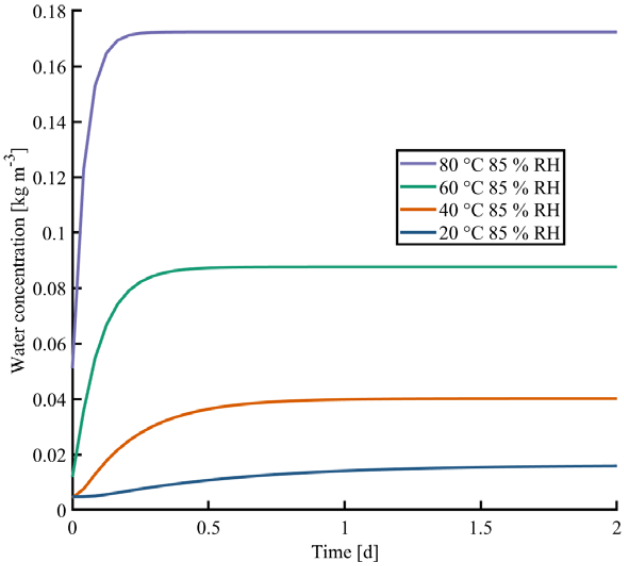

Figure 63. Water concentration in the FEM model of plate test object during conditioning to 85% RH at 20, 40, 60 and 80 °C.

References

[1] G. Mazzanti and M. Marzinotto, *Extruded Cables for High-Voltage Direct-Current Transmission: Advances in Research and Development*. John Wiley & Sons, 2013.

[2] A. Alassi, S. Bañales, O. Ellabban, G. Adam, and C. MacIver, "HVDC Transmission: Technology Review, Market Trends and Future Outlook," *Renewable and Sustainable Energy Reviews,* vol. 112, pp. 530-554, 2019/09/01/ 2019

[3] CIGRE TB 219 (2003), 'Recommendations for testing DC extruded cable systems for power transmission at a rate voltage of up to 250 kV'.

[4] G. Chen, M. Hao, Z. Xu, A. Vaughan, J. Cao, and H. Wang, "Review of high voltage direct current cables," *CSEE Journal of Power and Energy Systems,* vol. 1, no. 2, pp. 9-21, 2015

[5] G. C. Montanari, "Bringing an insulation to failure: the role of space charge," *IEEE Trns. Dielectr. Electr. Insul.,* vol. 18, no. 2, pp. 339-364, 2011

[6] G. Mazzanti and G. Montanari, "Electrical aging and life models: the role of space charge," *IEEE Trns. Dielectr. Electr. Insul.,* vol. 12, no. 5, pp. 876-890, 2005

[7] *ECHA Candidate List for Substances of Very High Concern, ED/61/2018,* European Chemicals Agency (ECHA), 2018.

[8] J. Sletbak and A. Botne, "A study of inception and growth of water trees and electrochemical trees in polyethylene and cross linked polyethylene insulations," *Electrical Insulation, IEEE Transactions on,* no. 6, pp. 383-389, 1977

[9] F. Aida, S. A. Wang, M. Fujita, G. Tanimoto, and Y. Fujiwara, "Study of the mechanism of space charge formation in polyethylene," (in English), *Journal of Electrostatics,* Proceedings Paper vol. 42, no. 1-2, pp. 3-15, Oct 1997

[10] G. C. Montanari and F. Palmieri, "The effect of humidity on space charge accumulation in XLPE," presented at the 2003 Annual report conference on electrical insulation and dielectric phenomena, 2003.

[11] A. Aragoneses *et al.*, "Effect of humidity in charge formation and transport in LDPE," *Journal of Electrostatics,* vol. 71, no. 4, pp. 611-617, 8// 2013

[12] L. Hui, L. S. Schadler, and J. Nelson, "The influence of moisture on the electrical properties of crosslinked polyethylene/silica nanocomposites," *Dielectrics and Electrical Insulation, IEEE Transactions on,* vol. 20, no. 2, pp. 641-653, 2013

[13] J. Yang, X. Wang, H. Zhao, W. Zhang, and M. Xu, "Influence of moisture absorption on the DC conduction and space charge property of MgO/LDPE nanocomposite," *Dielectrics and Electrical Insulation, IEEE Transactions on,* vol. 21, no. 4, pp. 1957-1964, 2014

[14] G. Chen, T. Y. G. Tay, A. E. Davies, Y. Tanaka, and T. Takada, "Electrodes and charge injection in low-density polyethylene - Using the pulsed electroacoustic technique," (in English), *IEEE Trns. Dielectr. Electr. Insul.,* Article vol. 8, no. 6, pp. 867-873, Dec 2001

[15] L. A. Dissado, "Understanding electrical trees in solids: from experiment to theory," *IEEE Trns. Dielectr. Electr. Insul.,* vol. 9, no. 4, pp. 483-497, 2002

[16] L. A. Dissado and J. C. Fothergill, *Electrical degradation and breakdown in polymers*, 1 ed. (IEEE materials and devices, no. 9). London: Peter Peregrinus Ltd., 1992, p. 601.
[17] T. Miyamoto and K. Shibayama, "Free-volume model for ionic conductivity in polymers," *Journal of Applied Physics,* vol. 44, no. 12, pp. 5372-5376, 1973
[18] K. C. Kao, *Dielectric phenomena in solids*. Academic press, 2004.
[19] G. Blaise, "Charge localization and transport in disordered dielectric materials," *Journal of Electrostatics,* vol. 50, no. 2, pp. 69-89, 2001
[20] G. Teyssedre and C. Laurent, "Charge transport modeling in insulating polymers: from molecular to macroscopic scale," *Dielectrics and Electrical Insulation, IEEE Transactions on,* vol. 12, no. 5, pp. 857-875, 2005
[21] T. Mizutani, "Behavior of charge carriers in organic insulating materials," in *2006 Annual Report Conference on Electrical Insulation and Dielectric Phenomena*. New York: Ieee, 2006, pp. 1-10.
[22] G. Strobl, *Condensed matter physics*. Springer, 2004.
[23] K. Less and E. Wilson, "Intrinsic photoconduction and photoemission in polyethylene," *Journal of Physics C: Solid State Physics,* vol. 6, no. 21, p. 3110, 1973
[24] M. Meunier, N. Quirke, and A. Aslanides, "Molecular modeling of electron traps in polymer insulators: Chemical defects and impurities," (in English), *Journal of Chemical Physics,* Article vol. 115, no. 6, pp. 2876-2881, Aug 2001
[25] M. Meunier and N. Quirke, "Molecular modeling of electron trapping in polymer insulators," *The Journal of Chemical Physics,* vol. 113, no. 1, pp. 369-376, 2000
[26] D. Cubero, G. Marcelli, and N. Quirke, "Electronic states of excess electrons in polyethylene," in *Electrical Insulation and Dielectric Phenomena, 2002 Annual Report Conference on*, 2002: IEEE, pp. 430-433
[27] S. Serra, E. Tosatti, S. Iarlori, S. Scandolo, and G. Santoro, "Interchain electron states in polyethylene," *Physical Review B,* vol. 62, no. 7, p. 4389, 2000
[28] N. F. Mott and R. W. Gurney, "Electronic processes in ionic crystals," 1948
[29] B. G. Bagley, "The field dependent mobility of localized electronic carriers," *Solid State Communications,* vol. 8, no. 5, pp. 345-348, 1970
[30] S. Boggs, D. H. Damon, J. Hjerrild, J. T. Holboll, and M. Henriksen, "Effect of insulation properties on the field grading of solid dielectric DC cable," *Power Delivery, IEEE Transactions on,* vol. 16, no. 4, pp. 456-461, 2001
[31] S. Le Roy, P. Segur, G. Teyssedre, and C. Laurent, "Description of bipolar charge transport in polyethylene using a fluid model with a constant mobility: model prediction," *Journal of physics D: Applied physics,* vol. 37, no. 2, p. 298, 2004
[32] I. Boukhris, E. Belgaroui, and A. Kallel, "Physical and Numerical Modelling for Bipolar Charge Transport in Disorder Polyethylene Under High DC Voltage," *International Journal on Electrical Engineering and Informatics,* vol. 2, no. 4, p. 313, 2010
[33] H. Boukhari and F. Rogti, "Simulation of Space Charge Dynamic in Polyethylene Under DC Continuous Electrical Stress," *Journal of Electronic Materials,* journal article vol. 45, no. 10, pp. 5334-5340, 2016
[34] B. Sanden, E. Ildstad, and R. Hegerberg, "Space charge accumulation and conduction current in XLPE insulation," in *Dielectric Materials, Measurements and Applications, Seventh International Conference on (Conf. Publ. No. 430)*, 23-26 Sep 1996 1996, pp. 368-373

[35] A. Hascoat *et al.*, "Study and analysis of conduction mechanisms and space charge accumulation phenomena under high applied DC electric field in XLPE for HVDC cable application," in *Electrical Insulation and Dielectric Phenomena (CEIDP), 2014 IEEE Conference on*, 2014: IEEE, pp. 530-533

[36] J. Castellon *et al.*, "Electrical properties analysis of micro and nano composite epoxy resin materials," *IEEE Trans. Dielectr. Electr. Insul,* vol. 18, no. 3, pp. 651-658, 2011

[37] J. J. O'Dwyer, *The theory of electrical conduction and breakdown in solid dielectrics*. Oxford: Clarendon Press, 1973, pp. IX, 317 s.

[38] T. Mizutani and M. Ieda, "Carrier transport in high-density polyethylene," *Journal of Physics D: Applied Physics,* vol. 12, no. 2, pp. 291-296, 1979/02/01 1979

[39] Ø. L. Hestad, F. Mauseth, and R. H. Kyte, "Electrical conductivity of medium voltage XLPE insulated cables," presented at the IEEE International Symposium on Electrical Insulation, 2012, ISEI 2012 San Juan, Puerto Rico, 2012.

[40] K. S. Suh, C. R. Lee, J. S. Noh, J. Tanaka, and D. H. Damon, "Electrical conduction in polyethylene with semiconductive electrodes," *Dielectrics and Electrical Insulation, IEEE Transactions on,* vol. 1, no. 2, pp. 224-230, 1994

[41] B. Sanden, "XLPE cable insulation subjected to HVDC stress: space charge, conduction and breakdown strength," Dr.Ing., Department of Electrical Power Engineering, NTNU, Trondheim, 1996.

[42] R. Gilbert, J.-P. Crine, B. Noirhomme, and S. Pélissou, "Measurement of organic and inorganic ions in cable insulation and shields," in *Electrical Insulation and Dielectric Phenomena, 1989. Annual Report., Conference on*, 1989: IEEE, pp. 235-240

[43] Y. Li and T. Takada, "Experimental observation of charge transport and injection in XLPE at polarity reversal," *Journal of Physics D: Applied Physics,* vol. 25, no. 4, p. 704, 1992

[44] Y. Maeno, N. Hirai, Y. Ohki, T. Tanaka, M. Okashita, and T. Maeno, "Effects of crosslinking byproducts on space charge formation in crosslinked polyethylene," (in English), *IEEE Trns. Dielectr. Electr. Insul.,* Proceedings Paper vol. 12, no. 1, pp. 90-97, Feb 2005

[45] K. S. Suh, S. J. Hwang, J. S. Noh, and T. Takada, "Effects of Constituents of XLPE on the Formation of Space Charge," *IEEE Trns. Dielectr. Electr. Insul.,* vol. 1, no. 6, pp. 1077-1083, 1994

[46] T. Takeda, N. Hozumi, H. Suzuki, and T. Okamoto, "Factor of space charge generation in XLPE under DC electric field of 20 kV/mm," in *Properties and Applications of Dielectric Materials, 1997., Proceedings of the 5th International Conference on*, 25-30 May 1997 1997, vol. 1, pp. 137-141 vol.1

[47] R. Barker Jr and A. Sharbaugh, "Ionic conduction in polymer films and related systems," in *Journal of Polymer Science Part C: Polymer Symposia*, 1965, vol. 10, no. 1: Wiley Online Library, pp. 139-152

[48] T. Blythe and D. Bloor, *Electrical Properties of Polymers*, 2 ed. Cambridge: Cambridge University Press, 2005, p. 491.

[49] A. Denat, "Conduction and breakdown initiation in dielectric liquids," in *Dielectric Liquids (ICDL), 2011 IEEE International Conference on*, 2011: IEEE, pp. 1-11

[50] L. Onsager, "Deviations from Ohm's law in weak electrolytes," *The Journal of Chemical Physics,* vol. 2, no. 9, pp. 599-615, 1934

[51] A. K. Jonscher, *Dielectric response in solids*. London: Chelsea Dielectrics Press Ltd., 1983.
[52] P. Röhl, "Dispersive hopping transport in polyethylene," in *Proceedings of First International Conference on Conduction and Breakdown in Solid Dielectrics*, 1983: IEEE, pp. 50-55
[53] S. Le Roy, G. Teyssedre, C. Laurent, G. Montanari, and F. Palmieri, "Description of charge transport in polyethylene using a fluid model with a constant mobility: fitting model and experiments," *Journal of Physics D: Applied Physics,* vol. 39, no. 7, p. 1427, 2006
[54] A. Many and G. Rakavy, "Theory of transient space-charge-limited currents in solids in the presence of trapping," *Physical Review,* vol. 126, no. 6, p. 1980, 1962
[55] A. K. Jonscher, "The physical origin of negative capacitance," *Journal of the Chemical Society, Faraday Transactions 2: Molecular and Chemical Physics,* vol. 82, no. 1, pp. 75-81, 1986
[56] M. Iwamoto, "Transient current across insulating films with long-range movements of charge carriers," *Journal of applied physics,* vol. 79, no. 10, pp. 7936-7943, 1996
[57] E. Belgaroui, I. Boukhris, A. Kallel, G. Teyssedre, and C. Laurent, "A new numerical model applied to bipolar charge transport, trapping and recombination under low and high dc voltages," *Journal of Physics D: Applied Physics,* vol. 40, no. 21, 2007
[58] T. Christen and E. Logakis, "The generic conduction model for solid polymer HVDC insulation material," in *2013 IEEE International Conference on Solid Dielectrics (ICSD)*, June 30 2013-July 4 2013 2013, pp. 1044-1047
[59] D. K. Das-Gupta, "Conduction mechanisms and high-field effects in synthetic insulating polymers," *Dielectrics and Electrical Insulation, IEEE Transactions on,* vol. 4, no. 2, pp. 149-156, 1997
[60] I. W. McAllister, G. C. Crichton, and A. Pedersen, "Charge accumulation in DC cables: a macroscopic approach," in *Electrical Insulation, 1994., Conference Record of the 1994 IEEE International Symposium on*, 5-8 Jun 1994 1994, pp. 212-216
[61] R. Coelho, "Charges in non homogeneous dielectrics," in *Electrical Insulation and Dielectric Phenomena, 1997. IEEE 1997 Annual Report., Conference on*, 19-22, Oct 1997 1997, vol. 1, pp. 1-10 vol.1
[62] D. A. Seanor, *Electrical properties of polymers*. Elsevier, 2013.
[63] J. Bezille, H. Janah, J. Chan, and M. Hartley, "Influence of diffusion on some electrical properties of synthetic cables," in *Electrical Insulation and Dielectric Phenomena, 1992. Annual Report. Conference on*, 1992: IEEE, pp. 567-572
[64] J. Hjerrild, J. Holboll, M. Henriksen, and S. Boggs, "Effect of semicon-dielectric interface on conductivity and electric field distribution," *Dielectrics and Electrical Insulation, IEEE Transactions on,* vol. 9, no. 4, pp. 596-603, 2002
[65] G. Montanari, G. Mazzanti, F. Palmieri, and B. Bertuzzi, "Mobility evaluation from space charge measurements performed by the pulsed electroacoustic technique," in *Properties and Applications of Dielectric Materials, 2000. Proceedings of the 6th International Conference on*, 2000, vol. 1: IEEE, pp. 38-41

[66] G. Chen and T. Van Nguyen, "Apparent mobility and its relationship with ageing in polymeric insulation materials," in *Condition Monitoring and Diagnosis, 2008. CMD 2008. International Conference on*, 2008: IEEE, pp. 633-637

[67] M. Unge, C. Tornkvist, and T. Christen, "Space charges and deep traps in polyethylene—Ab initio simulations of chemical impurities and defects," in *Solid Dielectrics (ICSD), 2013 IEEE International Conference on*, 2013: IEEE, pp. 935-939

[68] J. Jonsson and C. Törnkvist, "Space charge injection as a function of carbonyl group content in polyolefins," in *Nordic Insul. Symp. NORD-IS*, 1996, pp. 217-224

[69] A. Campus, P. Carstensen, A. A. Farkas, and M. Meunier, "Chemical defects and electron trapping relevant to cable dielectrics," in *2002 Annual Report Conference on Electrical Insulation and Dielectric Phenomena*, 2002, pp. 155-158.

[70] M. Mashikian, J. H. Groeger, S. Dale, and E. Ildstad, "Role of semiconducting compounds in the premature aging of XLPE cable insulation," in *Conference Record of the 1988 IEEE International Symposium on Electrical Insulation*, 1988: IEEE, pp. 314-320

[71] A. Garton, J. Groeger, and J. Henry, "Ionic impurities in crosslinked polyethylene cable insulation," *IEEE transactions on electrical insulation,* vol. 25, no. 2, pp. 427-434, 1990

[72] A. Belhadfa, A. Houdayer, P. Hinrichsen, G. Kajrys, J.-P. Crine, and B. Noirhomme, "Migration of impurities from semicon shield through PE insulation under various experimental conditions," in *IEEE International Symposium on Electrical Insulation*, 1990: IEEE, pp. 321-325

[73] K.-M. Jager and L. Lindbom, "The continuing evolution of semiconductor materials for power cable applications," *IEEE Electr. Insul. Mag.,* vol. 21, no. 1, pp. 20-34, 2005

[74] J. Parpal, J. Crine, A. Houdayer, and P. Hinrichsen, "Study of semiconductor impurity diffusion in XLPE cable insulation under electrical aging," in *1993 Third International Conference on Power Cables and Accessories 10kV - 500kV*, 23-25 Nov. 1993 1993, pp. 153-156

[75] Y. Sekii, T. Ohbayashi, T. Uchimura, K. Mochizuki, and T. Maeno, "The effects of material properties and inclusions on the space charge profiles of LDPE and XLPE," in *2002 Annual Report Conference on Electrical Insulation and Dielectric Phenomena*. New York: Ieee, 2002, pp. 635-639.

[76] N. Hirai, Y. Maeno, T. Tanaka, Y. Ohki, M. Okashita, and T. Maeno, "Effect of crosslinking on space charge formation in crosslinked polyethylene," in *Properties and Applications of Dielectric Materials, 2003. Proceedings of the 7th International Conference on*, 2003, vol. 3: IEEE, pp. 917-920

[77] Y. Sekii and T. Maeno, "Generation and Dissipation of Negative Heterocharges in XLPE and EPR," *Dielectrics and Electrical Insulation, IEEE Transactions on,* vol. 16, no. 3, pp. 668-675, 2009

[78] M. Novak and G. M. Loudon, "The pKa of acetophenone in aqueous solution," *The Journal of Organic Chemistry,* vol. 42, no. 14, pp. 2494-2498, 1977/07/01 1977

[79] S. T. Hagen, "AC Breakdown Strength of XLPE Cable insulation," Dr. Ing., Department of Electrical Power Engineering, Norwegian Institute of Technology (NTH), Trondheim, 1993.

[80] Y. Sekii, A. Taya, and T. Maeno, "Effect of Antioxidants on Space Charge Generation in Cross-linked Polyethylene and EPR," in *2006 IEEE Conference on Electrical Insulation and Dielectric Phenomena*, 15-18 Oct. 2006 2006, pp. 133-137

[81] R. E. Barker Jr, "Mobility and Conductivity of Ions in and into Polymeric Solids," *Pure and Applied Chemistry,* vol. 46, no. 2, pp. 157-170, 1976

[82] D. M. Taylor and T. J. Lewis, "Electrical conduction in polyethylene terephthalate and polyethylene films," *Journal of Physics D: Applied Physics,* vol. 4, no. 9, p. 1346, 1971

[83] C. Alquie, G. Dreyfus, and J. Lewiner, "Stress-wave probing of electric field distributions in dielectrics," *Physical Review Letters,* vol. 47, no. 20, p. 1483, 1981

[84] R. Gerhard-Multhaupt, G. M. Sessler, J. E. West, K. Holdik, M. Haardt, and W. Eisenmenger, "Investigation of piezoelectricity distributions in poly (vinylidene fluoride) by means of quartz-or laser-generated pressure pulses," *Journal of applied physics,* vol. 55, no. 7, pp. 2769-2775, 1984

[85] W. Eisenmenger and M. Haardt, "Observation of charge compensated polarization zones in polyvinylindenfluoride (PVDF) films by piezoelectric acoustic step-wave response," *Solid State Communications,* vol. 41, no. 12, pp. 917-920, 1982

[86] R. Collins, "Analysis of spatial distribution of charges and dipoles in electrets by a transient heating technique," *Journal of Applied Physics,* vol. 47, no. 11, pp. 4804-4808, 1976

[87] A. Cherifi, M. A. Dakka, and A. Toureille, "The validation of the thermal step method," *Electrical Insulation, IEEE Transactions on,* vol. 27, no. 6, pp. 1152-1158, 1992

[88] S. B. Lang and D. Das-Gupta, "Laser-intensity-modulation method: A technique for determination of spatial distributions of polarization and space charge in polymer electrets," *Journal of applied physics,* vol. 59, no. 6, pp. 2151-2160, 1986

[89] T. Takada and T. Sakai, "Measurement of Electric Fields at a Dielectric/Electrode Interface Using an Acoustic Transducer Technique," *Electrical Insulation, IEEE Transactions on,* vol. EI-18, no. 6, pp. 619-628, 1983

[90] N. H. Ahmed and N. N. Srinivas, "Review of space charge measurements in dielectrics," *Dielectrics and Electrical Insulation, IEEE Transactions on,* vol. 4, no. 5, pp. 644-656, 1997

[91] J. Lewiner, S. Hole, and T. Ditchi, "Pressure wave propagation methods: a rich history and a bright future," *Dielectrics and Electrical Insulation, IEEE Transactions on,* vol. 12, no. 1, pp. 114-126, 2005

[92] S. Holé, "Recent developments in the pressure wave propagation method," *Electrical Insulation Magazine, IEEE,* vol. 25, no. 3, pp. 7-20, 2009

[93] R. Singh, "A review of developments in thermal techniques for charge profile measurements in polymer electrets," *Journal of Electrostatics,* vol. 72, no. 4, pp. 322-329, 8// 2014

[94] T. Maeno, H. Kushibe, T. Takada, and C. Cooke, "Pulsed electroacoustic method for the measurement of volume charges in E-beam irradiated PMMA," *CEIDP Annual Report,* pp. 389-393, 1985

[95] T. Maeno, T. Futami, H. Kushibe, T. Takada, and C. M. Cooke, "Measurement of spatial charge distribution in thick dielectrics using the pulsed electroacoustic

method," *Electrical Insulation, IEEE Transactions on,* vol. 23, no. 3, pp. 433-439, 1988
[96] K. Fukunaga, H. Miyata, M. Sugimori, and T. Takada, "Measurement of charge distribution in the insulation of cables using pulsed electroacoustic method," *Trans. IEE japan,* vol. 110, pp. 647-648, 1990
[97] N. Hozumi, H. Suzuki, T. Okamoto, K. Watanabe, and A. Watanabe, "Direct observation of time-dependent space charge profiles in XLPE cable under high electric fields," *Dielectrics and Electrical Insulation, IEEE Transactions on,* vol. 1, no. 6, pp. 1068-1076, 1994
[98] T. Maeno, "Three-dimensional PEA charge measurement system," *Dielectrics and Electrical Insulation, IEEE Transactions on,* vol. 8, no. 5, pp. 845-848, 2001
[99] T. Maeno and K. Fukunaga, "Open-PEA system for space charge measurement in dielectrics under irradiation," in *Solid Dielectrics, 2004. ICSD 2004. Proceedings of the 2004 IEEE International Conference on*, 5-9 July 2004 2004, vol. 2, pp. 944-946 Vol.2
[100] Y. Echigo, H. Tanaka, Y. Ohki, K. Fukunaga, T. Maeno, and K. Okamoto, "Effects of Humidity and Temperature on Space Charge Distribution Profiles in Printed Circuit Board Insulations," in *Solid Dielectrics, 2007. ICSD '07. IEEE International Conference on*, 8-13 July 2007 2007, pp. 458-461
[101] G. Dagher, S. Holé, and J. Lewiner, "A preliminary study of space charge distribution measurements at nanometer spatial resolution," *Dielectrics and Electrical Insulation, IEEE Transactions on,* vol. 13, no. 5, pp. 1036-1041, 2006
[102] Five Labs Co., "PEANUTS user's manual," 2009.
[103] T. Takada *et al.*, "Space Charge Measurements in Dielectric and Insulating Materials," CIGRE D1.12.01, 2006.
[104] Y. Li and M. K. Daigaku, *Space charge measurement in lossy solid dielectric materials by pulsed electroacoustic method*. Musashi Institute of Technology, 1994.
[105] J. B. Bernstein, "Electrical characterization of polymeric insulation by electrically stimulated acoustic wave measurements," Massachusetts Institute of Technology, 1990.
[106] J. C. Lagarias, J. A. Reeds, M. H. Wright, and P. E. Wright, "Convergence properties of the Nelder--Mead simplex method in low dimensions," *SIAM Journal on optimization,* vol. 9, no. 1, pp. 112-147, 1998
[107] F. Boufayed *et al.*, "Models of bipolar charge transport in polyethylene," 2006
[108] E. H. Doedens, "Topographical impact on space charge injection, accumulation and breakdown in polymeric HVDC cable interfaces," PhD, Department of Electrical Engineering, Chalmers University of Technology, Gotherburg, Sweden, 2020.
[109] K. Adachi, G. Harrison, J. Lamb, A. M. North, and R. A. Pethrick, "High frequency ultrasonic studies of polyethylene," *Polymer,* vol. 22, no. 8, pp. 1032-1039, 1981
[110] L. Lin and A. S. Argon, "Structure and plastic deformation of polyethylene," *Journal of Materials Science,* vol. 29, no. 2, pp. 294-323, 1994/01/01 1994
[111] K. Ikezaki, T. Kaneko, and T. Sakakibara, "Effect of Crystallinity on Electrical Conduction in Polypropylene," *Japanese Journal of Applied Physics,* vol. 20, no. 3, pp. 609-615, 1981/03 1981

[112] J. O'dwyer, "A model for high field conduction in a dielectric," *IEEE transactions on electrical insulation,* no. 2, pp. 121-127, 1986
[113] A. V. Bandura and S. N. Lvov, "The ionization constant of water over wide ranges of temperature and density," *Journal of physical and chemical reference data,* vol. 35, no. 1, pp. 15-30, 2006
[114] K. R. Bambery and R. J. Fleming, "Space charge accumulation in two power cable grades of XLPE," *IEEE Trns. Dielectr. Electr. Insul.,* Proceedings Paper vol. 5, no. 1, pp. 103-109, Feb 1998
[115] G. Mazzanti, G. C. Montanari, F. Palmieri, and J. Alison, "Apparent trap-controlled mobility evaluation in insulating polymers through depolarization characteristics derived by space charge measurements," *Journal of Applied Physics,* vol. 94, no. 9, pp. 5997-6004, 2003
[116] H. J. Wintle, "Decay of Static Electrification by Conduction Processes in Polyethylene," *Journal of Applied Physics,* vol. 41, no. 10, pp. 4004-4007, 1970
[117] G. Chen, H. Banford, R. Fouracre, and D. Tedford, "Electrical conduction in low-density polyethylene," in *Conduction and Breakdown in Solid Dielectrics, 1989., Proceedings of the 3rd International Conference on*, 1989: IEEE, pp. 277-281
[118] P. T. Landsberg, "Einstein and statistical thermodynamics. III. The diffusion-mobility relation in semiconductors," *European Journal of Physics,* vol. 2, no. 4, pp. 213-219, 1981/10/01 1981
[119] L. Lan, J. Wu, Y. Yin, and Q. Zhong, "Investigation on heterocharge accumulation in crosslinked polyethylene: Experiment and simulation," *Japanese Journal of Applied Physics,* vol. 53, no. 7, p. 071702, 2014
[120] T.-c. Zhou, G. Chen, R.-j. Liao, and Z. J. J. o. A. P. Xu, "Charge trapping and detrapping in polymeric materials: Trapping parameters," vol. 110, no. 4, p. 043724, 2011
[121] Y. Chong, G. Chen, and Y. Ho, "Temperature effect on space charge dynamics in XLPE insulation," *Dielectrics and Electrical Insulation, IEEE Transactions on,* vol. 14, no. 1, pp. 65-76, 2007
[122] T. Mizutani, H. Semi, and K. Kaneko, "Space charge behavior in low-density polyethylene," *IEEE Trns. Dielectr. Electr. Insul.,* vol. 7, no. 4, pp. 503-508, 2000
[123] G. Chen and Z. Xu, "Charge trapping and detrapping in polymeric materials," *Journal of Applied Physics,* vol. 106, no. 12, p. 123707, 2009
[124] G. Chen, Y. Tanaka, T. Takada, and L. Zhong, "Effect of polyethylene interface on space charge formation," *IEEE Trns. Dielectr. Electr. Insul.,* vol. Vol.11, no. No.1, pp. 113-121, 2004
[125] M. Perlman, T. Sonnonstine, and J. S. Pierre, "Drift mobility determinations using surface-potential decay in insulators," *Journal of Applied Physics,* vol. 47, no. 11, pp. 5016-5021, 1976
[126] J. Alison and R. Hill, "A model for bipolar charge transport, trapping and recombination in degassed crosslinked polyethene," *Journal of Physics D: Applied Physics,* vol. 27, no. 6, p. 1291, 1994
[127] T. Kanno, T. Uozumi, and Y. Inoue, "Measurement of space charge distribution in XLPE cable insulation at high temperature," in *Conference Record of the 1998 Ieee International Symposium on Electrical Insulation, Vols 1 and 2*, 1998, pp. 85-88.
[128] L. Boudou, V. Griseri, J. Guastavino, and L. A. Dissado, "Effect of temperature on space charge formation in low density polyethylene role of antioxidant," in

Proceedings of the 2004 Ieee International Conference on Solid Dielectrics, Vols 1 and 2, 2004, pp. 252-255.

[129] L. Lan, J. Wu, Y. Yin, X. Li, and Z. Li, "Effect of temperature on space charge trapping and conduction in cross-linked polyethylene," *IEEE Trns. Dielectr. Electr. Insul.,* vol. 21, no. 4, pp. 1784-1791, 2014

[130] Y. Kemari, A. Mekhaldi, G. Teyssèdre, and M. Teguar, "Correlations between structural changes and dielectric behavior of thermally aged XLPE," *IEEE Trns. Dielectr. Electr. Insul.,* vol. 26, no. 6, pp. 1859-1866, 2019

[131] D. D. Gupta and R. Brockley, "A study of'absorption currents' in low-density polyethylene," *Journal of Physics D: Applied Physics,* vol. 11, no. 6, p. 955, 1978

[132] S. Westerlund and L. Ekstam, "Capacitor theory," *Dielectrics and Electrical Insulation, IEEE Transactions on,* vol. 1, no. 5, pp. 826-839, 1994

[133] J. Crank, *The mathematics of diffusion*. Oxford: Clarendon Press, 1975, pp. VIII, 414.

[134] G. S. Park and J. Crank, *Diffusion in polymers*. London: Academic Press, 1968, pp. XII, 452.

[135] C.-H. Shen and G. S. Springer, "Moisture Absorption and Desorption of Composite Materials," *Journal of Composite Materials,* vol. 10, no. 1, pp. 2-20, January 1, 1976 1976

[136] C. Rogers, "Permeation of gases and vapours in polymers," in *Polymer permeability*: Springer, 1985, pp. 11-73.

[137] W. R. Vieth, *Diffusion in and through polymers : principles and applications*. Munich: Hanser, 1991.

[138] H. G. Carter and K. G. Kibler, "Langmuir-type model for anomalous moisture diffusion in composite resins," *Journal of Composite Materials,* vol. 12, no. 2, pp. 118-131, 1978

[139] E. Ildstad, "Water migration and water treeing in cross-linked polyethylene cables," Dr. Ing., Electrical Engineering Department, The Norwegian Institute of Technology (NTH), Trondheim, 1982.

[140] T. A. Ve, "Verifisering av numeriske berekningar av diffusjon av vatn," MSc, Department of Physics, Norwegian University of Science and Techology (NTNU), 2008.

[141] S. M. Hellesø, V. C. Henøen, and S. Hvidsten, "Simulation of Water Diffusion in Polymeric Cables Using Finite Element Methods," in *Conference Record of the 2008 IEEE International Symposium on Electrical Insulation, 2008. ISEI 2008.* , 2008, pp. 595-598

ISBN 978-82-326-5278-5 (printed ver.)
ISBN 978-82-326-6995-0 (electronic ver.)
ISSN 1503-8181 (printed ver.)
ISSN 2703-8084 (online ver.)

NTNU

Norwegian University of
Science and Technology